

Ph.D. thesis

Electrical properties of hydrogen-related defects in
crystalline silicon

Ole Sinkjær Andersen

December, 2002

Contents

| | | |
|----------|---|-----------|
| 1 | Introduction | 1 |
| 1.1 | Motivation | 1 |
| 1.2 | Approach | 2 |
| 1.3 | Organization | 3 |
| 2 | Deep level defects in semiconductors | 5 |
| 2.1 | Crystal structure and band structure | 5 |
| 2.2 | Shallow and deep energy levels | 7 |
| 2.3 | Interactions with the conduction and the valence band | 9 |
| 2.3.1 | The rate equation | 9 |
| 2.3.2 | The capture process | 10 |
| 2.3.3 | The emission process | 11 |
| 2.4 | Piezospectroscopic theory | 13 |
| 2.4.1 | Stress | 13 |
| 2.4.2 | Strain | 14 |
| 2.4.3 | Influence of stress on defect total energy | 16 |
| 2.4.4 | Total energy diagrams | 20 |
| 3 | Experimental techniques | 23 |
| 3.1 | Schottky diode characterization | 23 |
| 3.1.1 | Energy band diagrams | 23 |
| 3.1.2 | The space charge region | 25 |

| | | |
|----------|--|-----------|
| 3.1.3 | Current-voltage characteristics | 26 |
| 3.1.4 | Capacitance-voltage characteristics | 26 |
| 3.2 | Deep-level transient spectroscopy | 28 |
| 3.2.1 | The principle of DLTS | 28 |
| 3.2.2 | Conventional DLTS | 31 |
| 3.2.3 | Laplace transform DLTS | 33 |
| 3.2.4 | DLTS-related techniques | 36 |
| 3.3 | Secondary ion mass spectroscopy | 39 |
| 3.4 | Electron paramagnetic resonance | 40 |
| 3.5 | Infrared absorption spectroscopy | 42 |
| 3.6 | Theoretical modeling of defects | 42 |
| 4 | Hydrogen incorporation by remote plasma treatment | 44 |
| 4.1 | Background | 44 |
| 4.2 | Experimental details | 47 |
| 4.2.1 | Sample preparation | 47 |
| 4.2.2 | SIMS measurements | 48 |
| 4.3 | Results and discussion | 48 |
| 4.3.1 | Room temperature plasma treatments | 48 |
| 4.3.2 | Effect of treatment temperature | 51 |
| 4.3.3 | Interaction of hydrogen with existing deep level defects | 53 |
| 4.3.4 | Formation of deep level defects by plasma treatment | 54 |
| 4.4 | Summary | 60 |
| 5 | The hydrogen-carbon pair in n-type silicon | 61 |
| 5.1 | Background | 62 |
| 5.1.1 | Theoretical work | 62 |
| 5.1.2 | Experimental work | 63 |
| 5.2 | Sample preparation | 64 |
| 5.3 | Experimental results | 65 |

| | | |
|----------|---|------------|
| 5.3.1 | Electronic characterization | 65 |
| 5.3.2 | Uniaxial stress measurements | 68 |
| 5.4 | Discussion | 73 |
| 5.4.1 | Donor/acceptor behavior of (C-H) _{II} | 73 |
| 5.4.2 | Microscopic identity of (C-H) _{II} | 75 |
| 5.4.3 | Analysis of piezospectroscopic parameters | 77 |
| 5.4.4 | Reorientation as a precursor for diffusion | 77 |
| 5.4.5 | Comparison to isolated atomic hydrogen | 79 |
| 5.5 | Summary | 80 |
| 6 | Piezospectroscopic analysis of the VO complex in silicon | 82 |
| 6.1 | Background | 82 |
| 6.2 | Sample preparation | 84 |
| 6.3 | Experimental results | 84 |
| 6.3.1 | Influence of stress on the emission and capture processes | 86 |
| 6.3.2 | Stress-induced alignment | 89 |
| 6.3.3 | Influence of stress on the reorientation barriers | 91 |
| 6.4 | Discussion | 93 |
| 6.4.1 | Piezospectroscopic parameters for the stable VO configuration | 93 |
| 6.4.2 | Stress dependence of the emission and capture processes | 95 |
| 6.4.3 | Charge state dependent reorientation | 96 |
| 6.4.4 | The saddle point configuration | 97 |
| 6.5 | Summary | 100 |
| 7 | Interactions of hydrogen with radiation induced defects | 101 |
| 7.1 | Background | 101 |
| 7.1.1 | Interactions of hydrogen with the vacancy-oxygen complex | 101 |
| 7.1.2 | Interactions of hydrogen with the divacancy | 103 |
| 7.2 | Sample preparation | 104 |
| 7.3 | Overview | 105 |

| | | |
|----------|---|------------|
| 7.4 | Hydrogen passivation of the VO complex | 108 |
| 7.4.1 | Electronic properties | 108 |
| 7.4.2 | Effect of hydrogen on defect concentrations | 110 |
| 7.4.3 | Uniaxial stress study of the VOH acceptor level | 111 |
| 7.4.4 | Uniaxial stress study of the VOH donor level | 114 |
| 7.5 | Hydrogen passivation of the divacancy | 116 |
| 7.5.1 | Electronic properties | 116 |
| 7.5.2 | Effect of hydrogen on defect concentrations | 118 |
| 7.5.3 | Discussion | 120 |
| 7.6 | Summary | 121 |
| 8 | Polarization of a hydrogen related defect in silicon studied by DLTS | 122 |
| 8.1 | Experimental details | 123 |
| 8.1.1 | Sample preparation | 123 |
| 8.1.2 | Electric field distributions | 124 |
| 8.2 | General effect | 124 |
| 8.3 | Preliminary model | 125 |
| 8.4 | Formation conditions | 127 |
| 8.4.1 | Relation to hydrogen | 127 |
| 8.4.2 | Comparison of different materials | 128 |
| 8.5 | Sign of the capacitance changes | 129 |
| 8.6 | Kinetics | 131 |
| 8.6.1 | Electric field dependence of the reverse bias phase process | 131 |
| 8.6.2 | Electric field dependence of the fill pulse phase process | 133 |
| 8.6.3 | Relation between the two processes | 134 |
| 8.6.4 | Temperature dependence | 134 |
| 8.7 | Signal amplitude | 136 |
| 8.7.1 | The reverse bias phase process | 136 |
| 8.7.2 | The fill pulse phase process | 139 |

| | | |
|----------|---|------------|
| 8.8 | Annealing experiments | 140 |
| 8.8.1 | Room temperature annealing | 140 |
| 8.8.2 | Isochronal annealing | 141 |
| 8.9 | Microscopic identity of the polarizing defect | 142 |
| 8.9.1 | The interstitial hydrogen molecule | 143 |
| 8.9.2 | The H_2^* defect | 143 |
| 8.10 | Summary | 144 |
| 9 | Conclusions | 145 |
| A | Piezospectroscopic formulas for a trigonal defect centre | 149 |
| B | List of symbols | 153 |
| C | List of publications | 156 |
| | Bibliography | 159 |

Chapter 1

Introduction

1.1 Motivation

Hydrogen in silicon has been intensively studied during the past two decades by experimentalists as well as theoreticians. The topic is of considerable interest to the semiconductor industry as inevitably hydrogen is incorporated into silicon during processing of electronic devices. Sources of hydrogen introduction include several cleaning and etching procedures and high temperature treatments. As discussed below, the presence of hydrogen can seriously alter the electronic properties of the silicon material, hence possibly affecting and degrading device performance. Further, the effects of hydrogen and other impurities become more important as device scales are reduced.

The effects of hydrogen in crystalline silicon are manifold. Monoatomic hydrogen is a fast diffusing species that readily interacts with other defects in the crystal, including vacancies, self-interstitials, dopants, oxygen, carbon and transition metals. The resulting complexes usually possess different electronic properties to those of the original defect. In some cases, the electrical activity is completely removed by the interactions with hydrogen, the most pronounced example being the passivation of active dopants by the formation of donor-hydrogen and acceptor-hydrogen pairs. In other cases, electronic energy levels are introduced into the band gap or displaced within the gap by the interactions with hydrogen. Typical examples are the iso-valent defect of substi-

tutional carbon, which is activated by the formation of the hydrogen-carbon pair, and various radiation induced defects, which have their electronic energy levels shifted by attachment of hydrogen atoms. In addition to interacting with other defects, hydrogen may also exist in the form of molecules or larger extended defects, such as platelets. A hot topic in the field is the optical activity of the interstitial hydrogen molecule, which was undetected for years. Finally, hydrogen can act as a catalyzer for other processes, such as the diffusion of oxygen. Considerable progress has been made over the past two decades in the understanding of these intriguing properties. Yet, many issues remain unresolved. Reviews on hydrogen in silicon have been given by Pearton et al. [Pearton 1992], Estreicher [Estreicher 1995] and Jones et al. [Jones 2000].

1.2 Approach

The aim of this thesis is to study the electronic properties of several hydrogen-related defect systems in silicon. In this, a number of the issues presented above are highlighted and discussed. The methods used for hydrogenations are chemical etching, proton implantation and remote plasma treatment. Our main experimental techniques are conventional deep-level transient spectroscopy (DLTS) and Laplace transform DLTS. Central to this work are uniaxial stress measurements used in combination with Laplace transform DLTS. The uniaxial stress technique has been utilized for decades to characterize defects in semiconductors but has never found widespread use in combination with DLTS. The principal reason for this is the poor energy resolution associated with the conventional DLTS technique, which allows reliable stress measurements to be carried out only for the most shallow energy levels. This limitation is overcome by taking advantage of the much higher energy resolution offered by Laplace transform DLTS. Through the last few years, we have gained considerable experience in using the technique of uniaxial stress combined with Laplace transform DLTS and have developed an experimental approach that allows examination of several properties of a given defect, including its point symmetry, piezospectroscopic tensor and reorientation kinetics. This

is valuable information, which allows direct comparison with data from other experimental techniques and theoretical modeling. A number of such uniaxial stress studies are presented in the thesis.

1.3 Organization

The thesis is divided into nine chapters. In Chapter 2, we describe aspects of semiconductor theory relevant to the thesis and introduce the concept of deep centres and their electrical activity. Further, an introduction to piezospectroscopic theory, which forms the foundation for the interpretation of uniaxial stress measurements, is given. In Chapter 3, various experimental and theoretical techniques used for characterization of defects in semiconductors are presented. The main focus is on conventional DLTS and Laplace transform DLTS, which are used for the majority of the experimental work. The techniques of secondary ion mass spectroscopy (SIMS), electron paramagnetic resonance (EPR), infrared absorption spectroscopy and theoretical modeling of defects are briefly introduced. The experimental results and discussions of these are presented in Chapters 4, 5, 6, 7 and 8. In Chapter 4, we consider the incorporation of hydrogen into n-type silicon by remote plasma treatment. The total amount and the form of hydrogen introduced under various experimental conditions is quantified by SIMS, capacitance-voltage measurements and DLTS. In Chapter 5, we consider the electronic and piezospectroscopic properties of the hydrogen-carbon pair in n-type silicon. This work was a collaborative study between UMIST and the semiconductor groups at the universities in Aarhus and Exeter. In Chapter 6, a detailed piezospectroscopic analysis of the vacancy-oxygen complex in silicon is given. Though not related to hydrogen, this work establishes some important conclusions and demonstrates the full use of uniaxial stress combined with Laplace transform DLTS. The piezospectroscopic analysis of the vacancy-oxygen complex was a collaborative study between UMIST and the semiconductor groups at the universities in Aarhus, Grenoble and Warsaw. In Chapter 7, we consider the interactions of hydrogen with radiation induced defects in electron

irradiated n-type and p-type silicon hydrogenated by remote plasma treatment. Some general trends are discussed and the interactions with the vacancy-oxygen complex and the divacancy are examined in detail. In Chapter 8, we present the observation of capacitance changes with opposite sign to those related to majority carrier emission from deep energy levels in the band gap. The properties of these unusual capacitance changes are analyzed in detail and a model that goes some way towards explaining the effect is presented. Finally, in Chapter 9, the thesis is summarized.

Chapter 2

Deep level defects in semiconductors

This chapter describes aspects of semiconductor theory and introduces the concept of defects and their electrical properties [Ashcroft 1976], [Sze 1985], [Blood 1992]. We consider the capture and emission processes responsible for the electronic interactions of a deep energy level with the conduction band and the valence band. Finally, the influence of uniaxial stress on a defect within a semiconductor is described in some detail [Nye 1957], [Kaplyanskii 1961], [Kaplyanskii 1964].

2.1 Crystal structure and band structure

In a solid, the ions are arranged in a periodic lattice and each electron interacts with the surrounding ion lattice and with the other electrons in the crystal. The electron energy states are determined by a solution of the Schrödinger equation with an effective one-electron potential representing these interactions. The solution yields a set of continuous functions $\varepsilon_n(\mathbf{k})$, where \mathbf{k} is the wave vector and n is an integer labelled the band index. The energy states $\varepsilon_n(\mathbf{k})$ form the band structure of the solid. For a semiconductor, all energy bands are either completely filled or completely empty in the ground state. Thus, we can define the band gap energy E_g as the energy difference

between the minimum E_c of the conduction band (the lowest empty band) and the maximum E_v of the valence band (the highest filled band). Conduction electrons and valence holes can be described as free particles with effective masses governed by an effective mass tensor.

Completely filled and completely empty energy bands are electrically inert. Consequently, the electrical properties of a semiconductor are mainly determined by the density n_c of conduction electrons and the density p_v of valence holes. These values are obtained from the densities of energy states in the bands and the Fermi-Dirac probability of their occupancy¹. For a non-degenerated semiconductor, n_c and p_v are given by:

$$n_c = N_c \exp\left(-\frac{E_c - E_F}{k_B T}\right), \quad (2.1)$$

$$p_v = P_v \exp\left(-\frac{E_F - E_v}{k_B T}\right), \quad (2.2)$$

where N_c and P_v are the effective densities of states in the bands and E_F is the semiconductor Fermi energy. These expressions are general but the Fermi level position depends critically on impurities in the semiconductor.

Throughout this work, the semiconductor silicon is used. Silicon has a diamond lattice structure in which each silicon atom is surrounded by four nearest neighbor atoms forming a regular tetrahedron (Figure 2.1). The silicon lattice constant is 5.43 Å. The conduction band has six equivalent energy minima located along the $\langle 100 \rangle$ directions in \mathbf{k} -space and there are two degenerate valence band maxima located at $\mathbf{k} = \mathbf{0}$. The band gap energy at room temperature is $E_g = 1.12$ eV. The room temperature effective densities of states in the bands are given by $N_c = 2.86 \times 10^{19} \text{ cm}^{-3}$ and $P_v = 3.10 \times 10^{19} \text{ cm}^{-3}$, respectively [Green 1990]. The room temperature effective electron and hole masses, which determine the average thermal velocities of carriers, are given by $m_c^* = 0.28m$ and $m_v^* = 0.41m$, respectively, where m is the free electron mass [Green 1990].

¹The Fermi-Dirac distribution function is given by $f_{FD}(E) = \left(1 + \exp\left(\frac{E - E_F}{k_B T}\right)\right)^{-1}$, where E_F is the semiconductor Fermi energy.

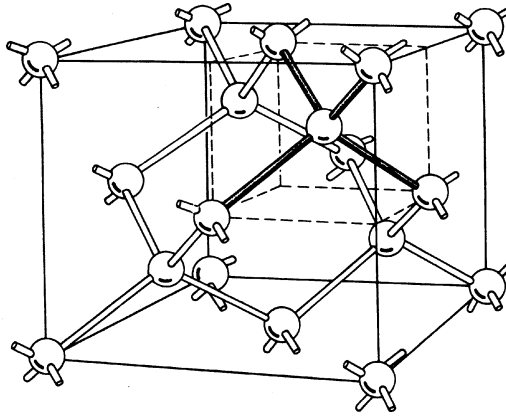


Figure 2.1: Diamant crystal structure. From [Sze 1985].

2.2 Shallow and deep energy levels

The presence of defects in the crystal can significantly alter the electrical properties of the semiconductor. The lattice imperfections distort the electronic potential and may result in the introduction of energy levels into the “forbidden” band gap. Typical examples of defects are chemical impurities, missing atoms in the lattice structure or combinations of the two. A large range of these types of defects exist in real semiconductor material, either as a result of intentional incorporation to control the electrical properties of the semiconductor or through unintentional contamination during crystal growth or subsequent processing.

The defect energy levels are usually categorized as either shallow or deep. In the case of silicon, shallow energy levels are introduced by doping the crystal with atoms from group III or group V of the periodic table. These dopants mainly occupy substitutional positions in the silicon lattice by forming covalent bonds with the four neighboring host atoms. The addition of a substitutional group V (group III) impurity can be represented as a fixed charge $+e$ ($-e$) on top of a host atom along with an additional electron (hole). This system forms a weak hydrogen-like potential with a small binding energy between the electron (hole) and the dopant. Dopants from group V (e.g. phosphorous with ionization energy 0.044 eV) and group III (e.g. boron with ionization energy 0.046 eV) are labelled donors and acceptors, respectively. A semiconductor doped with donors

(acceptors) is called n-type (p-type) due to the excess of conduction electrons (valence holes) in comparison to the other carrier type. The doping densities used in this work are in the range 10^{14} - 10^{17} cm^{-3} .

Other defects form a much stronger electronic potential that binds the carriers more efficiently. These deep level defects (or traps) introduce energy levels deeper in the band gap at a position denoted E_t . In thermodynamic terms, the band structure represents Gibbs free energies. Thus, the ionization energy $E_c - E_t$ is correctly interpreted as the change ΔG_n in Gibbs energy by the excitation of an electron from the deep level to the conduction band, i.e. the Gibbs energy difference between (i) the empty centre and a conduction electron and (ii) the centre with a trapped electron. Thus,:

$$E_c(T) - E_t(T) = \Delta G_n(T) = \Delta H_n - T\Delta S_n, \quad (2.3)$$

where ΔH_n and ΔS_n are the corresponding changes in enthalpy and entropy, respectively. A similar result applies to the hole ionization energy $E_t - E_v$.

Unlike shallow dopants, deep level defects can often exist in more than two charge states. As a result of Coulombic interaction between the carrier and the charged centre, an electron is usually more strongly bound to a positively charged centre than to a neutral or negatively charged centre. This natural sequence of levels is illustrated in Figure 2.2 and defines a so-called positive-U system. We talk about a negative-U

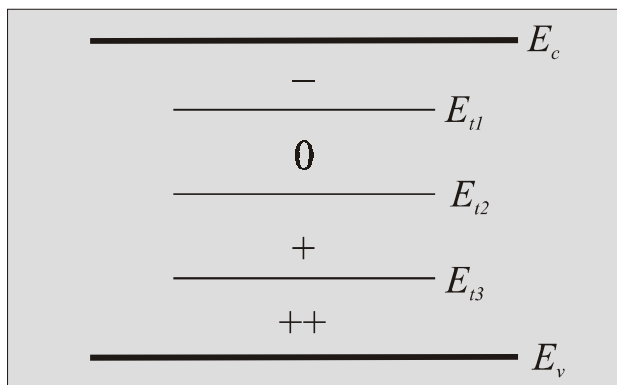


Figure 2.2: Deep energy levels of an arbitrary defect centre, which can exist in four charge states. The absolute charge state of the defect is indicated for different positions of the Fermi level.

system if this sequence is reversed, usually as a result of charge state dependent lattice relaxations. The charge state of a deep energy level is labelled in accordance with the absolute charge states of the defect before and after carrier emission. A transition from a negatively charged defect to a neutrally charged defect by electron emission is labelled $(-/0)$ and is also called a single acceptor level, while a transition from a positively charged defect to a neutrally charged defect by hole emission is labelled $(+/0)$ and is also called a single donor level.

2.3 Interactions with the conduction and the valence band

2.3.1 The rate equation

Consider a trap of volume density N_t , which introduces a deep energy level into the band gap at position E_t . The level can interact with the conduction band and the valence band through emission and capture of electrons and holes. Thus, the following four processes need to be considered (Figure 2.3):

- Emission of electrons to the conduction band with emission rate e_n .
- Emission of holes to the valence band with emission rate e_p .
- Capture of electrons from the conduction band with capture rate c_n .
- Capture of holes from the valence band with capture rate c_p .

The volume density n_t of filled traps is determined by the competition of these four processes. The emission of electrons and the capture of holes takes place from the n_t filled traps, while the emission of holes and the capture of electrons takes place from the $(N_t - n_t)$ empty traps. Thus, the interactions are described by the rate equation:

$$\frac{dn_t}{dt} = -(e_n + c_p)n_t + (c_n + e_p)(N_t - n_t). \quad (2.4)$$

Equation (2.4) forms the basis for mapping deep level defects by deep-level transient spectroscopy. The steady-state occupancy ratio of the trap is determined by the con-

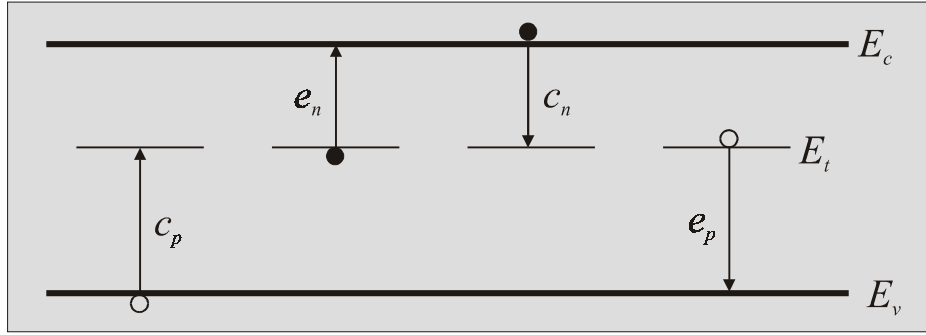


Figure 2.3: Interactions between a deep energy level and the two bands. Electrons and holes are represented by filled and open symbols, respectively.

dition $\frac{dn_t}{dt} = 0$ as:

$$\frac{n_t(\infty)}{N_t} = \frac{c_n + e_p}{e_n + c_n + e_p + c_p}. \quad (2.5)$$

In n-type material², we have particular interest in the two special cases, where (i) all traps are initially empty and electron capture is the dominant process and (ii) all traps are initially filled and electron emission is the dominant process. In these cases, the solution to equation (2.4) is given by:

$$n_t(t) = N_t (1 - \exp(-c_n t)) \quad n_t(0) = 0, \quad c_n \gg e_n, e_p, c_p, \quad (2.6)$$

$$n_t(t) = N_t \exp(-e_n t) \quad n_t(0) = N_t, \quad e_n \gg c_n, e_p, c_p. \quad (2.7)$$

Thus, the volume density n_t of filled traps relaxes exponentially towards the steady-state values $n_t(\infty) = N_t$ for the capture process and $n_t(\infty) = 0$ for the emission process. The time constants for the processes are given by the inverse capture rate c_n^{-1} and the inverse emission rate e_n^{-1} , respectively.

2.3.2 The capture process

The electron capture rate c_n is proportional to the flux of conduction electrons (electrons per unit area per unit time) that passes the centre. Thus:

$$c_n = \sigma_n \langle v_n \rangle n_c, \quad (2.8)$$

²In the remaining part of this chapter, we mainly focus on electrons in n-type material. An analogue description can be given for holes in p-type material.

where:

$$\langle v_n \rangle = \sqrt{\frac{3k_B T}{m_c^*}} \quad (2.9)$$

is the average thermal velocity of conduction electrons and the proportionality constant σ_n is the electron capture cross section with units of area. The value of the capture cross section is on the order of atomic dimensions and describes the effectiveness of the centre to capture electrons. The product $\sigma_n \langle v_n \rangle$ is known as the capture coefficient (units of $\text{cm}^3 \text{s}^{-1}$). The capture cross section can be independent of temperature or can be thermally activated. In the latter case, the cross section is usually found to follow the behavior:

$$\sigma_n(T) = \sigma_n^\infty \exp\left(-\frac{E_{\sigma_n}}{k_B T}\right), \quad (2.10)$$

where E_{σ_n} is the energy barrier for capture of electrons and σ_n^∞ is the electron capture cross section in the limit $T \rightarrow \infty$ [Henry 1977]. In most cases, the value of the carrier capture cross section can indicate the charge state of the defect centre emptied for carriers. For Coulombically-attractive centres, the carrier capture cross section is expected to be $\gtrsim 10^{-14} \text{ cm}^2$, while one expects this value to be in the range 10^{-16} - 10^{-14} cm^2 for a neutral centre and $\lesssim 10^{-17} \text{ cm}^2$ for a repulsive centre.

2.3.3 The emission process

In thermodynamic equilibrium, the principle of detailed balance applies. This principle states that the exchange of electrons between the deep level and the conduction band and the exchange of holes between the deep level and the valence band are both balanced, i.e. $e_n n_t = c_n (N_t - n_t)$ and $e_p (N_t - n_t) = c_p n_t$. Combining this principle with Fermi-Dirac statistics yields the electron emission rate:

$$e_n = \sigma_n \langle v_n \rangle \frac{g_0}{g_1} N_c \exp\left(-\frac{E_c - E_t}{k_B T}\right), \quad (2.11)$$

where g_0 and g_1 are the degeneracies of the empty and filled energy level, respectively. The temperature dependence of the electron emission rate is determined from the temperature dependencies of the thermal velocity (2.9), the electron capture cross

section (2.10), the ionization energy (2.3) and the effective density of states ($N_c \propto T^{3/2}$ [Green 1990]). The result is:

$$e_n(T) = \gamma_n T^2 \sigma_n^a \exp\left(-\frac{E_n^a}{k_B T}\right), \quad (2.12)$$

where:

$$E_n^a = \Delta H_n + E_{\sigma_n}, \quad (2.13)$$

$$\sigma_n^a = \frac{g_0}{g_1} \sigma_n^\infty \exp(\Delta S_n / k_B), \quad (2.14)$$

and γ_n is a constant. Thus, a plot of $\ln(e_n/T^2)$ versus inverse temperature T^{-1} (an Arrhenius plot) gives a straight line with slope and intersection of the e_n/T^2 axis characterized by the activation energy E_n^a and the apparent electron capture cross section σ_n^a , respectively. This, however, does not directly determine the ionization energy $E_c - E_t$ and the true electron capture cross section σ_n . In the case of temperature-independent electron capture, the activation energy E_n^a equals the enthalpy change ΔH_n for the emission process. The emission rate e_p for emission of holes to the valence band is described by expressions similar to equations (2.11) and (2.12).

In some cases, the presence of an electric field can stimulate the thermal emission of a carrier from a defect. For Coulombically-attractive centres, the enhancement of the emission rate is often caused by a lowering of the barrier associated with the Coulomb potential. The theory of this effect, known as the Poole-Frenkel effect, was originally developed by Frenkel and was later extended to a three dimensional model by Hartke [Hartke 1968]. For an electron attracted to a singly positively charged centre and under the influence of a uniform electric field \mathcal{E} , the ratio between the emission rate $e_n(\mathcal{E})$ in the electric field and the zero-field emission rate $e_n(0)$ is given by:

$$\frac{e_n(\mathcal{E})}{e_n(0)} = \omega^{-2} [1 + (\omega - 1) \exp(\omega)] + \frac{1}{2}, \quad (2.15)$$

where the field parameter $\omega = \frac{\sqrt{e^3 \mathcal{E} / \pi \epsilon_s}}{k_B T}$ and ϵ_s is the semiconductor dielectric constant [Hartke 1968]. Thus, the observation of a Poole-Frenkel effect is indicative of a charged defect centre. However, an enhancement of the emission rate in an electric field must be

interpreted with care as other mechanisms (e.g. tunneling and impact ionization) can produce a similar effect for neutral as well as charged centres. Recently, the problem of distinction between these effects was considered by Ganichev et al. [Ganichev 2000]. It was concluded that, for Coulombically-attractive centres, the Poole-Frenkel effect is the dominant effect at relatively low electric field strengths. At larger field strengths, the stimulation of the emission process is dominated by phonon assisted tunneling, which enhances the emission rate exponentially with the square of the electric field strength. For neutral centres, phonon assisted tunneling is the dominant effect even at small fields.

2.4 Piezospectroscopic theory

2.4.1 Stress

Consider a three dimensional body and a unit cube within the body with edges parallel to the axes Ox_1 , Ox_2 , Ox_3 . An external force applied to the body will exert forces on the cube surfaces by the material surrounding it. The force exerted per unit area is denoted the stress. We will discuss only the case of homogeneous stress, where the stress state of the cube is independent of its position in the body. The stress transmitted across each surface of the cube may be resolved into three components along Ox_1 , Ox_2 , Ox_3 . We denote by σ_{ij} ($i, j = 1, 2, 3$) the stress component in the $+Ox_i$ direction transmitted across the surface perpendicular to the Ox_j direction. The components σ_{ij} ($i = j$) and the components σ_{ij} ($i \neq j$) are denoted the normal and the shear stress, respectively. The normal stress represents a change in the length of the edges in the unit cube, while the shearing stress represents a change of the angles between the edges. It can be shown that the stress tensor defined by:

$$[\sigma_{ij}] = \begin{bmatrix} \sigma_{11} & \sigma_{12} & \sigma_{13} \\ \sigma_{21} & \sigma_{22} & \sigma_{23} \\ \sigma_{31} & \sigma_{32} & \sigma_{33} \end{bmatrix} \quad (2.16)$$

forms a symmetric second-rank tensor [Nye 1957]. The symmetry of the stress tensor means that it contains only six independent components, which are conveniently represented in the stress vector $\boldsymbol{\sigma} = (\sigma_{11}, \sigma_{22}, \sigma_{33}, \sigma_{32}, \sigma_{31}, \sigma_{12})$.

The stress used throughout this work is compressive uniaxial stress. It follows from the definition of stress given above that compressive stress corresponds to negative values of the normal stress components σ_{ii} . The minus sign of the compressive stress will be given explicitly. The components σ_{ij} of the stress tensor are obtained as:

$$\sigma_{ij} = -P \cos(Ox_i, \mathbf{P}) \cos(Ox_j, \mathbf{P}) \quad i, j = 1, 2, 3, \quad (2.17)$$

where $P > 0$ is the magnitude of the applied stress and (Ox_i, \mathbf{P}) is the angle between the stress direction and the Ox_i axis. Throughout this work, the stress directions are the three major crystallographic directions, $\langle 100 \rangle$, $\langle 110 \rangle$ and $\langle 111 \rangle$.

2.4.2 Strain

Closely related to stress is the concept of strain, which deals with the displacements of points in a body relative to one another. Consider a three dimensional body deformed by an externally applied force. Let a point with coordinates (x_1, x_2, x_3) move to a point with coordinates $(x_1 + u_1, x_2 + u_2, x_3 + u_3)$ as a result of the deformation. We define the strain tensor $[\varepsilon_{ij}]$ by the nine components:

$$\varepsilon_{ij} = \frac{1}{2} \left(\frac{\partial u_i}{\partial x_j} + \frac{\partial u_j}{\partial x_i} \right) \quad i, j = 1, 2, 3. \quad (2.18)$$

It can be shown that $[\varepsilon_{ij}]$ forms a symmetric second-rank tensor and that it represents a satisfactory measure of the state of strain in the body [Nye 1957]. Similar to the stress vector $\boldsymbol{\sigma}$, we introduce the strain vector $\boldsymbol{\varepsilon} = (\varepsilon_{11}, \varepsilon_{22}, \varepsilon_{33}, 2\varepsilon_{32}, 2\varepsilon_{31}, 2\varepsilon_{12})$.

Hooke's law states that the amount of elastic strain in a body subjected to a stress is proportional to the magnitude of the applied stress. In the general case, each strain component ε_{ij} is linearly related to all the components of the stress, i.e.:

$$\varepsilon_{ij} = \sum_{k,l} s_{ijkl} \sigma_{kl} \quad i, j = 1, 2, 3, \quad (2.19)$$

where the constants s_{ijkl} are the compliances of the crystal. It can be shown that $[s_{ijkl}]$ forms a fourth-rank tensor and that only 36 of the 81 components are independent [Nye 1957]. Direct evaluation of equation (2.19) shows that the components of the strain vector $\boldsymbol{\varepsilon}$ and the stress vector $\boldsymbol{\sigma}$ are related by a 6×6 matrix in the following way:

$$\begin{pmatrix} \varepsilon_{11} \\ \varepsilon_{22} \\ \varepsilon_{33} \\ 2\varepsilon_{32} \\ 2\varepsilon_{31} \\ 2\varepsilon_{12} \end{pmatrix} = \begin{pmatrix} s_{11} & s_{12} & s_{13} & s_{14} & s_{15} & s_{16} \\ s_{21} & s_{22} & s_{23} & s_{24} & s_{25} & s_{26} \\ s_{31} & s_{32} & s_{33} & s_{34} & s_{35} & s_{36} \\ s_{41} & s_{42} & s_{43} & s_{44} & s_{45} & s_{46} \\ s_{51} & s_{52} & s_{53} & s_{54} & s_{55} & s_{56} \\ s_{61} & s_{62} & s_{63} & s_{64} & s_{65} & s_{66} \end{pmatrix} \begin{pmatrix} \sigma_{11} \\ \sigma_{22} \\ \sigma_{33} \\ \sigma_{32} \\ \sigma_{31} \\ \sigma_{12} \end{pmatrix}, \quad (2.20)$$

where the components s_{mn} are defined by:

$$\begin{aligned} s_{mn} &= s_{ijkl} & m = 1, 2, 3 \text{ and } n = 1, 2, 3, \\ s_{mn} &= 2s_{ijkl} & m = 4, 5, 6 \text{ or } n = 4, 5, 6, \\ s_{mn} &= 4s_{ijkl} & m = 4, 5, 6 \text{ and } n = 4, 5, 6, \end{aligned} \quad (2.21)$$

using the suffix abbreviation $11 \rightarrow 1, 22 \rightarrow 2, 33 \rightarrow 3, 23 \rightarrow 4, 32 \rightarrow 4, 31 \rightarrow 5, 13 \rightarrow 5, 12 \rightarrow 6, 21 \rightarrow 6$ for the transformations $ij \rightarrow m, kl \rightarrow n$ [Nye 1957]. These definitions allow us to represent the strain-stress relation in the matrix form (2.20). The number of non-zero components in the compliance matrix and the values of these components depend on the specific structure of the material under study. In the case of crystalline silicon with cubic O_h symmetry,:

$$\begin{pmatrix} \varepsilon_{11} \\ \varepsilon_{22} \\ \varepsilon_{33} \\ 2\varepsilon_{32} \\ 2\varepsilon_{31} \\ 2\varepsilon_{12} \end{pmatrix} = \begin{pmatrix} s_{11} & s_{12} & s_{12} & 0 & 0 & 0 \\ s_{12} & s_{11} & s_{12} & 0 & 0 & 0 \\ s_{12} & s_{12} & s_{11} & 0 & 0 & 0 \\ 0 & 0 & 0 & s_{44} & 0 & 0 \\ 0 & 0 & 0 & 0 & s_{44} & 0 \\ 0 & 0 & 0 & 0 & 0 & s_{44} \end{pmatrix} \begin{pmatrix} \sigma_{11} \\ \sigma_{22} \\ \sigma_{33} \\ \sigma_{32} \\ \sigma_{31} \\ \sigma_{12} \end{pmatrix}, \quad (2.22)$$

where $s_{11} = 7.68 \times 10^{-3} \text{ GPa}^{-1}$, $s_{12} = -2.14 \times 10^{-3} \text{ GPa}^{-1}$ and $s_{44} = 12.56 \times 10^{-3} \text{ GPa}^{-1}$ [Nye 1957]. Thus, we have established a way to transform an externally applied uniaxial stress to the corresponding state of strain in the silicon crystal.

2.4.3 Influence of stress on defect total energy

Consider a defect centre in a semiconductor subjected to an external uniaxial stress. The total energy E of the defect is modified by the stress in the linear form:

$$\Delta E = \sum_{i,j} B_{ij} \varepsilon_{ij}, \quad (2.23)$$

where B_{ij} are components of the defect piezospectroscopic tensor, also called the $\bar{\mathbf{B}}$ tensor [Kaplyanskii 1964]. The specific form of the tensor for a centre of a given point-group symmetry is obtained by applying the symmetry operations of the point-group to the centre. In this, the form of the tensor remains unchanged, hence imposing restrictions on the components B_{ij} . Thus, the defect symmetry reduces the number of independent component in the piezospectroscopic tensor, i.e. the higher symmetry the fewer independent components. Table 2.1 gives the form of the tensor in (x, y, z) coordinates for the possible point-groups of defects in crystalline silicon. The point-groups have been divided into symmetry systems³ and the two suffixes in the B_{ij} components have been abbreviated into a single one running from 1 to 6. For the triclinic symmetry system, all six components of the piezospectroscopic tensor are independent, while for the monoclinic there are four independent components; for the orthorhombic, three; for the tetragonal and trigonal, two and for the cubic, one. The piezospectroscopic tensor is identical for the various point-groups within a given symmetry system.

The piezospectroscopic tensor is always symmetric, irrespective of the actual symmetry class of the given defect centre. Consequently, the tensor can be diagonalized.

³There exist 32 different point-groups, which are conveniently divided into seven symmetry systems in accordance with the symmetry elements they possess. The systems are: triclinic, monoclinic, orthorhombic, tetragonal, trigonal, hexagonal and cubic. The monoclinic and orthorhombic systems are further divided into two separate systems labelled I and II. A general description of point groups and symmetry systems is given in [Nye 1957].

| System | Point-groups | $\bar{\mathbf{B}}$ tensor | Eigenvalues and -vectors |
|-----------------|--------------------------------------|---|--|
| Triclinic | C_1, S_2 | $\begin{bmatrix} B_1 & B_6 & B_5 \\ B_6 & B_2 & B_4 \\ B_5 & B_4 & B_3 \end{bmatrix}$ | |
| Monoclinic-I | C_{1h}, C_{2h}, C_2 | $\begin{bmatrix} B_2 & B_3 & -B_4 \\ B_3 & B_2 & B_4 \\ -B_4 & B_4 & B_1 \end{bmatrix}$ | |
| Monoclinic-II | C_2 | $\begin{bmatrix} B_2 & B_4 & 0 \\ B_4 & B_3 & 0 \\ 0 & 0 & B_1 \end{bmatrix}$ | |
| Orthorhombic-I | C_{2v} | $\begin{bmatrix} B_2 & B_3 & 0 \\ B_3 & B_2 & 0 \\ 0 & 0 & B_1 \end{bmatrix}$ | (B_1) [001] $(B_2 - B_3)$ $[\bar{1}\bar{1}0]$ $(B_2 + B_3)$ [110] |
| Orthorhombic-II | D_2 | $\begin{bmatrix} B_1 & 0 & 0 \\ 0 & B_2 & 0 \\ 0 & 0 & B_3 \end{bmatrix}$ | (B_1) [100] (B_2) [010] (B_3) [001] |
| Trigonal | $C_3, S_6, C_{3v},$ D_3, D_{3d} | $\begin{bmatrix} B_1 & B_2 & B_2 \\ B_2 & B_1 & B_2 \\ B_2 & B_2 & B_1 \end{bmatrix}$ | $(B_1 - B_2)$ $[\bar{1}\bar{1}0]$ $(B_1 - B_2)$ [11 $\bar{2}$] $(2B_2 + B_1)$ [111] |
| Tetragonal | S_4, D_{2d} | $\begin{bmatrix} B_2 & 0 & 0 \\ 0 & B_2 & 0 \\ 0 & 0 & B_1 \end{bmatrix}$ | (B_2) [100] (B_2) [010] (B_1) [001] |
| Cubic | T, T_d | $\begin{bmatrix} B_1 & 0 & 0 \\ 0 & B_1 & 0 \\ 0 & 0 & B_1 \end{bmatrix}$ | (B_1) [100] (B_1) [010] (B_1) [001] |

Table 2.1: Form of the piezospectroscopic tensor in (x, y, z) coordinates for the possible point-groups of defect centres in crystalline silicon. The point-groups have been divided into symmetry systems. Eigenvalues and corresponding eigenvectors for the tensors are given for the higher symmetry classes.

Eigenvalues and eigenvectors for the piezospectroscopic tensors of the higher symmetries are given in Table 2.1. This change of coordinate system can be convenient because it allows a more direct interpretation of the piezospectroscopic parameters associated with the defect, i.e. the total energy of the defect compressed along one of the principal axes is changed by an amount given by the corresponding eigenvalue. A positive eigenvalue shows that the defect total energy is lowered by compressive stress applied along the corresponding principal axis (we use the sign convention that compressive stress is negative).

A defect centre in an unstrained crystal has a certain orientational degeneracy. The multiplicity of this degeneracy is obtained as the ratio between the order of the symmetry group of the crystal (48 for silicon with cubic O_h symmetry) and the order of the symmetry group of the defect centre [Kaplyanskii 1964]. The multiplicity is 1 for cubic, 3 for tetragonal, 4 for trigonal, 6 for orthorhombic, 12 for monoclinic and 24 for triclinic centres in a silicon crystal. These orientations are equivalent in the unstrained crystal but a uniaxial stress can partly lift the degeneracy. For a given direction of stress, the number of non-equivalent orientations and their remaining degeneracy is obtained by considering the possible different orientations of the centre relative to the stress. An example of this approach is given in Appendix A for the trigonal symmetry. Table 2.2 (column 3) gives the remaining degeneracy of the non-equivalent orientations for orthorhombic-I and trigonal centres in a silicon crystal stressed along the three major crystallographic directions, $\langle 100 \rangle$, $\langle 110 \rangle$ and $\langle 111 \rangle$.

The change ΔE in total energy of the various non-equivalent orientations is calculated from equation (2.23). The strain vector $\boldsymbol{\varepsilon}$ is obtained from the stress vector $\boldsymbol{\sigma}$ by the stress-strain relation (2.22), while the form of the piezospectroscopic tensor $\bar{\mathbf{B}}$ for the different symmetry classes is given in Table 2.1. The calculation of ΔE can be carried out in (x, y, z) coordinates or in the coordinate system defined by the principal axes of the tensor. Table 2.2 gives the calculated energy shifts per unit stress $\Delta E/P$ for the various non-equivalent orientations for orthorhombic-I and trigonal centres in a silicon crystal stressed along the $\langle 100 \rangle$, $\langle 110 \rangle$ and $\langle 111 \rangle$ directions. An example

| System | P | Deg. | Total energy shift per unit stress, $\Delta E/P$ |
|---------------|-----------------------|--|---|
| Ortho-rhombic | $\langle 100 \rangle$ | 4 | $-B_1 s_{12} - B_2 (s_{11} + s_{12})$ |
| | | 2 | $-B_1 s_{11} - 2B_2 s_{12}$ |
| I | $\langle 110 \rangle$ | 1 | $-B_1 s_{12} - B_2 (s_{11} + s_{12}) - \frac{1}{2} B_3 s_{44}$ |
| | | 4 | $-\frac{1}{2} B_1 (s_{11} + s_{12}) - \frac{1}{2} B_2 (s_{11} + 3s_{12})$ |
| | | 1 | $-B_1 s_{12} - B_2 (s_{11} + s_{12}) + \frac{1}{2} B_3 s_{44}$ |
| | $\langle 111 \rangle$ | 3 | $-\frac{1}{3} B_1 (s_{11} + 2s_{12}) - \frac{2}{3} B_2 (s_{11} + 2s_{12}) - \frac{1}{3} B_3 s_{44}$ |
| | | 3 | $-\frac{1}{3} B_1 (s_{11} + 2s_{12}) - \frac{2}{3} B_2 (s_{11} + 2s_{12}) + \frac{1}{3} B_3 s_{44}$ |
| Trigonal | $\langle 100 \rangle$ | 4 | $-B_1 (s_{11} + 2s_{12})$ |
| | | 2 | $-B_1 (s_{11} + 2s_{12}) - \frac{1}{2} B_2 s_{44}$ |
| | 2 | $-B_1 (s_{11} + 2s_{12}) + \frac{1}{2} B_2 s_{44}$ | |
| | $\langle 111 \rangle$ | 3 | $-B_1 (s_{11} + 2s_{12}) + \frac{1}{3} B_2 s_{44}$ |
| | | 1 | $-B_1 (s_{11} + 2s_{12}) - B_2 s_{44}$ |

Table 2.2: Degeneracies and total energy shifts per unit stress for the non-equivalent orientations of orthorhombic-I and trigonal defect centres in a silicon crystal stressed along the three major crystallographic directions. The components B_1 , B_2 and B_3 are defined as in Table 2.1.

of this calculation is given in Appendix A for the trigonal symmetry. The relations in Table 2.2 will be used throughout the thesis.

The displacement of the center of gravity of the split components for a given direction of stress is obtained as the weighed average of the various energy shifts. This “hydrostatic” term is determined by the trace of the defect piezospectroscopic tensor and is identical for all directions of the uniaxial stress. A hydrostatic stress, i.e. a stress from all sides of equal magnitude, shifts the components by a value that is a factor of three larger than the displacement of the center of gravity for an uniaxial stress. The hydrostatic component is determined by the change of crystal volume under application of the stress [Kaplyanskii 1961].

2.4.4 Total energy diagrams

Consider an arbitrary defect centre in a silicon crystal that can exist in two charge states $s - 1$ and s . We assume that a uniaxial stress $P > 0$ applied to the crystal gives rise to two non-equivalent configurations A and B . Figure 2.4 shows total energy diagrams for the charge states $s - 1$ and s of the centre under stress. The zero point of the energy scale has been chosen to equal the total energy of configuration A in charge state s .

Let us consider the influence of uniaxial stress on the electronic transition from charge state $s - 1$ to charge state s in configuration A . According to the piezospectroscopic theory described above, the total energy shifts linearly with the applied stress. We define by $\alpha_A = -(\Delta E_A(P) - \Delta E_A(0))/P$ the stress coefficient for the ionization process, where $\Delta E_A(P)$ is the change in total energy upon the transition from charge state $s - 1$ to charge state s in configuration A . A positive stress coefficient α_A (a negative value of $\Delta E_A(P) - \Delta E_A(0)$) means that the energy level approaches the conduction band for increasing stress. We assume that the stress dependence of the electron emission rate is given by equation (2.11). Thus, at a fixed temperature T_0 :

$$\frac{e_n(P, T_0)}{e_n(0, T_0)} = \frac{\sigma_n(P, T_0)}{\sigma_n(0, T_0)} \exp\left(\frac{\alpha_A P}{k_B T_0}\right). \quad (2.24)$$

Obviously, the value of the stress coefficient for a given orientation depends critically on the effect of stress on the conduction band. In order to eliminate this effect, we will always consider the difference between the stress coefficients for non-equivalent orientations (e.g. $\alpha_A - \alpha_B$). The magnitude of splitting is governed by the difference in the defect piezospectroscopic tensor for the two charge states involved in the transition.

Now, let us consider the defects in charge state s . The total energy difference between configurations A and B depends linearly on the applied stress and we define that configuration B is shifted in total energy by $-\alpha_{A,B}^s P$ relative to configuration A (Figure 2.4). The energy shift means that preferential alignment can occur as the defect seeks out the lowest energy configuration in respect to the applied stress. We describe the reorientation between configurations A and B as a thermally activated jump process

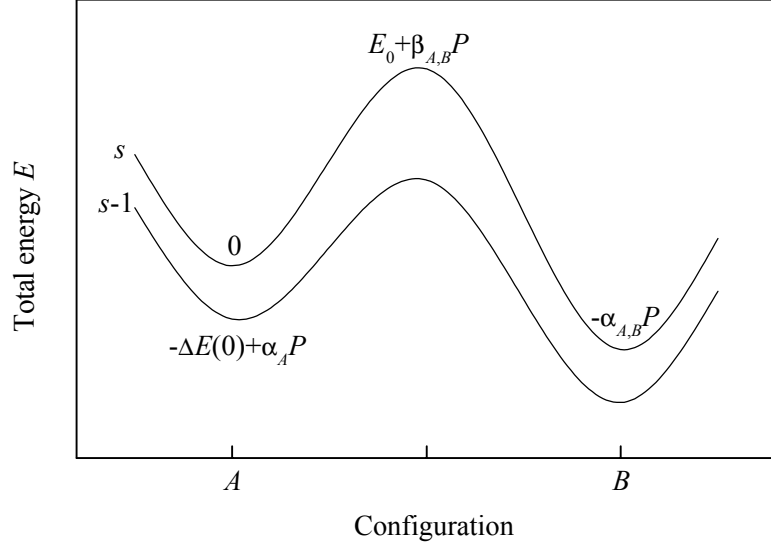


Figure 2.4: Total energy diagrams for the charge states $s - 1$ and s of an arbitrary defect centre under uniaxial stress. The stress introduces two non-equivalent configurations A and B of the centre.

over a classical energy barrier. The height of the barriers for the jump from A to B and the jump from B to A are given by $E_0^s + \beta_{A,B}^s P$ and $E_0^s + \beta_{A,B}^s P + \alpha_{A,B}^s P$, respectively, where E_0^s is the energy barrier at zero stress and $\beta_{A,B}^s$ is the stress coefficient for the barrier (Figure 2.4). A positive value of $\beta_{A,B}^s$ means that the barrier increases with the applied stress. From Boltzmann statistics, the rate constants $k_{A \rightarrow B}$ and $k_{B \rightarrow A}$ for the jumps $A \rightarrow B$ and $B \rightarrow A$ are given by:

$$k_{A \rightarrow B} = R_{A \rightarrow B} \exp\left(-\frac{E_0^s + \beta_{A,B}^s P}{k_B T}\right), \quad (2.25)$$

$$k_{B \rightarrow A} = R_{B \rightarrow A} \exp\left(-\frac{E_0^s + \beta_{A,B}^s P + \alpha_{A,B}^s P}{k_B T}\right), \quad (2.26)$$

where $R_{A \rightarrow B}$ and $R_{B \rightarrow A}$ are pre-exponential factors. The concentrations N_A and N_B of defects in configurations A and B are described by the rate equations:

$$\frac{dN_A}{dt} = -k_{A \rightarrow B} N_A + k_{B \rightarrow A} (N_t - N_A), \quad (2.27)$$

$$\frac{dN_B}{dt} = -k_{B \rightarrow A} N_B + k_{A \rightarrow B} (N_t - N_B), \quad (2.28)$$

where $N_t = N_A + N_B$ is the total concentration of the deep centre. The solutions to

equations (2.27) and (2.28) are given by:

$$N_A(t) = (N_A(0) - N_A(\infty)) \exp(-t/\tau) + N_A(\infty), \quad (2.29)$$

$$N_B(t) = (N_B(0) - N_B(\infty)) \exp(-t/\tau) + N_B(\infty), \quad (2.30)$$

where $\tau = (k_{A \rightarrow B} + k_{B \rightarrow A})^{-1}$. Thus, the concentrations N_A and N_B decay exponentially from their initial values to their steady-state values with a time constant given by $(k_{A \rightarrow B} + k_{B \rightarrow A})^{-1}$. The equilibrium value of N_A/N_B is obtained from the steady-state conditions $\frac{dN_A}{dt} = \frac{dN_B}{dt} = 0$ by using equations (2.27) and (2.28):

$$\frac{N_A(\infty)}{N_B(\infty)} = \frac{N_A}{N_B} \Big|_{P=0} \exp\left(-\frac{\alpha_{A,B}^s P}{k_B T}\right). \quad (2.31)$$

The general description given above will be used throughout the thesis for studying specific defects under uniaxial stress.

Chapter 3

Experimental techniques

In this chapter, we present a number of experimental and theoretical techniques used for characterization of defects in semiconductors. We begin by considering the experimental characterization of the Schottky diode [Sze 1985], [Blood 1992]. Then, we describe the technique deep-level transient spectroscopy (DLTS) in some detail [Lang 1974], [Blood 1992], [Dobaczewski 1994]. Finally, a number of other experimental and theoretical techniques of some importance to the present work are briefly presented. These are secondary ion mass spectroscopy (SIMS) [Schroder 1998], electron paramagnetic resonance (EPR) [Watkins 1961], infrared absorption spectroscopy [Schroder 1998] and theoretical modeling of defects [Estreicher 1995], [Jones 2000].

3.1 Schottky diode characterization

3.1.1 Energy band diagrams

A Schottky diode is formed when a metal of work function $e\phi_m$ and a n-type semiconductor of electron affinity $e\chi_n$ and work function $e\phi_s < e\phi_m$ are joined¹. The different positions of the Fermi levels in the isolated materials causes a diffusion of

¹The work function is defined as the energy required to excite an electron from the Fermi level to the vacuum level. The electron affinity is defined as the energy required to excite an electron from the conduction band to the vacuum level.

electrons from the semiconductor to the metal, leaving behind uncompensated donor ions in a depleted space charge region. In thermodynamic equilibrium, the energy band diagram of the Schottky diode is constructed from the requirements of constant Fermi level and continuous vacuum level, as illustrated in Figure 3.1. In the ideal case, the Schottky barrier from the metal to the semiconductor is given by $\phi_{Bn} = \phi_m - \chi_n$, while the built-in potential from the semiconductor to the metal is given by $V_{bi} = \phi_m - \phi_s$.

An externally applied bias will disturb the fine balance of electron transport across the junction and allow a net current to flow through the device. The junction is forward biased if a positive voltage V_F is applied to the metal with respect to the semiconductor. The junction is reverse biased if a positive voltage V_R is applied to the semiconductor with respect to the metal. The total potential across the junction is reduced to $V_{bi} - V_F$ in forward bias and increased to $V_{bi} + V_R$ in reverse bias, while the Schottky barrier is only weakly dependent on the applied bias. Real Schottky diodes show some deviations from this simple model but the above description is adequate for our use.

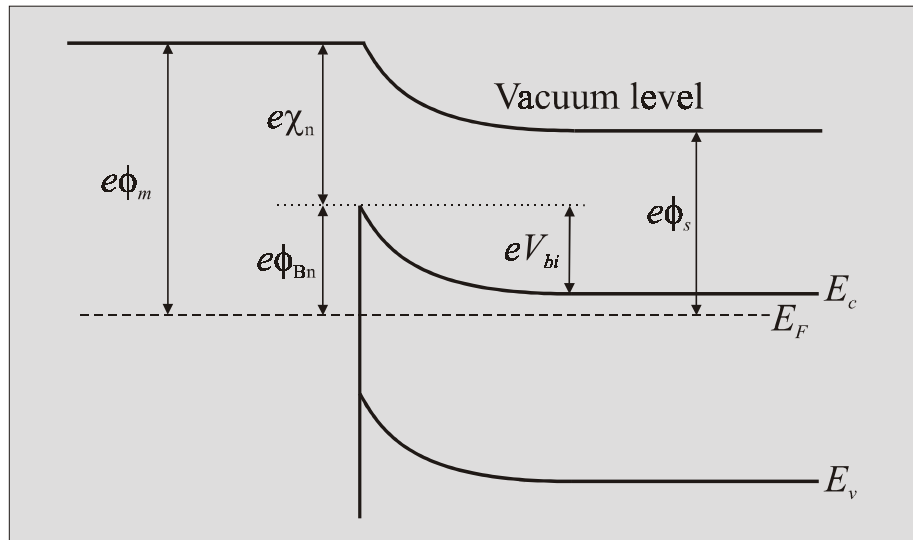


Figure 3.1: Energy band diagram of a Schottky diode in thermodynamic equilibrium. The meaning of the symbols is explained in the text.

3.1.2 The space charge region

The space charge region is characterized by the presence of uncompensated space charge due to partially or complete depletion of free carriers. The relation between the total potential V_{tot} across the junction and the width W of the space charge region for an arbitrary space charge density distribution $\rho(x)$ is obtained by integration of Poisson's equation, using the boundary condition that the band bending is zero in the electrically neutral region. The solution gives the general result:

$$V_{tot} = \frac{1}{\epsilon_s} \int_0^W x\rho(x)dx, \quad (3.1)$$

where $V_{tot} = V_{bi} - V_F$ in forward bias and $V_{tot} = V_{bi} + V_R$ in reverse bias [Blood 1992]. Assuming a uniform space charge density $\rho(x) = -eN_d$ in the space charge region, equation (3.1) reduces to:

$$W = \sqrt{\frac{2\epsilon_s V_{tot}}{eN_d}}. \quad (3.2)$$

In silicon, for a typical doping density of $N_d = 10^{15} \text{ cm}^{-3}$, the width of the space charge region is $\sim 1.1 \mu\text{m}$ in equilibrium and expands to $\sim 2.8 \mu\text{m}$ under reverse bias $V_R = 5 \text{ V}$.

We work under the assumption that no free carriers exist within the space charge region and that the boundary to the electrically neutral region is sharp. This assumption is known as the depletion approximation. In reality, there exist a small transition region, known as the Debye tail, which is only partly depleted for free carriers. The Debye length given by:

$$L_D = \sqrt{\frac{\epsilon_s k_B T}{e^2 N_d}} \quad (3.3)$$

is indicative of the width of this transition region [Blood 1992]. The assumption of abruptness between the space charge region and the neutral region is satisfied when the width of the space charge region is much larger than the Debye length. We work under the depletion approximation but Debye tail effects do play a role in characterization of deep level defects by DLTS.

3.1.3 Current-voltage characteristics

The dominant current transport mechanism in the Schottky diode is thermal emission of majority carriers over the potential barriers between the metal and the semiconductor. A quantitative analysis shows that the ideal current-voltage (IV) characteristics has the form:

$$I = I_s \left(\exp \left(\frac{eV}{k_B T} \right) - 1 \right), \quad (3.4)$$

where $V = V_F > 0$ in forward bias and $V = -V_R < 0$ in reverse bias [Sze 1985]. The saturation current I_s is given by:

$$I_s = AA^* T^2 \exp \left(\frac{-e\phi_{Bn}}{k_B T} \right), \quad (3.5)$$

where A is the diode area and A^* is the effective Richardson constant. The IV characteristics of the Schottky diodes used in this work are well described by equation (3.4). Typical experimental values of the saturation current are in the range 10^{-6} - 10^{-4} A at room temperature for diodes of area ~ 0.79 mm².

Experimental

Current-voltage measurements are carried out with a Hewlett Packard 4140B IV meter. The current is typically measured for voltages in the range -10 V to 1 V, varied in steps of ~ 0.1 V. The measurements are controlled by UMIST software.

3.1.4 Capacitance-voltage characteristics

We define the differential capacitance C associated with the space charge region as:

$$C = \frac{dQ}{dV_{tot}}, \quad (3.6)$$

where Q is the fixed charge in the space charge region. The differential capacitance is related to the width of the space charge region by the expression:

$$C = \frac{\varepsilon_s A}{W}. \quad (3.7)$$

This important result, developed under the depletion approximation, applies for an arbitrary charge distribution. Expression (3.7) is similar to the capacitance of two parallel plates of area A separated in distance W by a material with dielectric constant ϵ_s . Despite this similarity, it is important to distinguish the differential capacitance of a space charge region from the capacitance of a standard dielectric for which the charge varies linearly with the applied voltage. The zero-bias capacitances of the Schottky diodes used in this work are in the range 10-500 pF at room temperature for diodes of area $\sim 0.79 \text{ mm}^2$.

The capacitance-voltage (CV) characteristics allows determination of the spatial distribution of active dopants in the semiconductor. We write the space charge density as $\rho(x) = -eN_d^*(x)$, where N_d^* is the active donor density in the space charge region. In many cases, this quantity equals the background doping density N_d . Differentiation of equation (3.7) with respect to the reverse bias V_R relates the active donor density at the edge of the space charge region to the local slope of the CV curve:

$$N_d^*(W) = \frac{-C^3}{e\epsilon_s A^2} \left(\frac{dC}{dV_R} \right)^{-1}. \quad (3.8)$$

The corresponding space charge width is directly determined from the value of the capacitance by equation (3.7).

Experimental

Capacitance-voltage measurements are carried out with a Hewlett Packard 4192B capacitance analyzer. The capacitance is measured at different reverse bias values by superimposing an ac voltage on the dc voltage. The reverse bias is typically varied in the range $V_R = 0-10 \text{ V}$ in steps of 0.1-0.3 V. The amplitude and the frequency of the ac voltage are $\sim 10 \text{ mV}$ and $\sim 1 \text{ MHz}$, respectively. The measurements are controlled by UMIST software.

3.2 Deep-level transient spectroscopy

Deep-level transient spectroscopy (DLTS) was introduced by Lang in 1974 [Lang 1974]. Since then, the technique has had major influence in the characterization of deep level defects in semiconductors. The principle of DLTS is to perturb the occupancy of a trap by changing the value of the reverse bias applied to a Schottky diode or a pn-junction. A measurement of the diode capacitance as a function of time allows the carrier emission processes to be studied and determination of several parameters associated with the defect. In this section, we describe the principle of DLTS in more detail and discuss the techniques conventional DLTS and Laplace transform DLTS.

3.2.1 The principle of DLTS

Consider a Schottky diode formed on a n-type semiconductor. The reverse bias applied to the diode is pulsed with fixed repetition frequency between the “the reverse bias phase” at bias V_R and “the fill pulse phase” at bias $V_P < V_R$ (Figure 3.3(a)). The width of the fill pulse is denoted t_P . Figure 3.2 shows energy band diagrams of the diode at reverse bias V_R and V_P . We assume that the semiconductor has a uniform active donor density N_d and contains uniformly distributed electron traps of density N_t , which introduce energy levels located at E_t into the band gap.

In the neutral region, the quasi-Fermi level E_{Fn} is positioned above E_t and the traps are mainly filled with electrons. The trap occupancy decreases into the space charge region as $E_t(x)$ approaches E_{Fn} . We assume that, in steady-state, there are abrupt transitions between empty and filled traps at depths defined by the crossing of the quasi-Fermi level and the trap energy level. We denote this depth by x_1 for reverse bias V_R and by x_2 for reverse bias V_P (Figure 3.2). The transition length λ is given by:

$$\lambda = W_R - x_1 = W_P - x_2 = \sqrt{\frac{2\epsilon_s}{e^2 N_d} (E_{Fn} - E_t)}, \quad (3.9)$$

where W_R and W_P denote the width of the space charge region at the corresponding bias [Blood 1992]. In general, λ is not negligible compared to the space charge width.

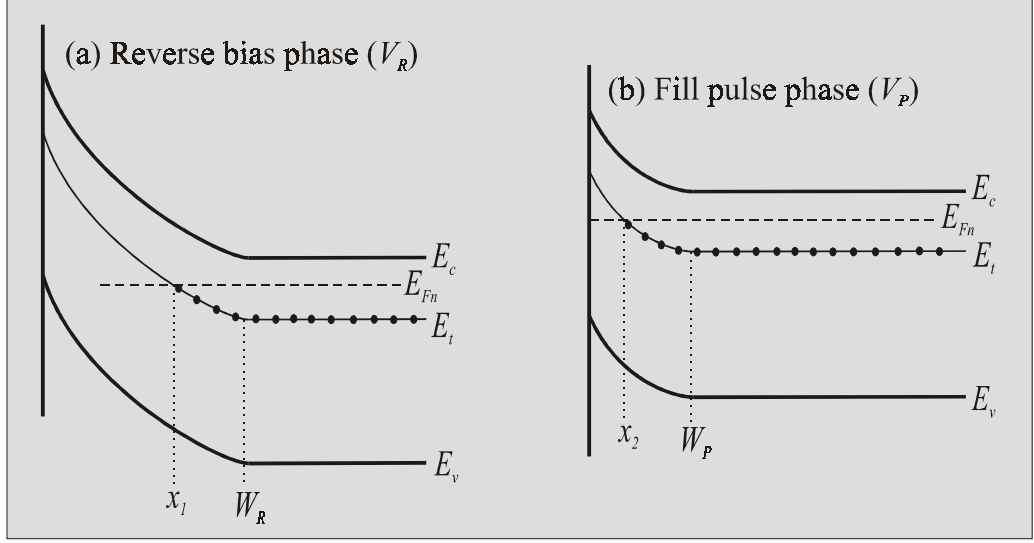


Figure 3.2: Energy band diagrams of a Schottky diode during (a) the reverse bias phase at bias V_R and (b) the fill pulse phase at bias $V_P < V_R$.

The pulsing of the reverse bias between V_R and V_P means that the occupancy of the electron traps is perturbed as the traps are successively emptied and filled in the interval $[x_2; x_1]$. The emission process during the reverse bias phase takes place in the space charge region with rate $e_n \gg c_n$, while the capture process during the fill pulse phase mainly takes place in the neutral region with rate $c_n \gg e_n$. Assuming complete emptying and filling, the trap occupancy $n_t(t)$ during capture and emission is described by equations (2.6) and (2.7), respectively.

During the emission process, shallow donors and deep centres contribute to the charge density in the space charge region by eN_d and $-en_t(x, t)$, respectively². Thus, the space charge density $\rho(x, t)$ during the emission process is given by:

$$\rho(x, t) = \begin{cases} eN_d & 0 < x < x_2 \\ e(N_d - N_t \exp(-e_n t)) & x_2 < x < x_1(t) \\ e(N_d - N_t) & x_1(t) < x < W_R(t) \end{cases} \quad (3.10)$$

²In this, we assume that the trap level is a single acceptor ($-/0$), i.e. the traps are negatively charged when filled. This assumption is not essential to the argument and a similar analysis can be carried out for other charge states.

We include a time dependence of x_1 and W_R due to the requirement of charge conservation, i.e. the increase of the space charge density during the emission process causes a gradual narrowing of the space charge region towards the steady-state value $W_R(\infty)$. By using the charge density (3.10) in equation (3.1), we obtain a differential equation for the capacitance C . Assuming $N_t \ll N_d$, the solution is given by [Blood 1992]:

$$\Delta C(t) \equiv C(t) - C(\infty) = -\Delta C_0 \exp(-e_n t) \quad N_t \ll N_d, \quad (3.11)$$

where $C(\infty)$ is the steady-state capacitance (3.7) and:

$$\frac{\Delta C_0}{C} = \frac{x_1^2 - x_2^2}{2W_R^2} \frac{N_t}{N_d}. \quad (3.12)$$

Thus, the electron emission process gives rise to a capacitance transient with time constant given by the inverse emission rate e_n^{-1} and amplitude related to the trap density N_t (Figure 3.3). The observation of this capacitance transient forms the basis of the DLTS technique. Typical trap concentrations and capacitance changes studied in this work are in the range 10^{11} - 10^{13} cm^{-3} and 0.01-1 pF, respectively, for material containing $\sim 10^{15}$ cm^{-3} shallow donors and diodes of area ~ 0.79 mm^2 .

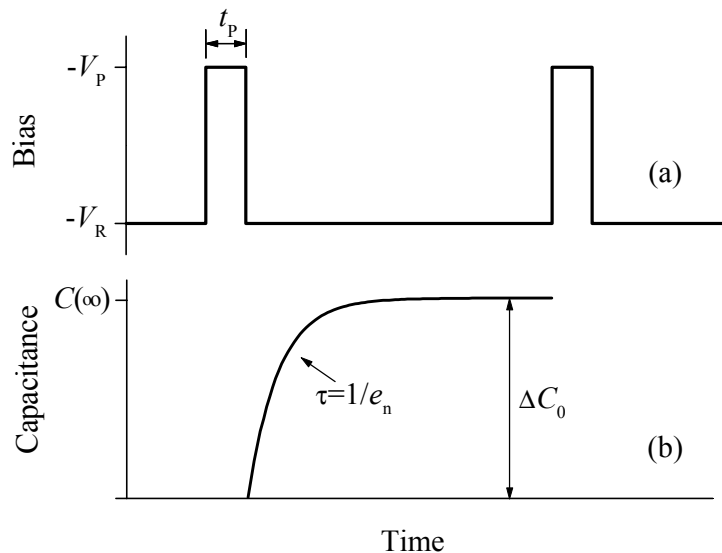


Figure 3.3: (a) Pulse train during a DLTS experiment. (b) The capacitance transient during the reverse bias phase of the measurement.

Equation (3.11) has been obtained by making a number of assumptions and approximations. Firstly, we have considered a semiconductor with only a single type of electron traps. In the general case, the semiconductor contains several types of traps of volume densities N_{ti} , which introduce energy levels located at E_{ti} into the band gap. The effective capacitance transient ΔC is interpreted as the sum of the individual contributions:

$$\Delta C(t) = \sum_i -\Delta C_{0i} \exp(-e_{ni}t) \quad N_{ti} \ll N_d, \quad (3.13)$$

where e_{ni} is the emission rate for the trap with energy level E_{ti} and ΔC_{0i} is related to N_{ti} similar to equation (3.12). Secondly, we assumed a uniform active donor density and a uniform distribution of deep level defects. In most cases, however, these conditions are not fulfilled and equation (3.12) has to be modified. Third, we assumed complete trap filling during the fill pulse phase of the measurement. Usually, this condition is easily met in a DLTS experiment but deliberate incomplete trap filling is a common approach used for direct analysis of the capture process. The cases of non-uniformity and incomplete trap filling will be considered later in this section. Fourth, equation (3.11) was derived under the important assumption $N_t \ll N_d$. When this requirement of dilute trap concentration is not met, the capacitance transient during the emission process departs from exponentiality. Finally, the theory of DLTS is developed within the limits of the depletion approximation.

3.2.2 Conventional DLTS

In conventional box car DLTS [Lang 1974], [Blood 1992], [Peaker 1999a], the capacitance is sampled at two different times t_1 and $t_2 > t_1$ during the emission process. The DLTS signal S is defined as the capacitance difference between t_2 and t_1 :

$$S \equiv C(t_2) - C(t_1) = \Delta C_0(\exp(-e_n t_1) - \exp(-e_n t_2)), \quad (3.14)$$

where equation (3.11) has been applied. During the experiment, the temperature is slowly scanned and a DLTS spectrum of signal versus temperature is recorded. The scanning of the temperature causes a change in the signal due to the thermal dependence

of the electron emission rate. For $e_n \ll (t_2 - t_1)^{-1}$ and $e_n \gg (t_2 - t_1)^{-1}$, the capacitance difference between t_2 and t_1 is small but at intermediate values $e_n \sim (t_2 - t_1)^{-1}$, this difference becomes significant. In this way, the scanning produces a peak in the DLTS spectrum. The emission rate e_n^{\max} corresponding to maximum DLTS signal is determined by differentiation of equation (3.14) with respect to e_n and setting the result equal to zero:

$$e_n^{\max} = \frac{\ln(t_2/t_1)}{t_2 - t_1}. \quad (3.15)$$

The value of e_n^{\max} , defined by the settings of t_1 and t_2 , is denoted the rate window of the measurement (typically, $e_n^{\max} \sim 1\text{-}1000 \text{ s}^{-1}$). The maximum DLTS signal $S(e_n^{\max})$ at the peak position allows estimation of the trap concentration N_t by using equations (3.12) and (3.14). Figure 3.4(a) shows an example of a conventional DLTS spectrum recorded at a rate window of 200 s^{-1} .

Conventional DLTS is a rapid technique, which efficiently detects the electrical activity of deep level defects in a semiconductor diode. The sensitivity is remarkable and allows detection of electrically active defect densities down to $10^{10}\text{-}10^{11} \text{ cm}^{-3}$, several orders of magnitude better than most other techniques used for defect characterization in semiconductors. One major problem, however, is the lack of resolution which makes it extremely difficult to separate the emissions from closely spaced energy levels in the band gap. The spectrum shown in Figure 3.4(a) clearly illustrates this problem. Several schemes have been proposed in order to improve the resolution of Lang's original box car technique [Peaker 1999a] but broad, featureless peaks remain a general problem of conventional DLTS.

Experimental

In this work, conventional DLTS measurements are carried out in a vacuum chamber ($\lesssim 0.05 \text{ mbar}$) in which the sample is cooled by the contact to the cold finger of a closed-cycled helium cryocooler. The temperature is controlled by a Lakeshore 340 temperature controller. A temperature scan rate of 0.05 K/s is used for all measurements. The bias is applied by a UMIST card and the capacitance is monitored with a

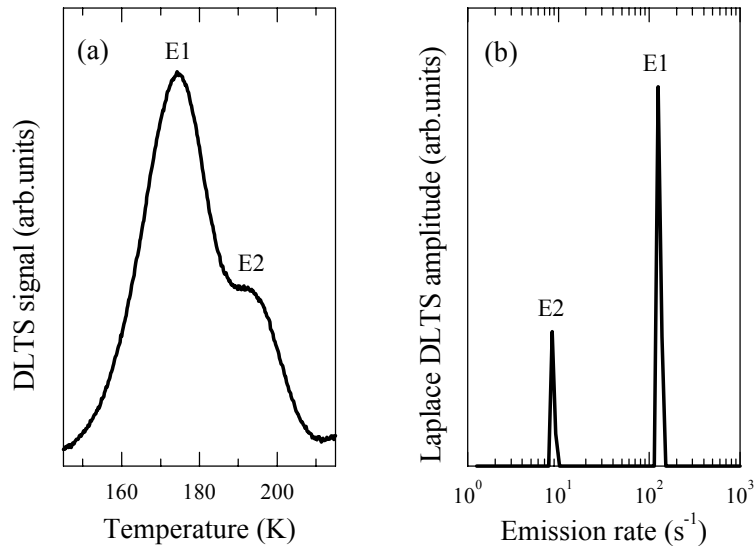


Figure 3.4: (a) Conventional DLTS spectrum recorded at a rate window of 200 s^{-1} . (b) Laplace DLTS spectrum recorded at temperature 170 K in the same sample and under similar experimental conditions. The spectra each contain two peaks related to the same electron traps labelled E1 and E2.

Boonton 72-4B capacitance meter or a UMIST capacitance meter. The measurements are controlled by the software “TrapView”.

3.2.3 Laplace transform DLTS

Laplace transform DLTS (Laplace DLTS) [Dobaczewski 1994] is an isothermal technique in which the capacitance transient is averaged at a fixed temperature. In order to account for non-exponentiality, the recorded transient is described as a continuous spectrum of emission rates rather than the discrete sum given by equation (3.13). That is:

$$f(t) = \int_0^\infty F(s) \exp(-st) ds, \quad (3.16)$$

where $f(t)$ is the measured transient and $F(s)$ is the spectral density function. The basic idea is to determine $F(s)$ from the measured transient $f(t)$ by using an appropriate mathematical algorithm [Provencher 1982], [Dobaczewski 1994], [Istratov 1999]. In principle, this problem is solved by taking the inverse Laplace transform of the averaged transient $f(t)$, hence the name Laplace transform DLTS. This, however, is far

from a trivial problem [Istratov 1999]. For an analytical, multiexponential function $f(t)$, equation (3.16) has a unique solution $F(s)$ but in the case of an experimentally obtained transient $f(t)$ with noise and an unknown base line, the number of solutions can be infinite and the solutions can differ strongly from each other.

In order to deal with discrete experimental data, we consider the Laplace equation (3.16) in the matrix form:

$$\mathbf{f} = K\mathbf{F}, \quad (3.17)$$

where $\mathbf{f} = (f_1, f_2, \dots, f_{N_f})$ is a vector of N_f data points, $\mathbf{F} = (F_1, F_2, \dots, F_{N_F})$ is a vector of N_F points in the spectral density function and K is a $N_f \times N_F$ matrix, which represents the Laplace integral operator. The mathematical algorithm used to obtain the solution \mathbf{F} is known as the Tikhonov regularization method [Provencher 1982], [Istratov 1999]. In this method, the solution is chosen as the best compromise between two requirements: (i) the norm-square $\|K\mathbf{F} - \mathbf{f}\|^2$ has to be minimal in order to fulfill equation (3.17) and (ii) the solution \mathbf{F} has to be as “simple” as possible, i.e. \mathbf{F} has to be smooth and contain a minimum number of peaks [Provencher 1982]. These requirements mean that the optimal solution \mathbf{F} minimizes the value:

$$\|K\mathbf{F} - \mathbf{f}\|^2 + \alpha^2 \|\Omega\mathbf{F}\|^2, \quad (3.18)$$

where Ω is the regularization matrix and α is the regularization parameter [Istratov 1999]. The regularization matrix acts on the solution \mathbf{F} by calculation of the second derivative, i.e.:

$$\|\Omega\mathbf{F}\|^2 = \int_{s_{\min}}^{s_{\max}} \left(\frac{d^2\mathbf{F}}{ds^2} \right)^2 ds. \quad (3.19)$$

The strength of the regularization term $\alpha^2 \|\Omega\mathbf{F}\|^2$ is determined by the value of the regularization parameter α . If α is too small, there is a risk of non-smooth, non-physical solutions, while, if α is too large, the original equation (3.17) is not adequately fulfilled. The specific mathematical algorithms used for the regularization process are not considered in the thesis.

Laplace DLTS utilizes three mathematical routines that are all based on the Tikhonov regularization method. These are CONTIN [Provencher 1982], FTIKREG [Weese 1992]

and FLOG. The solution $\mathbf{F}(s)$, denoted the Laplace DLTS spectrum, is either a spectrum of a broad structure for a transient with a continuum of time constants or a spectrum of narrow delta-like peaks for a mono- or multiexponential transient. If the transient is described by the multiexponential expression (3.13), the individual peaks are centered around the emission rates e_{ni} with the intensities ΔC_{0i} obtained as the areas under each sharp peak. An example of a Laplace DLTS spectrum recorded at 170 K is shown in Figure 3.4(b)³.

The main advantage of Laplace DLTS in comparison to conventional DLTS is the substantial increase in energy resolution. The noise on the measured transient sets a fundamental limit on the resolution obtainable in exponential analysis [Istratov 1999]. In Laplace DLTS, we often achieve a resolution close to this limit. The actual resolution depends on several experimental factors, including the temperature stability, the signal to noise ratio and the specific computational routine used for the regularization process. As a rule of thumb, the components are reliably separated for emission rate ratios larger than a factor of 2-3. The difference in resolution between conventional DLTS and Laplace DLTS is clearly demonstrated in Figure 3.4, which compares measurements of the same electron traps (labelled E1 and E2) by the two techniques. The conventional DLTS spectrum displays E2 as a shoulder to E1, while the emission components are clearly separated by the Laplace DLTS technique. The substantial increase in resolution allows studies of more closely spaced deep energy levels in the band gap. Examples of Laplace DLTS studies are the separation of the emissions from the substitutional gold acceptor and the gold-hydrogen acceptor [Deixler 1998], the separation of the emissions from the acceptor levels of platinum surrounded by different numbers of germanium atoms in a SiGe alloy [Dobaczewski 1999] and uniaxial stress DLTS studies [Bonde 1999a], [Andersen 2002].

³The Laplace DLTS spectra $\mathbf{F}(s)$ are presented on a logarithmic s -scale. Thus, because the peak intensities are related to the area under the curve, the true values and the visual impressions of the peak intensities do not agree, i.e. slower emissions appear to be relatively more dominant than faster emissions. For this reason, all Laplace spectra in this work are presented with $s \times \mathbf{F}(s)$ on the vertical axis.

Experimental

In this work, zero-stress Laplace DLTS measurements are carried out in a vacuum chamber cooled by a closed-cycled helium cryocooler (the same cryostat used for conventional DLTS measurements). Uniaxial stress Laplace DLTS measurements are carried out either in a cryostat cooled by a nitrogen gas or a cryostat cooled by a closed-cycled helium cryocooler. For stress measurements, the sample is mounted between two cylinders made of hardened steel and a force is transmitted to the sample through a carbon fiber rod attached to a spring. The temperature is controlled by a Lakeshore 330 or Lakeshore 340 temperature controller. These experimental set-ups ensure high temperature stability to the order of a few mK. The bias is applied by a UMIST card and the capacitance is monitored with a Boonton 72-4B capacitance meter or a UMIST capacitance meter. The measurements are controlled by the software “Laplace DLTS”. The duration of the recorded transient is controlled by setting the sampling rate and the number of samples, chosen on the basis of the time constant of the transient at the given temperature. The noise level is decreased by averaging over many transients, typically 10^2 - 10^3 in order to achieve a signal-to-noise ratio of $\sim 10^3$. Finally, the averaged transient is computed and the Laplace DLTS spectrum is obtained.

3.2.4 DLTS-related techniques

Thermal activation of the emission process

Corresponding values of temperature and emission rate can be obtained from both conventional DLTS and Laplace DLTS experiments, in the former case by measuring the peak position at a number of rate windows, in the latter by measuring the carrier emission rate at a number of temperatures. Thus, the activation energy E_n^a and the apparent electron capture cross section σ_n^a can be determined from an Arrhenius plot of the emission process.

Capture measurements

So far we have assumed that the pulse width during the DLTS measurement is long enough to fill all traps in the region $[x_2; x_1]$. However, appropriate reduction of the pulse width causes incomplete trap filling and allows direct analysis of the capture process. The capture measurements are carried out by varying the width t_P of the fill pulse and measuring the amplitude $\Delta C_0(t_P)$ of the capacitance transient under the same bias conditions. In the ideal case, the capture kinetics are described by equation (2.6), i.e.:

$$\frac{\Delta C_0^{\max} - \Delta C_0(t_P)}{\Delta C_0^{\max}} = \exp(-c_n t_P), \quad (3.20)$$

where ΔC_0^{\max} is the maximum amplitude corresponding to complete trap filling. Thus, the capture rate c_n can be determined from a plot of the relative signal reduction $\frac{\Delta C_0^{\max} - \Delta C_0(t_P)}{\Delta C_0^{\max}}$ versus fill pulse width t_P . Subsequently, the electron capture cross section σ_n is obtained from equation (2.8). This “filling pulse method” determines the true capture cross section at the measurement temperature and not the apparent capture cross section obtained from the Arrhenius plot of the emission process. The temperature dependence of the capture process is studied by repeating the procedure at a number of temperatures.

Though the above approach gives a good approximation of the capture characteristics of a given trap, there are possible pitfalls. The main factor is the fact that the capture process does not entirely take place in the neutral region of the semiconductor but also in the Debye tail near the edge of the space charge region (Figure 3.2). In the Debye-tail, the free carrier density varies strongly and there exist a distribution of capture rates. Consequently, equation (3.20) is not fulfilled. Usually, the capture kinetics can be described by the sum of a fast, purely exponential part corresponding to capture in the neutral region and a slow, non-exponential part corresponding to capture in the Debye tail [Pons 1984]. A detailed description of the Debye tail effect in relation to capture studies has been given by Pons [Pons 1984].

Depth profiling

In our description of DLTS, we have assumed a uniform distribution of deep level defects in the semiconductor. Obviously, this is usually not the case for defects formed by ion implantation or as a result of surface etching. The problem of obtaining the profile of a deep level defect by DLTS is far from trivial. The basic idea is to change the measurement region $[x_2; x_1]$ by varying the values of the reverse bias V_R or the fill pulse V_P . Either the reverse bias is fixed and a measurement series is carried out at a number of fill pulses, or the fill pulse is fixed and a measurement series is carried out at different values of the reverse bias. A careful analysis of the experimental data has to take into account the exact profile of active dopants (often non-uniform) and the effect of the Debye tail. An alternative approach is to apply the technique of Double DLTS in which two fill pulses V_P and V'_P are applied in the pulse train and the difference between the corresponding DLTS signals is monitored. This technique minimizes Debye tail effects and localizes the signal to a narrow region. However, trap profiling by Double DLTS also requires great care [Stievenard 1986]. Trap distributions given in this work are obtained by using UMIST software, which takes into account the Debye tail effect and non-uniform dopant distributions.

Electric field measurements

As described in Chapter 2, the dependence of the carrier emission rate on the electric field strength can indicate the charge state of a deep energy level. The field effect is examined by measuring the emission rate for different settings of the reverse bias V_R and/or the fill pulse V_P . An alternative approach is to apply the technique of Double DLTS in order to minimize the spreading of the field in the measurement region. The average electric field strength in the measurement region is estimated from the capacitance-voltage characteristic of the device.

Uniaxial stress measurements

The influence of uniaxial stress on a defect centre was described in detail in Chapter 2. We can divide the uniaxial stress DLTS measurements carried out in this work into four types of experiments. The first two assume a random distribution of defects in non-equivalent orientations, while the latter two are stress-induced alignment experiments:

- The true (or apparent) symmetry of a defect centre is obtained from the intensity ratio of the split DLTS lines under uniaxial stress applied along the three major crystallographic directions, $\langle 100 \rangle$, $\langle 110 \rangle$ and $\langle 111 \rangle$.
- The influence of stress on the ionization process is studied by measuring the carrier emission rates of the split peaks at a number of stresses. The splitting of the energy level with stress is governed by the difference in the piezospectroscopic tensors of the two charge states involved in the transition.
- The total energy difference between two non-equivalent orientations of a defect in a given charge state is obtained from their steady-state occupancy ratio under stress. In most cases, the steady-state condition is reached at higher temperatures, followed by a quick cool-down to the measurement temperature. The energy difference is governed by the piezospectroscopic tensor for the given charge state.
- The reorientation kinetics of a defect are studied by measuring the gradual alignment or mis-alignment of the defect under a given stress. The energy barrier for the reorientation process and the stress-dependence of the barrier can be obtained from the time constant of the alignment process by using Boltzmann statistics.

3.3 Secondary ion mass spectroscopy

Secondary ion mass spectroscopy (SIMS) [Schroder 1998] is one of the most effective techniques to determine the elemental composition of the surface region of a solid. During a SIMS measurement, a primary beam of 0.5-20 keV ions (Cs^+ , O^- , O_2^+ , Ar^+)

is bombarding the sample under study. On their way through the solid, the primary ions collide with the different species in the sample and come to rest deeper in the bulk. The energy transfer from the primary ions to these species causes a sputtering of material close to the sample surface. These secondary ions are analyzed in a mass spectrometer. In a dynamic SIMS measurement, the number of ion counts for a given element is recorded as a function of sputtering time. The number of ion counts is converted into element concentration by comparison to a sample with known composition and the sputtering time is converted into depth by examination of the sputter crater after the measurement. In this way, the depth distribution of the given element is obtained. SIMS is capable of detecting any element in the periodic table with a detection limit of typically 10^{15} cm^{-3} . Unfortunately, the detectivity for hydrogen is much smaller due to contamination of the measurement chamber by hydrogen deposition from the stainless steel.

Experimental

SIMS measurements used in this work were carried out at CSMA in Manchester by Dr. Alan Brown or at IFPAN in Warsaw by Prof. Adam Barcz and Dr. Marcel Zielinski. CAMECA equipment was used in both places.

3.4 Electron paramagnetic resonance

Electron paramagnetic resonance (EPR) [Watkins 1961] is probably the most powerful experimental technique to obtain structural information about paramagnetic defects in semiconductors. The technique utilizes the Zeeman-splitting of electronic energy states in the presence of an external magnetic field.

In an EPR experiment, the sample is located in a cavity and illuminated with microwave radiation of frequency ν . The magnitude of a magnetic field \mathbf{B} applied along one of the major crystallographic directions is slowly scanned. The interactions

of the magnetic field with the defect are described by the Hamiltonian:

$$\mathbf{H} = -\boldsymbol{\mu} \cdot \mathbf{B}, \quad (3.21)$$

where $\boldsymbol{\mu}$ is the total magnetic dipole moment given by the sum of the contributions from the orbital angular momentum \mathbf{L} and the electronic spin \mathbf{S} . For most paramagnetic defect in silicon, the contribution from the spin is the dominant part. In this case, the dipole moment is written in the form:

$$\boldsymbol{\mu} = -\mu_B \mathbf{g} \cdot \mathbf{S}, \quad (3.22)$$

where μ_B is the Bohr magneton and \mathbf{g} is a symmetric tensor. The departure of \mathbf{g} from the free electron value is caused by the spin-orbit interaction, which depends on the orientation of the magnetic field relative to the defect. The energy difference between the Zeeman-split states is given by:

$$\Delta E = g\mu_B B, \quad (3.23)$$

where the value g is governed by the \mathbf{g} tensor. During the experiment, a dipole transition occurs when the splitting $g\mu_B B$ equals the energy quantum $h\nu$. The first derivative of the absorption signal is monitored as a function of magnetic field magnitude and a transition is seen as a sharp line in the spectrum. For a given direction of \mathbf{B} , several resonances related to the same defect are generally observed as the Zeeman-splitting varies for different defect orientations relative to the field. The symmetry class of the defect is obtained from the numbers and the relative intensities of the lines for experiments with \mathbf{B} applied along the major crystallographic directions. In many cases, one of the nuclei in the defect has a non-vanishing nuclear spin, which can also interact with the electronic spin. This hyperfine interaction modifies the Hamiltonian and leads to a splitting of the EPR lines, hence providing additional information. The technique has also been used in combination with uniaxial stress to obtain the defect piezospectroscopic tensor from alignment experiments.

3.5 Infrared absorption spectroscopy

The theory of host atom vibrations in a solid is well known. The phonon dispersion curve depends on the masses of the host atoms and the effective spring constants describing their interactions. A light impurity in the crystal normally oscillates with frequencies much higher than the phonon frequencies. These oscillations only interact weakly with their nearest neighbor host atoms and, consequently, they are localized in the lattice. The modes of the oscillations are denoted local vibrational modes (LVM's). The principle of infrared absorption spectroscopy [Schroder 1998] is to excite the impurity from one vibrational state to another by absorption of infrared light of energy $\hbar\omega$. During the experiment, the sample is exposed to a beam of infrared light. The transition between vibrational states is seen as a sharp line at frequency ω in the absorption spectrum of the sample. In Fourier transform infrared spectroscopy (FTIR), the analysis is carried out by using a Michelson interferometer. The interferograms with and without the sample inserted in the instrument are recorded and subsequently converted into single-beam spectra by a Fourier transform. Finally, a spectrum of absorbance versus frequency is produced, where the absorbance is defined by:

$$A = \ln \left(\frac{I_B}{I_S} \right) \quad (3.24)$$

and I_B and I_S are the single-beam spectra obtained without and with the sample inserted, respectively. A LVM is seen as a sharp line in the spectrum at the corresponding frequency. The chemical nature of a defect can sometimes be determined by isotopic substitutions, which shift the value of the vibrational frequency. The technique is also used in combination with uniaxial stress for symmetry determination and defect alignment experiments.

3.6 Theoretical modeling of defects

Theoretical modeling of defects in semiconductors [Estreicher 1995], [Jones 2000] has played an important role during the past decade. The recent progress of theoretical

investigations is related to the great increase in computer power, which make the calculations much more reliable. Two approaches are used for the modeling. The cluster method models a defect located in a small cluster of host atoms, while the supercell method models a periodic system of atoms. A major problem with the cluster method is the interference of the surface of the cluster with the inner part of the cluster, where the defect is located. The surface effects are minimized by using larger clusters or by saturating the surface dangling bonds with hydrogen atoms. The problem of surface effects does not exist in the supercell method but this approach gives rise to interactions between defects located in neighboring cells.

A given defect structure is examined by solving the many-body Schrödinger equation for the system. Obviously, this is an extremely complicated task, which involves a number of assumptions and approximations. The solution of the Schrödinger equation gives relative energies of possible stable and metastable configurations, while other structures are excluded. Traditionally, the calculations were carried out by using fits to empirical data for well-described defect systems. The current focus, however, is on using *ab initio* methods, which involve no such use of empirical data. Theoretical calculations also produce a number of experimental observables associated with the defects, including dissociation energies, local vibrational modes, band gap energy levels and piezospectroscopic tensor components. Thus, direct comparison between theoretical and experimental data can form an important tool for defect identification.

Chapter 4

Hydrogen incorporation by remote plasma treatment

Several techniques can be used for hydrogenation of semiconductor material. The methods include wet chemical etching, proton implantation, in-diffusion from a hydrogen gas at high temperatures, boiling in water and exposure to a hydrogen plasma. In this chapter, we consider the latter of these techniques. After its installation in the spring of 2000, the plasma system at UMIST has been used for numerous experimental studies, some of which are presented later in the thesis. The aim of this chapter is to quantify the amount and the form of hydrogen incorporated into silicon by exposure to the plasma under different experimental conditions.

4.1 Background

The spatial profile of hydrogen in plasma treated silicon can be determined by SIMS measurements. For this purpose, it is common to use the deuterium isotope with identical electronic properties to hydrogen and much higher detectivity as a result of its low natural abundance. Deuterium depth profiles in silicon obtained after plasma treatments below 300 °C have been presented in [Johnson 1985a], [Johnson 1985b], [Johnson 1986], [Johnson 1987], [Pearton 1992]. Some general features can be extracted

from the profiles. Within a depth of $\sim 0.1 \mu\text{m}$ from the sample surface, the deuterium concentration is very high and decreases steeply from $\sim 10^{20} \text{ cm}^{-3}$ to $\sim 10^{18} \text{ cm}^{-3}$. Deeper in the samples, the concentration decreases more gently with depth from $\sim 10^{18} \text{ cm}^{-3}$ towards the detection limit of $\sim 10^{15} \text{ cm}^{-3}$. The profile in this region depends critically on the type of silicon material and the plasma conditions. The deuterium penetration depth is typically in the range 1-10 μm .

The highly hydrogenated sub-surface region has been attributed to the formation hydrogen-related platelets [Johnson 1987]. These are ordered planar defects, which each can extend several tens of nanometers in the lattice. The platelet formation requires a minimum hydrogen concentration of $\sim 10^{17} \text{ cm}^{-3}$ and their generation is controlled by the position of the Fermi level [Nickel 2000]. The dominant platelets are those lying in (111) crystallographic planes but their exact microscopic structure has remained unknown for years. Recently, it was shown that two different structures of (111) oriented hydrogen-related platelets can co-exist in concentrations depending on the plasma conditions [Lavrov 2001]. Further, the specific structure of the two types of platelets was proposed.

Another important defect formed in plasma treated silicon is the hydrogen molecule. Theoreticians have predicted the existence of interstitial hydrogen molecules in silicon for years [Estreicher 1994], [Van de Walle 1994], [Estreicher 1995], [Hourahine 1998] but until recently there was little experimental evidence for the existence of the defect. However, recent infrared absorption measurements [Pritchard 1997], [Pritchard 1998], [Pritchard 1999] have identified isolated interstitial hydrogen molecules and hydrogen molecules located close to interstitial oxygen atoms in silicon hydrogenated at 1300 °C by a flowing H₂-gas. After hydrogenation, the O_i-H₂ complexes are dominant but these centres gradually dissociate and transform into isolated molecules during annealing in the temperature range 35-130 °C. In the case of plasma treated silicon, molecular hydrogen has been identified by means of Raman spectroscopy. Murakami et al. observed a Raman line at 4158 cm⁻¹ after hydrogenation in the temperature range 180-500 °C, which was ascribed to isolated hydrogen molecules located at interstitial

sites [Murakami 1996], [Fukata 1997]. This claim was later disputed by Leitch et al. [Leitch 1998a] and the present view is that the line at 4158 cm^{-1} is due to hydrogen molecules trapped within voids formed by the plasma-induced platelets. Subsequently, a weaker Raman line at 3601 cm^{-1} observed after plasma treatment at $150\text{ }^\circ\text{C}$ has been associated with isolated hydrogen molecules located at interstitial sites [Leitch 1998b]. Both forms of molecules have been observed in n-type as well as p-type silicon [Kitajima 1999]. The formation of hydrogen molecules in the two forms depends critically on the temperature during plasma treatment [Fukata 1997], [Leitch 1998b], [Kitajima 1999].

The interactions of hydrogen with shallow dopants is one of the most well understood topics involving hydrogen in silicon. Theoreticians agree that the lowest energy configurations of the hydrogen-dopant complexes in silicon have the hydrogen atom positioned at an anti-bonding site of a Si-donor bond and at a bond-center site of a Si-acceptor bond [Van de Walle 1994], [Estreicher 1995], [Zhou 1995]. These centres are electrically inactive and, consequently, their formation has a significant effect on electrical measurements. Hydrogen-acceptor complexes are in general more stable than hydrogen-donor complexes. The binding energies for the hydrogen-boron pair and the hydrogen-phosphorous pair have been estimated as 0.87 eV and $0.35\text{-}0.65\text{ eV}$, respectively [Johnson 1991]. The passivation of shallow dopants after remote hydrogen plasma treatment has been reported by Johnson et al. for both boron doped p-type silicon [Johnson 1985a] and phosphorous doped n-type silicon [Johnson 1986]. For comparable experimental conditions, donor passivation was found to be less pronounced than acceptor passivation.

The formation of deep level defects upon exposure of n-type silicon to a remote hydrogen plasma has not been studied extensively. Johnson et al. observed two acceptor levels at $E_c - 0.06\text{ eV}$ and $E_c - 0.51\text{ eV}$ in concentrations $\lesssim 10^{13}\text{ cm}^{-3}$ after plasma treatment of n-type silicon at $150\text{ }^\circ\text{C}$ [Johnson 1987]. The complexes were unstable at room temperature and annealed with an activation energy of $\sim 0.3\text{ eV}$. It was concluded that both defects are related to hydrogen but no specific identification

was given. Remarkably, this seems to be the only documented investigation of deep level defects formed by exposure of n-type silicon to a remote hydrogen plasma. More detailed work has been carried out for p-type silicon but this will not be considered here.

4.2 Experimental details

4.2.1 Sample preparation

Five sets of n-type silicon samples have been used. Descriptions of the various samples are given in Table 4.1. The samples were hydrogenated/deuterated by remote plasma treatments. The plasma system consisted of a quartz tube through which a molecular hydrogen/deuterium gas was pumped. The gas pressure and the flow rate during treatments were maintained at ~ 1.0 mbar and ~ 50 cm³/min, respectively. The hydrogen/deuterium plasma was excited by a 13.56 MHz generator connected to a copper coil encircling the tube. The samples were positioned in the quartz tube downstream from the plasma, approximately 15 cm away from the plasma itself. This is thought to minimize damage to the sample due to ion bombardment. Plasma powers in the range 10-70 W, treatment temperatures in the range 30-400 °C and treatment times in the range 10-240 minutes have been used. Ignition of the plasma increased the sample temperature by 5-10 °C. Hence, room temperature treatments correspond to a sample

| Material | Plasma treatment |
|---|---------------------------------|
| epi n-n ⁺ Si (P), 0.5 Ω -cm | H+D, 30 °C, 10-70 W, 10-240 min |
| Cz n-Si (P), 0.2 Ω -cm | D, 30 °C, 30 W, 30-180 min |
| FZ n-Si (P), 20 Ω -cm | H, 120 °C, 30 W, 60 min |
| FZ n-Si (P), 38-50 Ω -cm | D, 30-400 °C, 30 W, 60 min |
| FZ n-Si (P), 1.0 Ω -cm | D, 30 °C, 30 W, 30-180 min |

Table 4.1: Details of materials and plasma treatments of samples used in this study.

temperature of ~ 30 °C. Details of conditions during plasma treatments of specific samples are given in Table 4.1. Schottky diodes and Ohmic contacts were formed for electrical measurements by evaporation of gold and aluminum, respectively.

4.2.2 SIMS measurements

SIMS measurements were carried out at CSMA in Manchester by Dr. Alan Brown or at IFPAN in Warsaw by Prof. Adam Barcz and Dr. Marcel Zielinski. CAMECA equipment was used in both places. Measurements at CSMA were carried out into a depth of ~ 1 μm from the surface with a relatively high resolution of ~ 5 nm. Measurement at IFPAN were carried out into a depth of ~ 10 μm but with a much lower resolution of ~ 100 nm.

4.3 Results and discussion

4.3.1 Room temperature plasma treatments

Figure 4.1 shows SIMS deuterium profiles obtained in 0.2 $\Omega\text{-cm}$ Czochralski (Cz) n-Si and 1.0 $\Omega\text{-cm}$ float-zone (FZ) n-Si after plasma treatment at room temperature for 30 and 180 minutes. The SIMS measurements were carried out at CSMA with a detection limit of $\sim 1 \times 10^{15}$ cm^{-3} . Within a depth of ~ 0.1 μm from the sample surface, the deuterium concentration is very large and decreases steeply from $\sim 10^{21}$ cm^{-3} to $\sim 10^{17}$ cm^{-3} . The surface concentration is by approximately one order of magnitude larger in the FZ material than in the Cz material. The surface concentration observed in the 0.2 $\Omega\text{-cm}$ Cz n-Si sample is slightly larger than the concentration reported by Johnson et al. after deuteration of comparable material at 150 °C [Johnson 1986]. Thus, our results suggest an equally strong formation of deuterium-related platelets even at room temperature, where the in-diffusion of deuterium is much slower. A possible explanation lies in the enhancement of the platelet generation, when the Fermi level moves closer to the conduction band [Nickel 2000]. Deeper in the samples, the deuterium concentration decreases more gently with depth and eventually reaches a practically constant level.

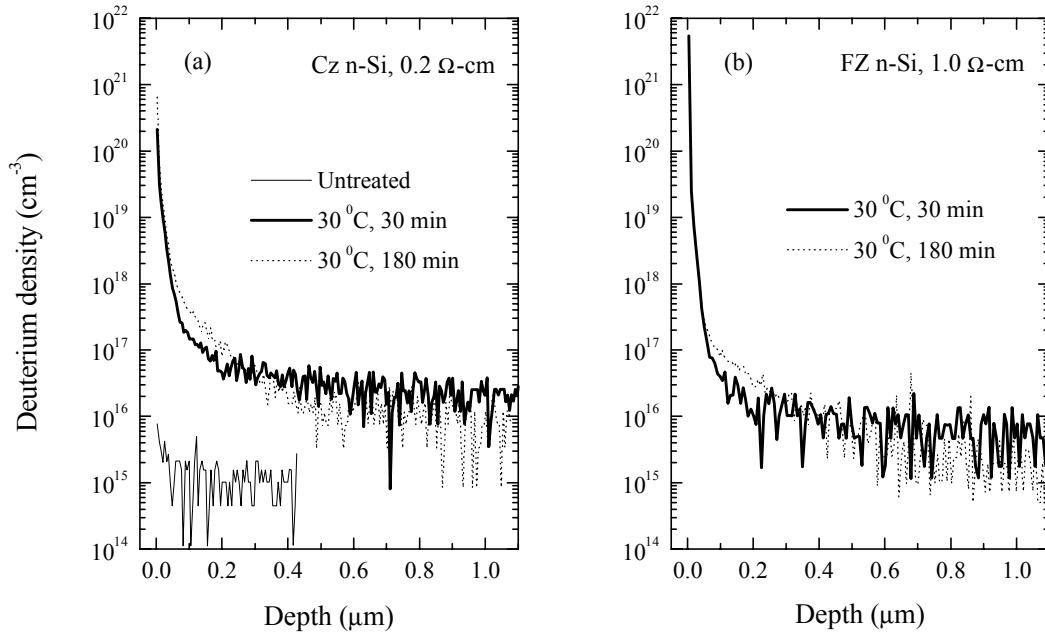


Figure 4.1: Deuterium depth profiles measured in (a) 0.2 Ω -cm Cz n-Si deuterated for 30 and 180 minutes at room temperature and (b) 1.0 Ω -cm FZ n-Si deuterated for 30 and 180 minutes at room temperature. The measurements have been carried out at CSMA.

For both materials, the effect of longer treatment time is to increase the deuterium concentration at depths 0.1-0.3 μm , indicating a slow generation of a given complex in this range. The constant level of deuterium, reached beyond a depth of $\sim 0.3 \mu\text{m}$, is approximately $1\text{-}3 \times 10^{16} \text{ cm}^{-3}$ for 0.2 Ω -cm Cz n-Si and approximately $2\text{-}6 \times 10^{15} \text{ cm}^{-3}$ for 1.0 Ω -cm FZ n-Si. In both cases, the value is comparable to the background doping level of the material.

Figure 4.2 shows typical free carrier profiles for untreated and hydrogenated epitaxial 0.5 Ω -cm n-n⁺-Si. The data demonstrate that the hydrogenation causes a significant decrease in the number of free carriers. The carrier loss depends on material type, treatment conditions and sample depth but typically 50-80% of carriers are compensated for plasma treatments carried out before Schottky diode formation and 2-20% of carriers are compensated for plasma treatments carried out after Schottky diode formation. Evidently, not much of the atomic hydrogen penetrates the metallic layer. Note, that the compensation extends deeper than 1 μm into the sample. Complete passivation

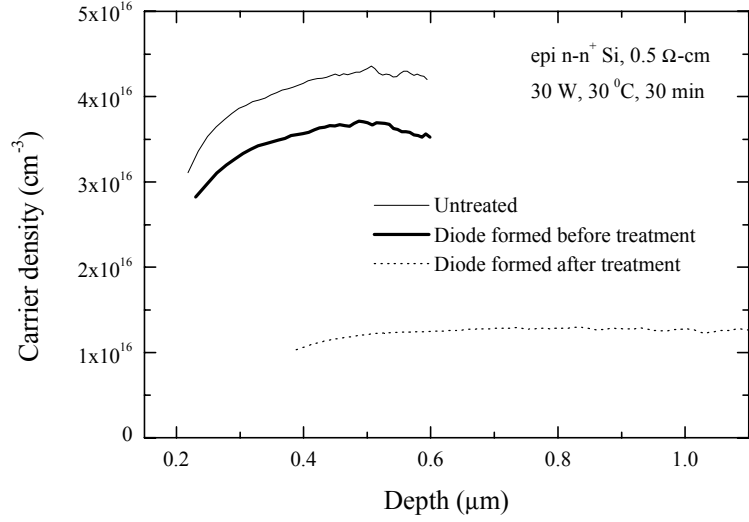


Figure 4.2: Free carrier profiles for untreated and hydrogenated epitaxial 0.5 Ω -cm n-n⁺ silicon. The plasma treatments were carried out for 30 minutes at room temperature at a power of 30 W.

of carriers was never observed, at least 20% of the phosphorous always remained electrically active. The level of compensation was found to systematically increase for increasing powers in the range 10-70 W, while there was practically no effect of treatment times in the range 10-240 minutes. No systematic differences were observed between hydrogenated and deuterated samples. A similar level of compensation to the data presented in Figure 4.2 was observed in 0.2 Ω -cm Cz n-Si.

The correlation between the total deuterium concentration and the loss of free carriers indicates that the deuterium mainly exists in the form of deuterium-dopant complexes beyond $\sim 0.3 \mu\text{m}$ after room temperature plasma treatment. A somewhat similar conclusion has been reached for intermediate to highly doped p-type silicon deuterated at 150 $^{\circ}\text{C}$ [Johnson 1985a], [Johnson 1987]. A much less pronounced passivation, however, was seen for n-type silicon treated at 150 $^{\circ}\text{C}$, where the total deuterium concentration dropped significantly below the doping level of the material for depths beyond $\sim 0.3 \mu\text{m}$ [Johnson 1986]. We interpret that the stronger passivation observed in the present work is an effect of treatment temperature. A significant dissociation of the deuterium-donor complexes will take place at 150 $^{\circ}\text{C}$ and during the cool-down of the sample, while the complexes are stable at room temperature. Thus, the present

results demonstrate the possibility of strong passivation of shallow donors into depths above $1 \mu\text{m}$ by room temperature remote plasma treatment.

4.3.2 Effect of treatment temperature

Figure 4.3 shows SIMS deuterium profiles obtained in 38-50 $\Omega\text{-cm}$ FZ n-Si deuterated for 60 minutes at temperatures in the range 30-400 $^{\circ}\text{C}$. The SIMS measurements were carried out at IFPAN with a detection limit of $\sim 1 \times 10^{15} \text{ cm}^{-3}$. The lowly doped FZ material was chosen to minimize the effect of impurities. After deuteration, the sample was cooled from the treatment temperature to room temperature in a time space of approximately 5 minutes, with the plasma and the deuterium flow turned off. The data in Figure 4.3 demonstrate a strong effect of treatment temperature. Initially, the deuterium incorporation increases substantially with temperature due to enhanced diffusion into the sample. The profile extends to $\sim 1 \mu\text{m}$ at 30 $^{\circ}\text{C}$, $\sim 5 \mu\text{m}$ at 100 $^{\circ}\text{C}$ and $\sim 10 \mu\text{m}$ at 200 $^{\circ}\text{C}$. For treatment temperature above 200 $^{\circ}\text{C}$, however, the deuterium concentration falls dramatically. The profile extends to $\sim 2 \mu\text{m}$ at 300 $^{\circ}\text{C}$ and practically no deuterium is detected after treatment at 400 $^{\circ}\text{C}$.

The data are consistent with in-diffusion of deuterium in atomic form and subsequent self-interaction to form interstitial molecules as the dominant deuterium-related species in the bulk of the material. The experimental conditions mean the Fermi level is positioned below $\sim E_c - 0.3 \text{ eV}$ during the treatments, i.e. the atomic deuterium introduced from the plasma exists in the positive charge state [Herring 2001]. Diffusion of positively charged hydrogen/deuterium in silicon was originally described by van Wieringen and Warmoltz [van Wieringen 1956] and has more recently been studied by Gorelkinskii and Nevinnyi [Gorelkinskii 1996] and by Herring et al. [Herring 2001]. The three studies are in good agreement and together cover the temperature range 125-1480 K. Using the data obtained by Herring et al., we estimate the diffusion length of positively charged atomic deuterium in silicon as $\sim 2 \mu\text{m}$ at 30 $^{\circ}\text{C}$, $\sim 9 \mu\text{m}$ at 100 $^{\circ}\text{C}$ and $\sim 47 \mu\text{m}$ at 200 $^{\circ}\text{C}$ for 60 minutes diffusion. These values are significantly larger than the penetration depths observed experimentally in the present work. This result is ex-

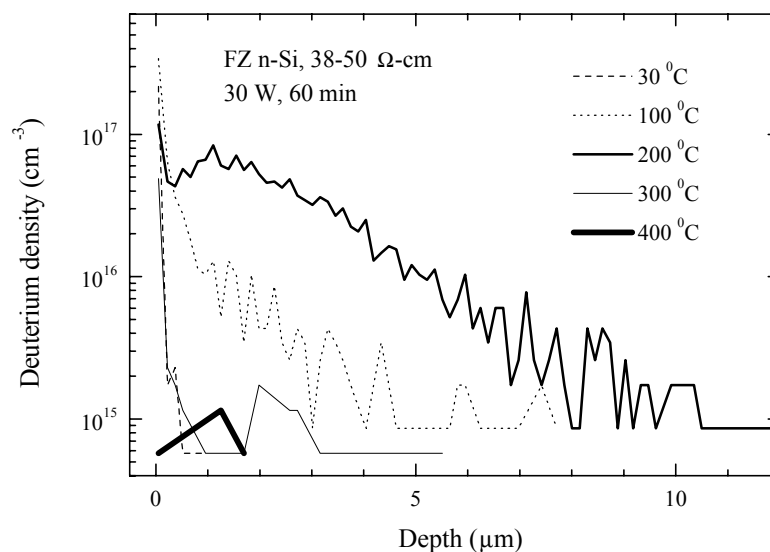


Figure 4.3: Deuterium profiles obtained in 38-50 Ω -cm FZ n-type silicon deuterated at 30 W for 60 minutes at temperatures in the range 30-400 $^{\circ}$ C. The measurements have been carried out at IFPAN.

pected, since the deuterium diffusion is limited by interactions with various traps (e.g. voids formed by the plasma treatment, oxygen, dopants) and by self-interactions resulting in molecule formation. Thus, in the present work, the resulting deuterium profile is obtained by the solution of a series of coupled differential equations describing these interactions. Such a model of limited hydrogen/deuterium diffusion was considered in detail by Mathiot [Mathiot 1989]. It was concluded that the model was consistent with a deuterium penetration depth of a few microns for experimental conditions comparable to the present work. Thus, the deuterium profiles obtained after plasma treatments at 30 $^{\circ}$ C, 100 $^{\circ}$ C and 200 $^{\circ}$ C appear consistent with in-diffusion of positively charged atomic deuterium and subsequent formation of interstitial molecules. As described in the background section, the literature contains experimental evidence for the generation of interstitial hydrogen molecules in plasma treated silicon.

The dramatic drop in deuterium concentration after plasma treatment at 300 $^{\circ}$ C appears somewhat surprising. There are, however, possible explanations. Firstly, the platelets formed by the plasma treatment act as efficient traps for atomic hydrogen, hence preventing the generation of interstitial molecules deeper in the bulk. The

generation of molecules within the platelets is dominant at temperatures 200-400 °C [Fukata 1997], [Leitch 1998b], [Kitajima 1999]. Secondly, the stability of the interstitial molecules themselves play a crucial role. The molecules can exist within the bulk up to temperatures of ~ 300 -350 °C [Markevich 2000a] but are highly mobile at these temperatures [Markevich 1998]. Thus, a strong out-diffusion and redistribution of the molecules takes place during the plasma treatment and the cool-down of the sample. Finally, at 400 °C, the molecules are not stable in the bulk and practically no deuterium is seen in the sample.

Further support for our interpretation of the SIMS data comes from comparison to the directly observed Raman intensities of interstitial hydrogen molecules in n-type silicon. Leitch et al. report that a plasma temperature of 150 °C is suitable for the molecule formation [Leitch 1998b], while Kitajima et al. find a maximum Raman signal at a treatment temperature of 250 °C [Kitajima 1999]. This is in good agreement with the present data, showing a maximum deuterium concentration at 200 °C. Further, no Raman signal related to interstitial molecules was observed in n-type silicon after treatment at 300 °C [Kitajima 1999].

4.3.3 Interaction of hydrogen with existing deep level defects

In this section, we briefly demonstrate the interactions between hydrogen introduced from a plasma and existing deep level defects, here in the form of substitutional platinum and radiation induced defects. The platinum was incorporated into 20 Ω -cm FZ n-Si by thermal evaporation followed by diffusion at 850 °C for 30 minutes. This procedure was carried out at IFPAN in Warsaw. Figure 4.4 shows 200 s⁻¹ conventional DLTS spectra of an as-diffused sample and a sample hydrogenated by exposure to a remote plasma for 60 minutes at ~ 120 °C. The as-diffused sample contains a strong peak at ~ 125 K, previously identified as the single acceptor level of substitutional platinum [Sachse 1997], [Sachse 1999]. Hydrogenation causes a strong decrease in the amplitude of this peak and the appearance of new peaks at ~ 95 K and ~ 260 K. These peaks have been identified as the double acceptor level of the platinum-dihydrogen complex and

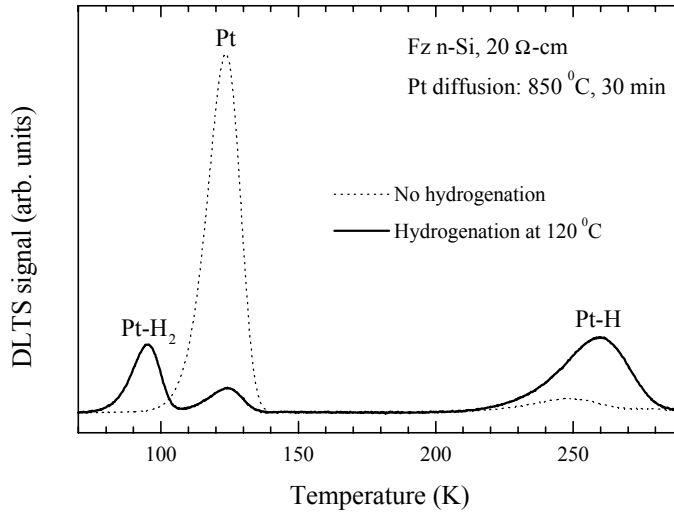


Figure 4.4: 200 s^{-1} conventional DLTS spectra of platinum diffused and platinum diffused, hydrogenated $20 \text{ } \Omega\text{-cm}$ FZ n-Si. The hydrogenation was carried out by remote plasma treatment for 60 minutes at $\sim 120 \text{ } ^\circ\text{C}$.

the single acceptor level of the platinum-hydrogen complex, respectively [Sachse 1997], [Sachse 1999]. A somewhat similar pattern was seen in electron irradiated n-type and p-type material. In this case, the amplitudes of the DLTS peaks related to the pure radiation induced defects were decreased by hydrogenation of the material, while new hydrogen-related peaks appeared in the spectra. These data will be presented and discussed in details in Chapter 7. An important observation in both the platinum diffused and the irradiated material was an overall decrease in the concentration of electrically active defects. Thus, our results demonstrate the interactions between existing deep level defects and hydrogen introduced from a remote plasma. These interactions significantly alter the electronic properties of the defects, shifting the level position within the band gap or completely removing the electrical activity.

4.3.4 Formation of deep level defects by plasma treatment

In this section, we consider the formation of deep level defects in $38\text{-}50 \text{ } \Omega\text{-cm}$ FZ n-type silicon deuterated for 60 minutes at temperatures in the range $30\text{-}400 \text{ } ^\circ\text{C}$. SIMS profiles for these samples were presented in Figure 4.3. Figure 4.5 shows 200 s^{-1} conventional

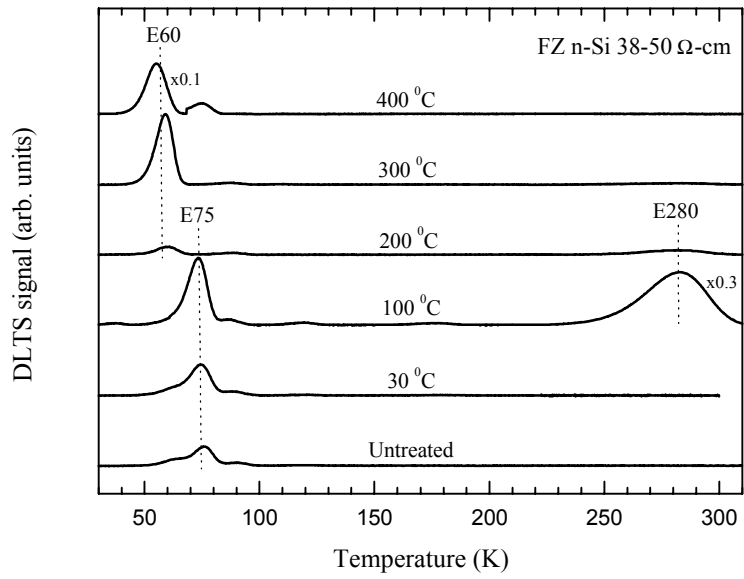


Figure 4.5: 200 s^{-1} conventional DLTS spectra of 38-50 Ω -cm FZ n-type silicon deuterated for 60 minutes at temperatures in the range 30-400 $^{\circ}\text{C}$.

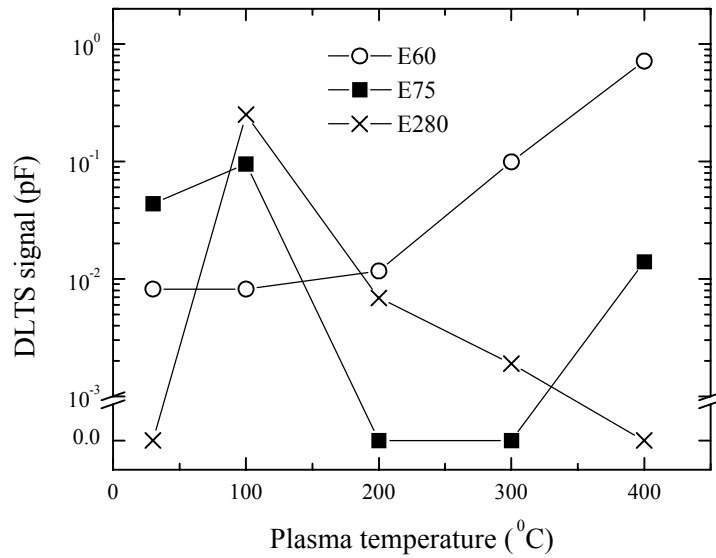


Figure 4.6: DLTS signal amplitudes of E60, E75 and E280 as a function of treatment temperature.

DLTS spectra of an untreated sample and samples deuterated at temperatures 30 °C, 100 °C, 200 °C, 300 °C and 400 °C. Three dominant peaks, labelled E60, E75 and E280, are observed at some stage of the treatment procedure. Figure 4.6 depicts the amplitudes of the DLTS signals as a function of treatment temperature for the bias conditions used to obtain the data in Figure 4.5. The formation of E60 rapidly increases with treatment temperature. The spatial profile shows a practically uniform concentration into a depth of at least 7 μm for all treatment temperatures, the trap concentration being $\sim 1 \times 10^{11} \text{ cm}^{-3}$ at 200 °C, $\sim 1 \times 10^{12} \text{ cm}^{-3}$ at 300 °C and $\sim 2 \times 10^{13} \text{ cm}^{-3}$ at 400 °C. E75 is seen in untreated material but is increased by plasma treatments at 30 °C and 100 °C. E280 is dominant after 100 °C and practically vanishes at higher treatment temperatures. The formation of the defect shows a remarkably strong dependence of sample depth, the concentration decaying from $\sim 1 \times 10^{13} \text{ cm}^{-3}$ at $\sim 0.7 \mu\text{m}$ to $\sim 1 \times 10^{12} \text{ cm}^{-3}$ at $\sim 1.5 \mu\text{m}$ after treatment at 100 °C.

Laplace DLTS spectra of E75 and E280 contain sharp single lines with no measurable enhancement of the electron emission rate for increasing electric field strength. In contrast, the Laplace spectra of E60 show either a broad structure or multiple peaks, indicating a distribution of time constants in the measurement region. It was only possible to obtain a well-defined peak by using Laplace Double DLTS with a narrow measurement region. The inset in Figure 4.7 shows examples of Laplace Double DLTS spectra of E60 obtained at 55 K under different bias conditions. The spectra demonstrate a strong enhancement of the electron emission rate with electric field strength, hence explaining the slightly varying peak positions of E60 in the conventional DLTS spectra in Figure 4.5. Figure 4.7 depicts the emission rate of E60 at 55 K relative to the zero-field emission rate as a function of the field parameter $\omega = \frac{\sqrt{e^3 \mathcal{E} / \pi \epsilon_s}}{k_B T}$, where \mathcal{E} is the average electric field strength in the measurement region. The data for the field dependence are well described by the three dimensional Poole-Frenkel effect for an electron attracted to a positive charge of magnitude q . The fitting gives $q = 2.1e$. Thus, the data strongly indicate that the electric field dependence is caused by the Poole-Frenkel effect and that the empty defect centre is doubly positively charged, i.e.

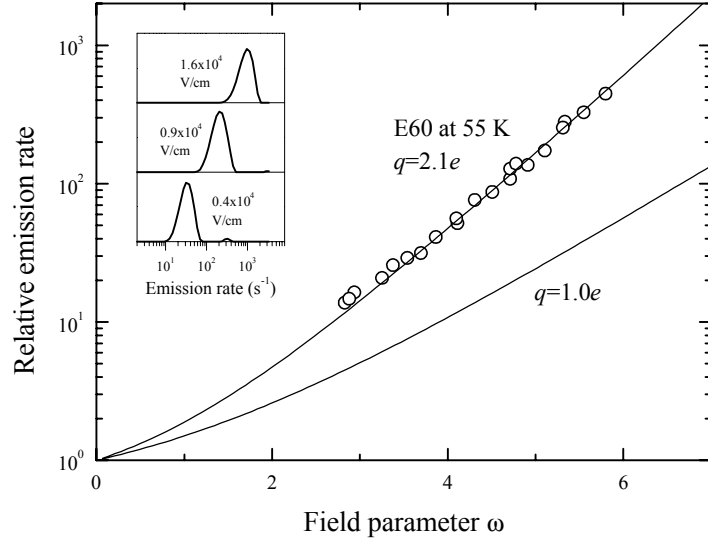


Figure 4.7: The emission rate of E60 at 55 K relative to the zero-field emission rate as a function of the field parameter $\omega = \frac{\sqrt{e^3 \mathcal{E} / \pi \epsilon_s}}{k_B T}$. The solid line represents the best fit to the data obtained from the three dimensional Poole-Frenkel effect. The zero-field emission rate was obtained by extrapolation of the curve to $\omega = 0$. The fitting gives the value $q = 2.1e$ for the charge of the defect centre. The field effect expected for a singly charged centre is shown for comparison. Inset shows Laplace DLTS spectra obtained at 55 K at three different field strengths.

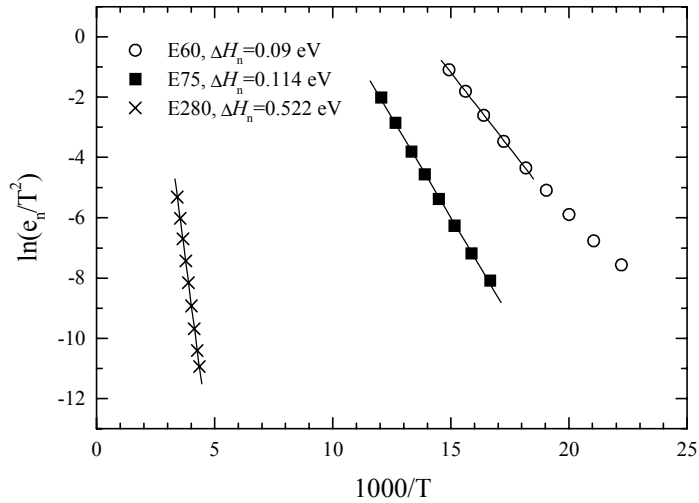


Figure 4.8: Arrhenius plots for the electron emissions from E60, E75 and E280. The data for E60 have been obtained in an electric field of approximately 5×10^3 V/cm.

E60 is a double donor level.

Figure 4.8 shows Arrhenius plots for the electron emissions from E60, E75 and E280. The data have been obtained from series of Laplace DLTS measurements carried out at a number of temperatures. We determine the activation enthalpies as $\Delta H_n = 0.114$ eV for E75 and $\Delta H_n = 0.522$ eV for E280. The data for E60 have been obtained in an electric field of approximately 5×10^3 V/cm. The strong field dependence for this level causes a slight bending of the Arrhenius curve at lower temperatures. We estimate the activation enthalpy for E60 as $\Delta H_n = 0.09$ eV at a field strength of $\sim 5 \times 10^3$ V/cm.

The defect E60 has a remarkable resemblance to oxygen-related thermal double donors (TDD's) [Jones 1996]. This is a family of small oxygen-related clusters that arise in silicon after heat treatments below ~ 700 °C, the generation peaking at ~ 450 °C. Their formation critically depends on the concentration of interstitial oxygen and is significantly enhanced by hydrogenation. The TDD's are double donors located around $E_c - 0.15$ eV at zero electric field [Kimerling 1981]. Despite intense studies, the exact structure of the TDD's and the microscopic processes leading to their formation are still debated. The energy barrier for the formation process is much smaller than the barrier for the jump of an interstitial oxygen atom in the lattice. Hence, the oxygen diffusion leading to the TDD formation takes place as part of a fast-diffusing defect complex, possibly the oxygen dimer [Murin 1998]. The above characteristics are in good agreement with the observed behavior of E60. Firstly, E60 was formed after deuterium plasma treatments at 200-400 °C, the concentration rapidly increasing with treatment temperature. Secondly, the spatial profile of E60 is practically uniform up to a depth of ~ 7 μm , suggesting no direct relation to deuterium. A uniform concentration profile of TDD's formed in hydrogen plasma treated n-type silicon has been reported elsewhere [Simoen 2002]. Third, the double donor character of E60 and its thermal activation enthalpy of $\Delta H_n = 0.09$ eV in an electric field of $\sim 5 \times 10^3$ V/cm agrees with the electronic properties of the TDD's. Finally, a direct comparison between E60 and oxygen-related TDD's formed in heat treated Cz silicon showed practically identical Laplace DLTS peak positions at a number of temperatures and electric field strengths.

The proposal that E60 is related to TDD's is remarkable considering that it has been formed in FZ silicon. Most previous observations of TDD's have been done in Cz silicon with a much higher oxygen content. Recently, however, Simoen et al. reported formation of TDD's in oxygen-doped high-resistivity FZ n-type silicon containing an average interstitial oxygen concentration of $\sim 10^{17} \text{ cm}^{-3}$ [Simoen 2002]. This value is only by a factor of 2-5 higher than the expected oxygen content in the FZ material used in the present work. An attempt to directly measure the concentration of interstitial oxygen by means of infrared absorption was not successful. A possible explanation for the observation of TDD's in FZ silicon lies in the dramatic enhancement of the TDD generation rate by hydrogenation, as previously established [Jones 1996]. Presumably, this enhancement is related to an increase in the mobility of the fast-diffusing oxygen-related complex as a result of interaction with hydrogen. Markevich et al. report an increase in the oxygen diffusivity by a factor of 10^5 - 10^6 in silicon crystals containing 10^{15} - 10^{16} cm^{-3} of hydrogen compared to crystals with low hydrogen concentration [Markevich 2000a]. Thus, the large concentration of diffusing deuterium atoms during plasma treatment at 200-400 °C offers a possible explanation for the observation of TDD's in FZ n-type silicon.

Our experimental results do not allow us to reach any conclusion about the identities of E75 and E280. For both levels, the lack of electric field dependence for the emission process indicates no Coulombic interaction between the carrier and the defect centre. Thus, we identify E75 and E280 as deep acceptor levels located at $E_c - 0.114 \text{ eV}$ and $E_c - 0.522 \text{ eV}$, respectively. We interpret that E280 is identical to the deep acceptor at $E_c - 0.51 \text{ eV}$ observed by Johnson et al. after hydrogen plasma treatment at 150 °C [Johnson 1987]. The strong spatial profile of E280 indicates either an extended deuterium-related defect or a multi-vacancy-deuterium complex formed close to the surface. Further work is required to establish the identities of E75 and E280.

4.4 Summary

The incorporation of hydrogen/deuterium into n-type silicon by exposure to a remote plasma has been studied by SIMS, capacitance-voltage measurements and DLTS. Room temperature deuterium plasma treatment introduces deuterium-related platelets into the sub-surface region of the material and passivates more than 50% of the background carriers by the formation of deuterium-donor complexes. The latter complexes form the dominant deuterium-related species beyond $\sim 0.3 \mu\text{m}$. The deuterium incorporation into lowly doped FZ n-type silicon at elevated treatment temperatures is consistent with the formation of interstitial molecules in the bulk. The molecule generation is strongest for treatment temperatures around $200 \text{ }^\circ\text{C}$, where the deuterium profile extends to a depth of $\sim 10 \mu\text{m}$ from the surface with a maximum concentration of $\sim 10^{17} \text{ cm}^{-3}$ for a treatment time of 60 minutes. Treatments carried out around $100 \text{ }^\circ\text{C}$ introduce two deuterium-related acceptor levels into the band gap at $E_c - 0.114 \text{ eV}$ and $E_c - 0.522 \text{ eV}$. It was proposed that oxygen-related thermal double donors are formed at higher treatment temperatures as a result of the strongly enhanced oxygen diffusion by interactions with hydrogen/deuterium.

Chapter 5

The hydrogen-carbon pair in n-type silicon

Carbon is incorporated into silicon during crystal growth by the float zone as well as the Czochralski technique. For both growth techniques, the carbon concentration exceeds $\sim 10^{15} \text{ cm}^{-3}$. The carbon atoms mainly occupy substitutional sites in the silicon lattice, forming an immobile, iso-valent defect. The complex acts as an effective trap for a number of other impurities, including oxygen, interstitial carbon and hydrogen. In some cases, the resulting complexes are electrically active with energy levels in the band gap. A review on carbon in silicon has been given by Davies and Newman [Davies 1994]. The aim of this chapter is to study the interactions of substitutional carbon with atomic hydrogen in n-type silicon and describe the structural, electronic and piezospectroscopic properties of the hydrogen-carbon pair¹.

¹This work was a collaborative study between the semiconductor groups at UMIST and the universities in Aarhus and Exeter. The work has been published in [Andersen 2001], [Andersen 2002]. The experimental part consisted of DLTS studies of proton implanted and chemically etched carbon rich n-type silicon. The latter data are presented in the present chapter. The author was also involved in the study of the implanted material but was not the principal experimentalist. Therefore, these data are not included in the thesis but will be treated as a reference.

5.1 Background

5.1.1 Theoretical work

The hydrogen-carbon pair has been modeled by several theoretical groups during the past decade. Theoretical investigations include work by Maric et al. [Maric 1993], Kaneta et al. [Kaneta 1995] and several papers by the Exeter group [Leary 1998], [Hoffmann 2000], [Andersen 2001], [Andersen 2002]. A number of possible structures for the hydrogen-carbon pair have been proposed. We will consider three of these: (i) the $\text{SiH}_{\text{BC}}\text{C}_{\text{s}}$ configuration where the hydrogen atom is located close to a Si-C bond-center site, bound mainly to the substitutional carbon atom, (ii) the $\text{SiC}_{\text{s}}\text{H}_{\text{AB}}$ configuration where the hydrogen atom is anti-bonded to the substitutional carbon atom and (iii) the $\text{SiH}_{\text{BC}}\text{SiC}_{\text{s}}$ configuration where the hydrogen atom is bond-centered between two silicon atoms located as first and second nearest neighbors to the substitutional carbon atom. The three structures are depicted in Figure 5.1.

In the positive and neutral charge states, the bond-center configuration $\text{SiH}_{\text{BC}}\text{C}_{\text{s}}$ is found by most theoretical calculations to form the lowest energy configuration. It is by 0.5-0.7 eV more stable than the anti-bonding configuration $\text{SiC}_{\text{s}}\text{H}_{\text{AB}}$ in the positive charge state and by 0.3-0.6 eV more stable than $\text{SiC}_{\text{s}}\text{H}_{\text{AB}}$ in the neutral charge state [Kaneta 1995], [Leary 1998], [Andersen 2002]. In the negative charge state, however,

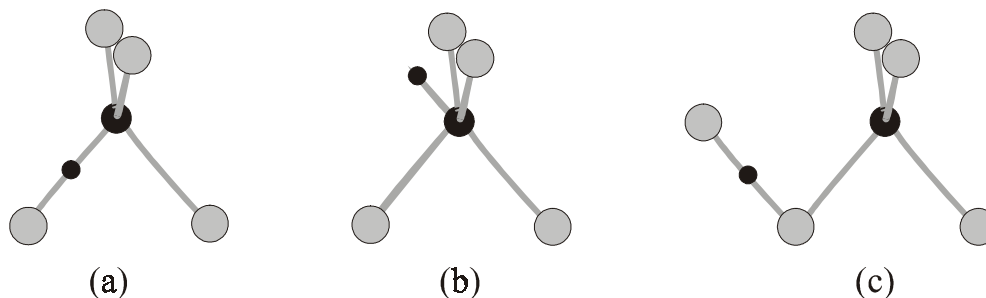


Figure 5.1: Illustrations of (a) configuration $\text{SiH}_{\text{BC}}\text{C}_{\text{s}}$, (b) configuration $\text{SiC}_{\text{s}}\text{H}_{\text{AB}}$ and (c) configuration $\text{SiH}_{\text{BC}}\text{SiC}_{\text{s}}$. Silicon atoms are shown as grey spheres, carbon and hydrogen atoms as large and small black spheres, respectively.

disagreement exists whether the lowest energy structure is formed by $\text{SiH}_{\text{BC}}\text{C}_{\text{s}}$ or by $\text{SiC}_{\text{s}}\text{H}_{\text{AB}}$. All calculations suggest that the two structures are very close in energy [Maric 1993], [Kaneta 1995], [Leary 1998], [Andersen 2002]. The $\text{SiH}_{\text{BC}}\text{SiC}_{\text{s}}$ configuration has only been modeled by the Exeter group. It was found to be 0.2 eV higher in energy than the $\text{SiH}_{\text{BC}}\text{C}_{\text{s}}$ configuration in the positive charge state, while it is unstable in the negative charge state [Hoffmann 2000], [Andersen 2002].

Theoretical calculations of band gap energy levels and piezospectroscopic parameters for the three structures have also been carried out by the Exeter group. These will be presented later in the chapter and directly compared to the experimental results.

5.1.2 Experimental work

An electron trap with a level at $E_c - 0.16$ eV formed after room temperature chemical etching of carbon-rich n-type silicon has been related to the hydrogen-carbon pair in several DLTS studies. The trap has been investigated by a German group [Endrös 1989], [Endrös 1992], [Csaszar 1994] and by a Japanese group [Yoneta 1991], [Kamiura 1992], [Kamiura 1997], [Fukuda 1999], [Kamiura 2000], [Fukuda 2001], [Kamiura 2002]. The German group reports a strong electric field dependence of the electron emission process and finds that removal of the hydrogen-carbon complexes results in a similar decrease in the number of active donors. On this basis, it was concluded that the level at $E_c - 0.16$ eV forms a single donor. The data for the field effect, however, appear somewhat inconsistent. In the early papers, the field effect observed below 2×10^4 V/cm was found to be much weaker than predicted by a three-dimensional Coulomb model [Endrös 1989], [Endrös 1992], while a later study showed a much stronger than Coulombic field dependence even below 2×10^4 V/cm [Csaszar 1994].

The annealing behavior of the defect depends critically on the Fermi level position, illumination conditions and the bias applied to the sample during annealing [Yoneta 1991], [Endrös 1992], [Kamiura 1992], [Kamiura 1997]. It has been concluded that the dissociation is strongly dependent on the charge state of the complex, i.e. it is much more stable in the electron-empty state than in the electron-occupied state. The

energy barrier for the dissociation of the complex has been obtained as 0.5 eV in the electron-occupied state and 1.3 eV in the electron-empty state [Kamiura 1997].

The Japanese group has studied the trap at $E_c - 0.16$ eV by uniaxial stress combined with conventional DLTS and finds a trigonal symmetry of the atomic structure [Kamiura 1997], [Fukuda 2001]. The defect was assigned to the bond-center configuration $\text{SiH}_{\text{BC}}\text{C}_{\text{s}}$. Stress-induced alignment has been observed above 240 K under zero bias and above 300 K under reverse bias [Fukuda 1999], [Kamiura 2000], [Kamiura 2002] but no detailed piezospectroscopic analysis of the complex has been carried out.

A hole trap with a level at $E_v + 0.33$ eV has also been related to the hydrogen-carbon pair [Kamiura 1995]. This defect was formed by room temperature chemical etching or by 100 °C hydrogen plasma treatment of carbon-rich p-type silicon. The hole capture cross section of the trap was determined as 2×10^{-16} cm² and the hole emission process showed no electric field dependence in fields below 6×10^3 V/cm. These properties suggest a deep donor level. The defect was tentatively ascribed to the anti-bonding configuration $\text{SiC}_{\text{s}}\text{H}_{\text{AB}}$.

Recently, local vibrational modes observed by infrared absorption spectroscopy [Hoffmann 2000] and a deep donor level located at $E_c - 0.22$ eV observed by DLTS [Andersen 2001], [Andersen 2002] have been identified as the $\text{SiH}_{\text{BC}}\text{SiC}_{\text{s}}$ configuration. In both cases, the complex was formed by low temperature proton implanted of carbon rich n-type silicon. The $\text{SiH}_{\text{BC}}\text{SiC}_{\text{s}}$ defect is irreversibly lost after annealing at approximately 225 K. In the DLTS study, the complex converts to another hydrogen-carbon complex with identical properties to the trap with a level at $E_c - 0.16$ eV described above. No local vibrational modes were observed by infrared absorption after annealing of the $\text{SiH}_{\text{BC}}\text{SiC}_{\text{s}}$ defect.

5.2 Sample preparation

Samples were prepared from 20 Ω-cm FZ n-type silicon doped with carbon atoms of density $\sim 10^{17}$ cm⁻³. All the samples were cut from the same wafer with the (110)

surface orientation in the shape of $1 \times 2 \times 7$ mm blocks with the longest dimension parallel to one of the three major crystallographic directions, $\langle 100 \rangle$, $\langle 110 \rangle$ and $\langle 111 \rangle$. Hydrogenation was carried out by wet chemical etching at room temperature for 5 minutes, using an acid solution of HNO_3 (70%) and HF (48%) in the ratio 10:1. Schottky diodes and Ohmic contacts were formed by evaporation of gold and aluminum, respectively.

5.3 Experimental results

Conventional DLTS spectra obtained after hydrogenation of the carbon-rich samples reveal a single peak at ~ 90 K. Laplace DLTS measurements confirm that the peak contains a single emission component. We label the peak $(\text{C-H})_{\text{II}}^2$. A detailed analysis of the electronic and piezospectroscopic properties of $(\text{C-H})_{\text{II}}$ is given below.

5.3.1 Electronic characterization

Figure 5.2 shows an Arrhenius plot for the electron emission from $(\text{C-H})_{\text{II}}$ obtained from a series of Laplace DLTS measurements carried out at different temperatures. We determine the activation enthalpy as $\Delta H_n = 0.155$ eV and the apparent electron capture cross section as $\sigma_n^a = 4 \times 10^{-16}$ cm^2 (equation (2.12)). The results are displayed in Table 5.1. Figure 5.2 and Table 5.1 compare our results to literature data obtained for similar electron traps observed in carbon-rich material after wet chemical etching [Endrös 1989], [Yoneta 1991], [Csaszar 1994] and after low temperature proton implantation followed by annealing at room temperature [Andersen 2002]. A clear correlation exists between the various sets of emission data, suggesting that the traps are identical.

Direct capture measurements of $(\text{C-H})_{\text{II}}$ have been carried out at 85 K and 110 K by using the filling pulse method. Figure 5.3 shows the relative signal reduction as a function of fill pulse width. The capture data are well described by exponential

²We adopt the notation used in the papers [Andersen 2001], [Andersen 2002] published from this work.

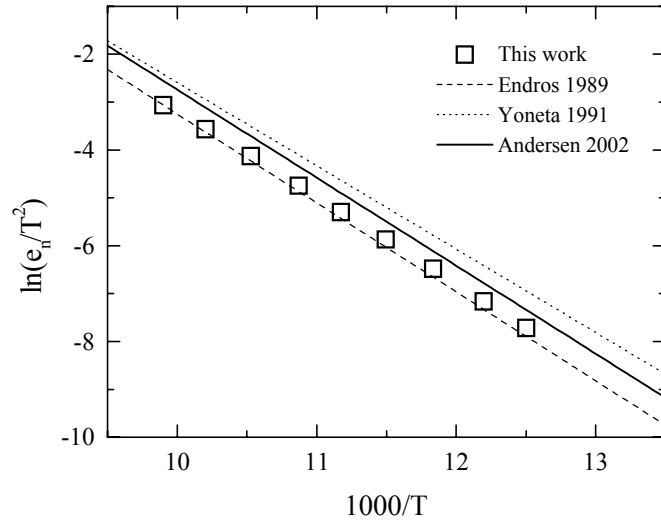


Figure 5.2: Arrhenius plot for the electron emission from $(\text{C-H})_{\text{II}}$. The results are compared to literature data for similar electron traps related to hydrogen and carbon.

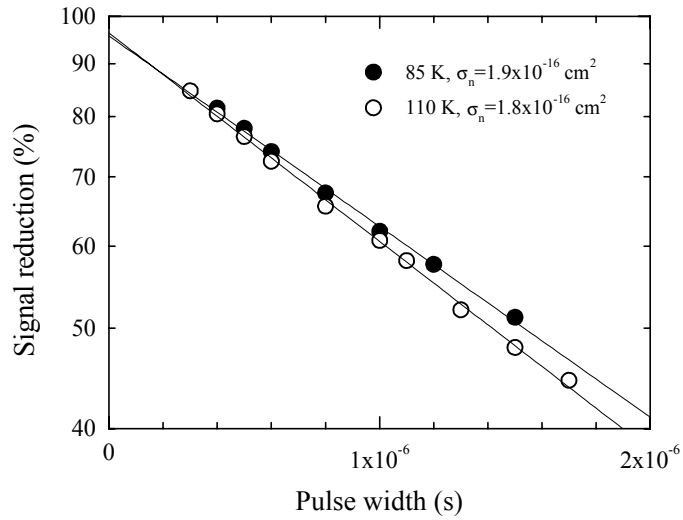


Figure 5.3: Capture data for $(\text{C-H})_{\text{II}}$ obtained at 85 K and 110 K. The graph shows the signal reduction $\frac{\Delta C_0^{\text{max}} - \Delta C_0(t_P)}{\Delta C_0^{\text{max}}}$ as a function of fill pulse width t_P . The maximum amplitude ΔC_0^{max} has been obtained for a pulse width of 1 ms.

| | ΔH_n (eV) | σ_n^a (cm ²) | σ_n (cm ²) | Electric field dependence |
|-----------------|-------------------|---------------------------------|-------------------------------|----------------------------------|
| This work | 0.155 | 4×10^{-16} | 2×10^{-16} | None ($< 1.5 \times 10^4$ V/cm) |
| [Endrös 1989] | 0.16 | 7×10^{-16} | | <CP ($< 2 \times 10^4$ V/cm) |
| [Yoneta 1991] | 0.15 | | 4×10^{-16} | <CP ($< 1 \times 10^4$ V/cm) |
| [Csaszar 1994] | 0.16 | | | >CP ($< 5 \times 10^4$ V/cm) |
| [Andersen 2002] | 0.159 | 9×10^{-16} | | None ($< 1.5 \times 10^4$ V/cm) |

Table 5.1: Activation enthalpy ΔH_n , apparent electron capture cross section σ_n^a , directly measured electron capture cross section σ_n and electric field dependence of (C-H)_{II}. The results from the present work are compared to literature data. Electric field dependencies stronger and weaker than a Coulombic potential are indicated as >CP and <CP, respectively.

refilling kinetics, equation (3.20), for pulse widths in the range 0.3-2.0 μ s. The electron capture cross sections at 85 K and 110 K are determined from equation (2.8) as $\sigma_n(85 \text{ K}) = 1.9 \times 10^{-16} \text{ cm}^2$ and $\sigma_n(110 \text{ K}) = 1.8 \times 10^{-16} \text{ cm}^2$, respectively. Thus, no energy barrier for the capture process is observed. The capture data are displayed in Table 5.1.

The electric field dependence of the electron emission from (C-H)_{II} has been studied at 85 K by means of Laplace Double DLTS. The reverse bias was fixed at -9 V and measurements were carried out with several pairs of fill pulses. The average electric field strength in the measurement region was estimated from the capacitance-voltage characteristics of the given device. The experimental conditions allowed field strengths below $\sim 1.5 \times 10^4$ V/cm to be studied. Practically no enhancement of the electron emission rate was observed. The maximum ratio of emission rates in different fields was below 1.2. In comparison, a Hartke model describing a three dimensional Coulombic interaction between a charged centre and a carrier of opposite polarity yields an emission rate ratio above 3.0 between the minimum and maximum electric field strengths considered. Thus, the results indicate that no such Coulombic interaction takes place. The lack of field dependence is in direct disagreement with results reported by the German group [Endrös 1992], [Csaszar 1994]. Table 5.1 compares the electric field dependencies

reported in various publications.

5.3.2 Uniaxial stress measurements

Figure 5.4 shows 85 K Laplace DLTS spectra of $(\text{C-H})_{\text{II}}$ obtained at zero stress and under uniaxial stress along the three major crystallographic directions, $\langle 100 \rangle$, $\langle 110 \rangle$ and $\langle 111 \rangle$. The zero-stress peak splits into two components with approximate intensity ratios 2 : 2 for the $\langle 110 \rangle$ stress direction and 3 : 1 for the $\langle 111 \rangle$ stress direction. No splitting is observed for the $\langle 100 \rangle$ stress direction. For all directions of stress, the amplitude of the split lines sum to the amplitude of the zero-stress line. The splitting pattern establishes the trigonal symmetry of the $(\text{C-H})_{\text{II}}$ defect (Table 2.2) in agreement with data from conventional DLTS [Kamiura 1997], [Fukuda 2001]. The trigonal symmetry class is consistent with the bond-center structure $\text{SiH}_{\text{BC}}\text{C}_{\text{s}}$ as well as the anti-bonding structure $\text{SiC}_{\text{s}}\text{H}_{\text{AB}}$.

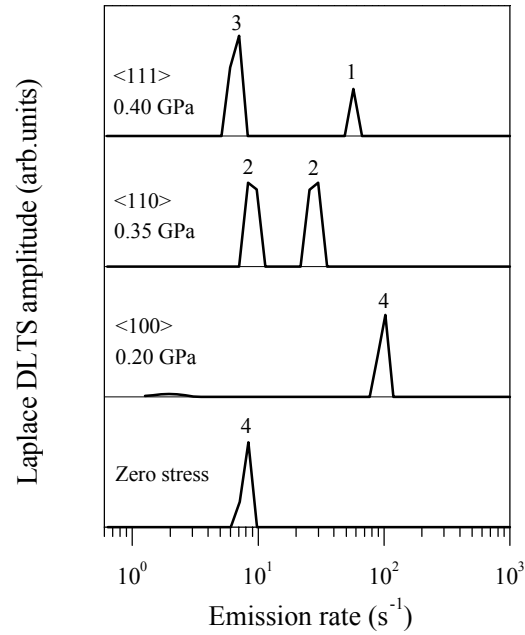


Figure 5.4: 85 K Laplace DLTS spectra of $(\text{C-H})_{\text{II}}$ obtained at zero stress and under uniaxial stress along the three major crystallographic directions, $\langle 100 \rangle$, $\langle 110 \rangle$ and $\langle 111 \rangle$. The splitting pattern establishes the trigonal symmetry of the complex.

The influence of uniaxial stress on the ionization process has been investigated for the various non-equivalent configurations of the $(\text{C-H})_{\text{II}}$ complex. Laplace DLTS spectra were obtained at 85 K for several stresses along the three major crystallographic directions. Direct capture measurements carried out at 0.35 GPa along the $\langle 111 \rangle$ direction showed no influence of stress on the capture process. Thus, we assume that a change in electron emission rate with stress is entirely related to a change in ionization enthalpy. Figure 5.5 shows the energy shifts $dE = k_B T \ln \left(\frac{e_n(P)}{e_n(0)} \right)$ versus applied stress for the individual lines presented in Figure 5.4. The shifts are linear in stress in agreement with the piezospectroscopic theory described in Chapter 2. The values of the shifts are obtained as 109 meV/GPa for the $\langle 100 \rangle$ stress direction, 14 and 34 meV/GPa for the $\langle 110 \rangle$ stress direction and -3 and 26 meV/GPa for the $\langle 111 \rangle$ stress direction. This yields a line splitting of 20 meV/GPa for $\langle 110 \rangle$ -stress and 29 meV/GPa for $\langle 111 \rangle$ -stress. According to the piezospectroscopic theory for a trigonal defect centre, the line splitting in the $\langle 111 \rangle$ stress direction is larger by a factor of $\frac{4}{3}$ than the line splitting in the $\langle 110 \rangle$ stress direction (Table 2.2). This ratio is maintained within experimental error. However, a significant scattering was observed between the experimental data obtained for different $\langle 110 \rangle$ and $\langle 111 \rangle$ oriented samples. The values of the individual energy shifts could differ by up to 25%.

Stress-induced alignment experiments of the $(\text{C-H})_{\text{II}}$ complex have been carried out for the $\langle 111 \rangle$ stress direction. No effect of alignment was observed below 250 K but application of stress around room temperature increases the intensity of the low frequency line relative to the intensity of the high frequency line. Complete alignment changes the 3 : 1 splitting to a 4 : 0 splitting. The equilibrium intensity ratio of the two lines was obtained at 340 K under reverse bias and at 330 K under zero bias by applying the stress for 60 minutes and 15 minutes, respectively. Subsequently, the sample was cooled quickly to 85 K, where the intensities of the Laplace DLTS peaks were evaluated. It was checked directly that the steady-state condition was reached. Figure 5.6 shows the equilibrium amplitude ratio of the high frequency line and the low frequency line as a function of applied stress. The energy separation is linear with stress, in agreement

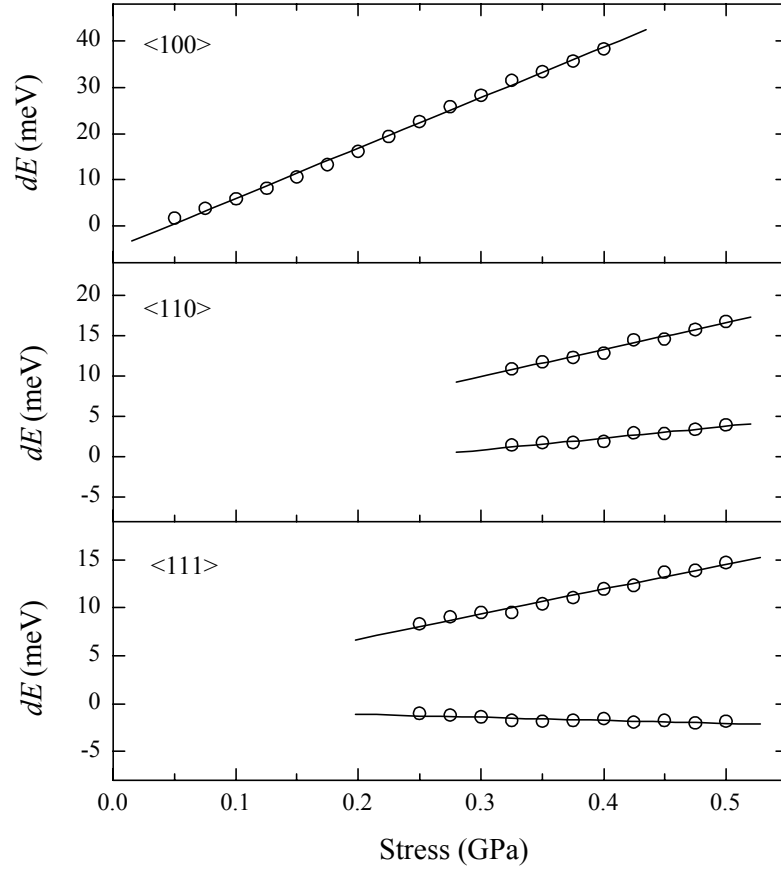


Figure 5.5: Energy shifts dE versus applied stress for the individual lines of $(\text{C-H})_{\text{II}}$ under stress along the $\langle 100 \rangle$, $\langle 110 \rangle$ and $\langle 111 \rangle$ directions. The energy shifts have been obtained as $dE = k_B T \ln \left(\frac{e_n(P)}{e_n(0)} \right)$, where $e_n(P)$ is the directly measured electron emission rate at the given stress. A positive slope means that the energy level approaches the conduction band under stress.

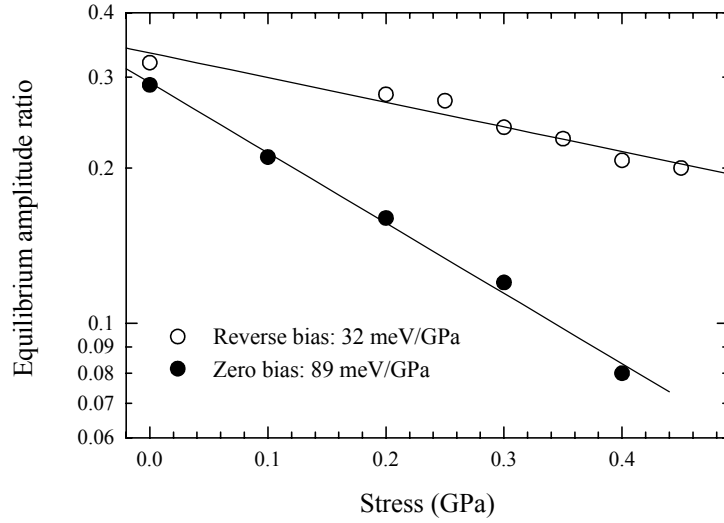


Figure 5.6: Equilibrium amplitude ratio of the high frequency and low frequency lines as a function of applied stress along the $\langle 111 \rangle$ direction. The steady-state condition has been reached at 340 K under reverse bias and at 330 K under zero bias.

with equation (2.31). We obtain the stress coefficients as 32 meV/GPa for alignment under reverse bias and 89 meV/GPa for alignment under zero bias. Shortly, we relate these values to the piezospectroscopic parameters for the different charge states of the $(\text{C-H})_{\text{II}}$ complex.

The zero-stress reorientation barrier of the $(\text{C-H})_{\text{II}}$ complex has also been studied. Initially, complete alignment was carried out at 280 K under 0.40 GPa stress along the $\langle 111 \rangle$ direction with no bias applied to the sample. Subsequently, the complexes were gradually mis-aligned during a series of steps of isothermal annealings at zero stress and zero bias. After each step, the sample was cooled quickly to 85 K and the intensities of the two Laplace DLTS peaks were evaluated. This allowed us to observe the kinetics of the zero-stress reorientation process. The procedure was carried out at temperatures in the range 250-290 K. Figure 5.7 shows the amplitude ratio D of the high frequency line relative to the sum of the two lines as a function of mis-alignment time for different temperatures. The ratio decays from the initial value $D = 0$ in the completely aligned state to the saturation value $D = \frac{1}{4}$ in the completely mis-aligned state. The corresponding Arrhenius plot for the reorientation process is depicted in

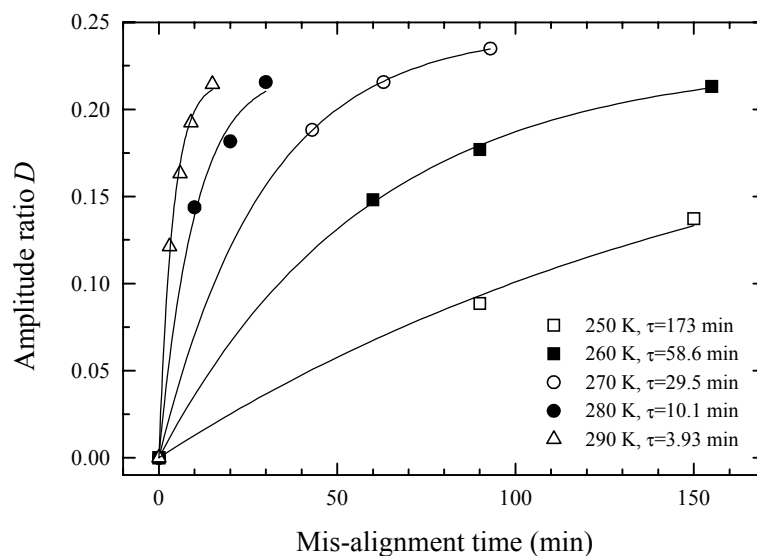


Figure 5.7: Zero-stress reorientation kinetics of $(\text{C-H})_{\text{II}}$ after complete alignment in the $\langle 111 \rangle$ stress direction. The graph shows the amplitude ratio D of the high frequency line relative to the sum of the two lines as a function of mis-alignment time for different temperatures. The experimental saturation values of D are in the range 0.22-0.25 for all temperatures.

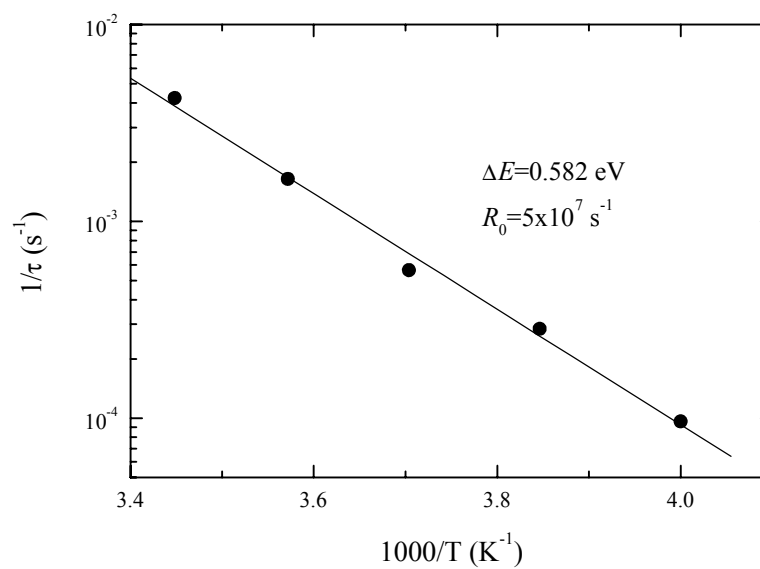


Figure 5.8: Arrhenius plot for the zero-stress reorientation of the $(\text{C-H})_{\text{II}}$ complex under zero bias.

Figure 5.8. We obtain the activation energy as $\Delta E = 0.582$ eV and the pre-exponential factor as $R_0 = 5 \times 10^7$ s⁻¹. The reorientation process was observed to be significantly slower with a reverse bias applied during the mis-alignment but no quantitative data have been obtained for this case.

5.4 Discussion

5.4.1 Donor/acceptor behavior of (C-H)_{II}

The charge state of a deep level studied by DLTS is usually determined from the electric field dependence of the carrier emission process and the carrier capture properties of the trap. In the present study of (C-H)_{II}, the directly measured electron capture cross section of 2×10^{-16} cm² and the lack of electric field dependence for the emission process clearly indicate that no Coulombic interaction takes place between the carrier and the defect centre. Note, that the field effect was studied for field strengths of sufficient magnitude to produce a measurable enhancement of the emission rate in the case of a Coulombic interaction. Thus, the experimental data suggest that (C-H)_{II} is a single acceptor level.

Further support for this assignment comes from comparison with theoretical modeling. Calculations carried out by the Exeter group show that the bond-center structure SiH_{BC}C_s and the anti-bonding structure SiC_sH_{AB} both introduce deep acceptor levels into the band gap close to the observed position of (C-H)_{II} at $E_c - 0.155$ eV [Andersen 2001], [Andersen 2002]³. In comparison, no donor levels are found in the upper part of the band gap.

Finally, the acceptor nature of (C-H)_{II} is supported by recent studies of proton implanted carbon-rich n-type silicon [Andersen 2001], [Andersen 2002]. In this work, an electron trap with a level at $E_c - 0.22$ eV was formed after implantation at 70 K. The trap, labelled (C-H)_I, was assigned to the donor level of the SiH_{BC}SiC_s configuration. After annealing at 225 K, the (C-H)_I defect irreversibly reconfigures to

³Below, we establish that (C-H)_{II} originates from either SiH_{BC}C_s or SiC_sH_{AB}.

another hydrogen-carbon complex, which introduces a level at $E_c - 0.159$ eV with similar electronic properties to the $(\text{C-H})_{\text{II}}$ level studied in the present work (Table 5.1). A comparison of the field effects for the two traps showed a significant field-induced enhancement of the electron emission rate for $(\text{C-H})_{\text{I}}$, while no enhancement was observed for $(\text{C-H})_{\text{II}}$ in the same sample and under exactly the same experimental conditions. The relative difference between the electric field dependencies of $(\text{C-H})_{\text{I}}$ and $(\text{C-H})_{\text{II}}$ is another indication of the acceptor nature of $(\text{C-H})_{\text{II}}$.

The above arguments seem to reliably establish the charge state of $(\text{C-H})_{\text{II}}$. However, as described in the background section, several authors have previously assigned a hydrogen-carbon-related trap level at $E_c - 0.16$ eV to a deep donor [Endrös 1989], [Yoneta 1991], [Endrös 1992], [Csaszar 1994]. It seems unlikely that the level observed by these authors is different from the $(\text{C-H})_{\text{II}}$ level studied in the present work as the sample preparation and the experimental parameters associated with the levels are practically identical (Table 5.1).

There are two main arguments supporting the assignment of $(\text{C-H})_{\text{II}}$ to a donor level. The first is the electric field dependence of the electron emission process reported by a German group in two studies [Endrös 1992], [Csaszar 1994]. In both cases, however, the experimental data do not fit to a Hartke model for the three dimensional Poole-Frenkel effect. Further, the two studies appear inconsistent. In the early paper, the field effect observed below 2×10^4 V/cm was found to be much weaker than predicted by a Coulomb model [Endrös 1992], while the later study showed a much stronger than Coulombic field dependence even below 2×10^4 V/cm [Csaszar 1994]. The second argument for the donor nature of $(\text{C-H})_{\text{II}}$ is the observation that removal of the hydrogen-carbon complexes by annealing results in a corresponding decrease in the number of active donors [Endrös 1992]. Though this forms a genuine argument, a similar effect could be expected for an acceptor, if the released atomic hydrogen from dissociation of the hydrogen-carbon pairs passivates the phosphorous atoms in the crystal. In this case, the decrease in the number of active donors is caused by a decrease in the number of active phosphorous atoms and is only indirectly related to the loss of hydrogen-carbon

pairs.

In conclusion, there exist literature data supporting the donor nature of $(\text{C-H})_{\text{II}}$. However, these seem to be outweighed by the arguments for the acceptor behavior of $(\text{C-H})_{\text{II}}$ described in the present work. We identify $(\text{C-H})_{\text{II}}$ as a deep acceptor level.

5.4.2 Microscopic identity of $(\text{C-H})_{\text{II}}$

As described in the background section, most theoretical groups agree that the bond-center configuration $\text{SiH}_{\text{BC}}\text{C}_{\text{s}}$ and the anti-bonding configuration $\text{SiC}_{\text{s}}\text{H}_{\text{AB}}$ form the lowest energy structures of the hydrogen-carbon pair in the neutral and negative charge states. Both structures have trigonal C_{3v} symmetry in agreement with the observed symmetry class of the $(\text{C-H})_{\text{II}}$ complex. Below, we compare the experimental parameters for $(\text{C-H})_{\text{II}}$ to those obtained for $\text{SiH}_{\text{BC}}\text{C}_{\text{s}}$ and $\text{SiC}_{\text{s}}\text{H}_{\text{AB}}$ from theoretical modeling carried out by the Exeter group. The data are displayed in Table 5.2.

The activation enthalpy for $(\text{C-H})_{\text{II}}$ was obtained as 0.155 eV (Figure 5.2). The calculations show that the bond-center structure as well as the anti-bonding structure introduce deep acceptor levels into the band gap relatively close to this position. The cluster method gives acceptor levels of $E_c - 0.15$ eV for $\text{SiH}_{\text{BC}}\text{C}_{\text{s}}$ and $E_c - 0.33$ eV for $\text{SiC}_{\text{s}}\text{H}_{\text{AB}}$ [Andersen 2001], while the supercell method gives acceptor levels of $E_c - 0.30$ eV for $\text{SiH}_{\text{BC}}\text{C}_{\text{s}}$ and $E_c - 0.63$ eV for $\text{SiC}_{\text{s}}\text{H}_{\text{AB}}$ [Andersen 2002]. Thus, the calculations favor the bond-center configuration. The difference, however, is not conclusive considering the large error ($\gtrsim 0.2$ eV) involved in the calculations of the levels.

Below, we argue that the reorientation of $(\text{C-H})_{\text{II}}$ around room temperature takes place in the negative charge state under zero bias and in the neutral charge state under reverse bias. Thus, the steady-state intensities of the two Laplace DLTS lines observed for the $\langle 111 \rangle$ stress direction after zero (reverse) bias stress-induced alignment around room temperature represent the equilibrium populations in the negative (neutral) charge state. The stress coefficients were obtained as $\Delta E^-/P = 89$ meV/GPa for the negatively charged centre and $\Delta E^0/P = 32$ meV/GPa for the neutrally charged centre (Figure 5.6). For a trigonal defect stressed along the $\langle 111 \rangle$ direction, the

| | This work (C-H) _{II} | Theoretical modeling | |
|--|----------------------------------|----------------------------------|----------------------------------|
| | | SiH _{BC} C _s | SiC _s H _{AB} |
| (- / 0) level (eV from E_c) | 0.155 | 0.15 / 0.30 | 0.33 / 0.63 |
| B_t^0 (eV) | -1.9 | -4.5 | -2.8 |
| B_t^- (eV) | -5.3 | -6.0 | -4.8 |
| $\frac{\partial E}{\partial P} _{\langle 110 \rangle}$ (meV/GPa) | 20 | 18.8 | 25.5 |
| $\frac{\partial E}{\partial P} _{\langle 111 \rangle}$ (meV/GPa) | 29 | 25.1 | 34.0 |

Table 5.2: Comparison of experimentally measured parameters for (C-H)_{II} to those obtained for the structures SiH_{BC}C_s and SiC_sH_{AB} from theoretical modeling. The two values for the calculated acceptor levels have been obtained by the cluster method and the supercell method, respectively.

difference in total energy between the two non-equivalent configurations is given by $\Delta E/P = -\frac{4}{3}B_t s_{44}$, where B_t is the trigonal (off-diagonal) component of the piezospectroscopic tensor (Table 2.2). We obtain $B_t^- = -5.3$ eV for the negative charge state and $B_t^0 = -1.9$ eV for the neutral charge state. Theoretical calculations give $B_t^- = -6.0$ eV and $B_t^0 = -4.5$ eV for the SiH_{BC}C_s configuration and $B_t^- = -4.8$ eV and $B_t^0 = -2.8$ eV for the SiC_sH_{AB} configuration [Andersen 2001], [Andersen 2002]. Thus, the measured piezospectroscopic tensor parameters of (C-H)_{II} are in closer agreement with the calculated values for the anti-bonding structure SiC_sH_{AB} compared to the bond-center structure SiH_{BC}C_s but the difference is not conclusive.

Finally, the magnitude of line splitting was obtained as $\frac{\partial E}{\partial P}|_{\langle 110 \rangle} = 20$ meV/GPa for the $\langle 110 \rangle$ stress direction and $\frac{\partial E}{\partial P}|_{\langle 111 \rangle} = 29$ meV/GPa for the $\langle 111 \rangle$ stress direction (Figure 5.5). The calculations give $\frac{\partial E}{\partial P}|_{\langle 110 \rangle} = 18.8$ meV/GPa and $\frac{\partial E}{\partial P}|_{\langle 111 \rangle} = 25.1$ meV/GPa for the SiH_{BC}C_s configuration and $\frac{\partial E}{\partial P}|_{\langle 110 \rangle} = 25.5$ meV/GPa and $\frac{\partial E}{\partial P}|_{\langle 111 \rangle} = 34.0$ meV/GPa for the SiC_sH_{AB} configuration [Andersen 2002]. For both structures, the agreement with the experimental data is good.

In summary, the convergence of the experimental and theoretical results strongly support the assignment of (C-H)_{II} to either the bond-center configuration SiH_{BC}C_s or the anti-bonding configuration SiC_sH_{AB}. However, the data do not allow us to reliably

distinguish between the two structures.

5.4.3 Analysis of piezospectroscopic parameters

Let us analyze the piezospectroscopic tensor components for $(\text{C-H})_{\text{II}}$ in more detail. The trigonal axis forms one of the principal axes of the defect with the corresponding eigenvalue $2B_t + B_h$, where B_t and B_h are the trigonal (off-diagonal) and hydrostatic (diagonal) tensor components, respectively (Table 2.1). The experimental data for $(\text{C-H})_{\text{II}}$ give the values $2B_t^- = -10.6$ eV for the negatively charged complex and $2B_t^0 = -3.8$ eV for the neutrally charged complex. Neglecting the hydrostatic term, the negative signs show that the total energy of the $(\text{C-H})_{\text{II}}$ defect is increased by a compressive stress applied along the trigonal axis of the defect (we use the sign convention that compressive stress is negative). That is, compressive stress applied along the axis of the carbon and hydrogen atoms is not energetically favorable for the complex. We conclude that the relaxation of the defect along the trigonal axis is outward. The effect is stronger for the negative charge state than for the neutral charge state.

5.4.4 Reorientation as a precursor for diffusion

We now consider the nature of the reorientation process for the $(\text{C-H})_{\text{II}}$ defect. During the measurements of the reorientation kinetics at temperatures 250-290 K with no bias applied to the sample, the Fermi level is approximately 0.10-0.15 eV below the $(\text{C-H})_{\text{II}}$ energy level. Thus, the majority of the complexes are in the neutral charge state, while the rest are in the negative charge state. Two possible scenarios can take place for the reorientation of the neutrally charged complex. The defect can either reorient directly in the neutral charge state or it can capture an electron and subsequently reorient in the negative charge state. The defect will experience the reorientation mechanism, which is energetically favorable. Our experimental data support the latter of the two possibilities. During the reorientation process, the occupancy of defects in the negative

charge state is given by:

$$\frac{N_t^-}{N_t} = f_{FD}(E_t) = \frac{1}{1 + \exp\left(\frac{E_t - E_F}{k_B T}\right)}, \quad (5.1)$$

where $f_{FD}(E)$ is the Fermi-Dirac distribution function and E_t is the (C-H)_{II} energy level. Assuming $E_t - E_F \gg k_B T$, equation (5.1) reduces to:

$$\frac{N_t^-}{N_t} \approx \exp\left(-\frac{E_t - E_F}{k_B T}\right) = \frac{n_c}{N_c} \exp\left(\frac{E_c - E_t}{k_B T}\right). \quad (5.2)$$

If the reorientation of the defect only takes place in the negative charge state, the effective Arrhenius expression for the reorientation process is given by:

$$1/\tau = \frac{n_c}{N_c} R_0^- \exp\left(-\frac{\Delta E^- - (E_c - E_t)}{k_B T}\right), \quad (5.3)$$

where ΔE^- and R_0^- are the energy barrier and the pre-exponential factor for the reorientation in the negative charge state, respectively. Thus, the effective pre-exponential factor will be by a factor of $\frac{n_c}{N_c}$ ($\sim 8 \times 10^{-6}$ under the given experimental conditions) smaller than the pre-exponential factor R_0^- for the negatively charged defect ($\sim 1 \times 10^{13} \text{ s}^{-1}$ for a classical jump process over a barrier). The experimental pre-exponential factor of $5 \times 10^7 \text{ s}^{-1}$ obtained from the Arrhenius plot for the reorientation process (Figure 5.8) is in excellent agreement with the estimated product of $\frac{n_c}{N_c}$ and R_0^- ($\sim 8 \times 10^7 \text{ s}^{-1}$). We interpret that the neutral (C-H)_{II} defect reorients by capturing an electron and subsequently reorienting in the negative charge state. To further support this interpretation, a much slower reorientation process was observed with a reverse bias applied to the sample. Under these experimental conditions, practically all centres are in the neutral charge state, suggesting that the energy barrier for the reorientation is substantially larger in this case. A similar dependence on charge state has been proposed by Kamiura et al. after the conclusion of the present work [Kamiura 2002].

According to equation (5.3), the reorientation process will be activated by an energy given by the difference between ΔE^- and $E_c - E_t$. Though intuitively difficult to comprehend, this means that the experimentally observed activation energy is smaller than the energy barrier ΔE^- for reorientation in the negative charge state. From

the sum of the effective activation energy (0.582 eV) and the distance between the conduction band and the (C-H)_{II} energy level (0.155 eV), we obtain the energy barrier for reorientation in the negative charge state as $\Delta E^- \approx 0.74$ eV. The energy barrier for reorientation in the neutral charge state is significantly larger.

A similar dependence on charge state has been reported for the dissociation of (C-H)_{II} [Yoneta 1991], [Endrös 1992], [Kamiura 1992], [Kamiura 1997]. That is, the complex becomes unstable in the negative charge state and is stabilized in the neutral charge state. Thus, there exist a certain equivalence between the reorientation and the dissociation of the (C-H)_{II} complex. We can understand this similarity by considering the jump events involved in the two processes. Reorientation takes place by a jump of hydrogen between equivalent sites (bond-center sites or anti-bonding sites) around substitutional carbon, while dissociation takes places by a jump of hydrogen between first and second nearest neighbor sites to the carbon atom. The nature of these jump processes are essentially similar. We conclude that the reorientation of hydrogen around substitutional carbon can be considered a precursor for the diffusion process.

5.4.5 Comparison to isolated atomic hydrogen

Finally, let us compare the electronic properties of the hydrogen-carbon pair to those of isolated atomic hydrogen. Figure 5.9 shows the band gap positions of donor/acceptor levels related to isolated atomic hydrogen, carbon-perturbed bond-centered hydrogen (configuration SiH_{BC}SiC_s) and the hydrogen-carbon pair studied in the present work (configuration SiH_{BC}C_s or configuration SiC_sH_{AB}).

Isolated hydrogen in silicon is a bistable negative-U defect. H⁰ and H⁺ occupy positions close to bond-center sites with a donor level E3' at $E_c - 0.175$ eV [Bonde 1999b], while H⁻ lies near a T-site with an acceptor level close to midgap at approximately $E_c - 0.65$ eV [Bonde 2001]. As described in the background section, it was recently shown that the SiH_{BC}SiC_s structure introduces a donor level (C-H)_I at $E_c - 0.22$ eV, i.e. close to the donor level of isolated bond-centered hydrogen. Thus, the perturbation of bond-centered hydrogen by a nearby substitutional carbon atom does not significantly

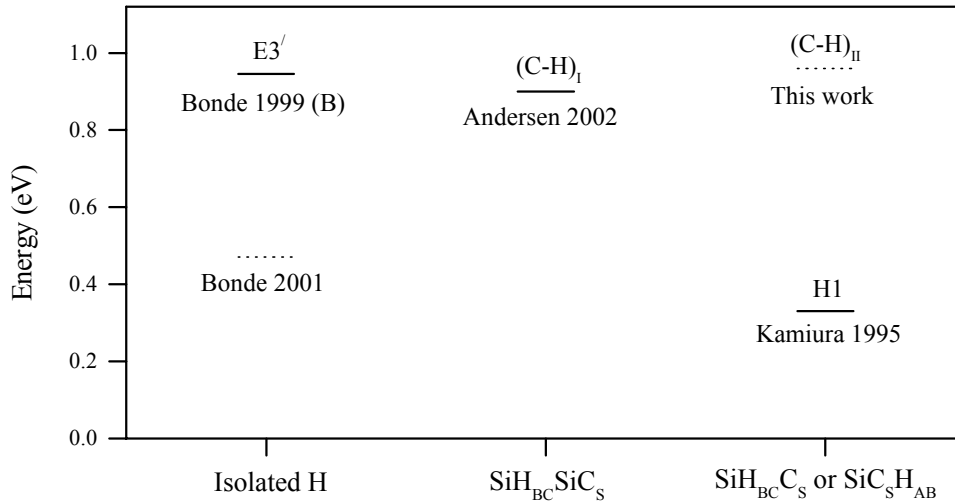


Figure 5.9: Band gap positions of donor/acceptor levels related to isolated hydrogen, configuration $\text{SiH}_{\text{BC}}\text{SiC}_{\text{s}}$ and configuration $\text{SiH}_{\text{BC}}\text{C}_{\text{s}}/\text{SiC}_{\text{s}}\text{H}_{\text{AB}}$ responsible for the $(\text{C-H})_{\text{II}}$ level. Donor and acceptor levels are represented by solid and dotted lines, respectively. Labels and references are given for the individual levels. The zero point of the energy scale has been chosen to equal the energy of the valence band maximum.

alter the electronic properties of the defect. In the present work, we have studied an acceptor level $(\text{C-H})_{\text{II}}$ at $E_c - 0.155$ originating from the bond-center configuration $\text{SiH}_{\text{BC}}\text{C}_{\text{s}}$ or the anti-bonding configuration $\text{SiC}_{\text{s}}\text{H}_{\text{AB}}$. One of these configurations also introduces a donor level labelled H1 at $E_v + 0.33$ eV [Kamiura 1995]. Thus, remarkably, the formation of the $\text{SiH}_{\text{BC}}\text{C}_{\text{s}}/\text{SiC}_{\text{s}}\text{H}_{\text{AB}}$ structure converts the negative-U system of isolated hydrogen to a positive-U defect. We conclude that the interactions of isolated atomic hydrogen with substitutional carbon and resulting formation of the hydrogen-carbon pair profoundly alters the electronic properties of the defect.

5.5 Summary

An electron trap with a level at $E_c - 0.155$ eV observed in etched carbon-rich n-type silicon has been investigated by Laplace DLTS in combination with uniaxial stress. Contrary to previous work, the trap level has been assigned to a deep acceptor. A detailed piezospectroscopic analysis of the defect has been carried out, including measurements

of the strain-energy piezospectroscopic tensor and investigations of the reorientation kinetics. The complex has been identified either as a structure with hydrogen bond-centered next to a substitutional carbon atom or a structure with hydrogen anti-bonded to the carbon atom. The data did not allow us to reliably distinguish between the two structures. The energy barrier for the reorientation of the negatively charged complex was obtained as ~ 0.74 eV, while the barrier is significantly larger in the neutral charge state. It was concluded that the reorientation process acts as a precursor for diffusion.

Chapter 6

Piezospectroscopic analysis of the VO complex in silicon

Silicon crystals grown by the Czochralski method contain an oxygen concentration of $\sim 10^{18} \text{ cm}^{-3}$. The oxygen mainly occupies interstitial lattice sites, forming an electrical inactive defect. After irradiation, the vacancy-oxygen complex (also labelled VO or the A-centre) is formed through trapping of migrating vacancies by interstitial oxygen atoms. The complex is one of the dominant defects in irradiated Cz grown silicon. This chapter describes the results of a detailed piezospectroscopic analysis of the VO complex carried out by uniaxial stress in combination with Laplace DLTS¹.

6.1 Background

A detailed description of the VO complex was given by Watkins and Corbett as early as 1961 in an experimental study combining EPR [Watkins 1961] and infrared absorption [Corbett 1961]. This excellent work established the microscopic structure of the VO complex, depicted in Figure 6.1(a). The oxygen atom forms a strong covalent Si-O-Si

¹This work was a collaborative study between the semiconductor groups at UMIST and the universities in Aarhus, Grenoble and Warsaw. Therefore, some of the experimental data presented below have not been obtained by the author of the present work. It will be clearly stated, when this is the case.

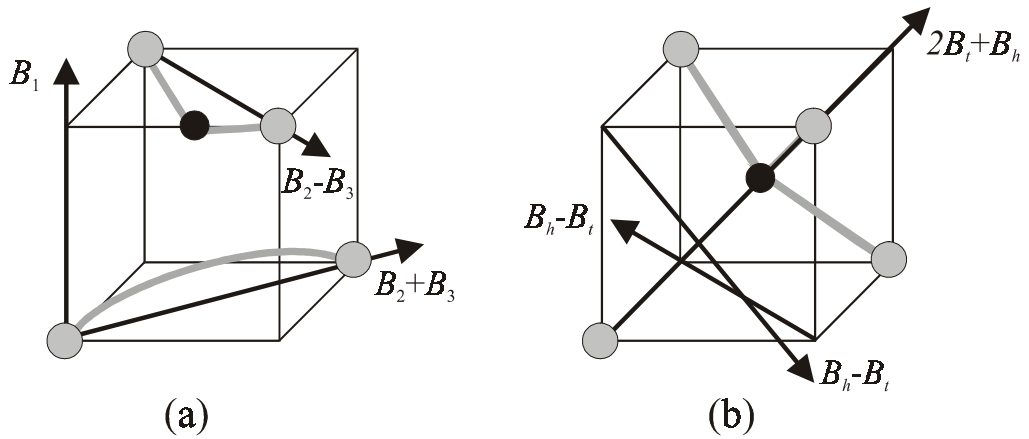


Figure 6.1: Structures of (a) the stable configuration of the VO complex and (b) the trigonal saddle point configuration of the VO complex. Silicon and oxygen atoms are shown as grey and black spheres, respectively. Principal directions and corresponding eigenvalues are indicated.

bond with two of the silicon atoms bordering the vacancy, while the two remaining host atoms form a weak Si-Si bond. This orthorhombic-I C_{2v} symmetry has subsequently been confirmed by theoretical calculations [Coutinho 2000] and uniaxial stress conventional DLTS measurements [Meese 1983], [Qin 1985], [Yao 1987]. In silicon, the VO centre can exist in the negative and neutral charge states (VO^- , VO^0) and introduces a deep acceptor level $VO(-/0)$ into the band gap at $E_c - 0.16$ eV. This level has been analyzed in a number of DLTS studies of irradiated Cz n-type silicon [Evwaraye 1976], [Brotherton 1982]. The interactions of hydrogen with the VO complex is considered in Chapter 7.

A detailed piezospectroscopic analysis of the stable VO complex has been carried out by EPR in combination with uniaxial stress [Watkins 1961]. Piezospectroscopic parameters were obtained by measuring the equilibrium occupancy ratios of non-equivalent orientations under an uniaxial stress. The results will be given later in the thesis and directly compared to the results obtained in the present work. Preferential alignment of the VO complex has also been observed by conventional DLTS [Meese 1983], [Qin 1985] but no detailed studies have been reported.

The zero-stress energy barrier for the reorientation of the neutrally charged centre

has been determined experimentally as 0.38 eV by EPR [Watkins 1961] and 0.37 eV by conventional DLTS [Meese 1983]. This barrier has also been calculated and found to equal 0.47 eV [DeLeo 1984], 0.5 eV [Chadi 1996], 0.3 eV [Pesola 1999], and 0.26 eV [Coutinho 2000]. However, little is known about the structure of the saddle point on the reconfiguration trajectory. No experimental studies are reported and the calculations carried out by different theoretical groups are not conclusive. DeLeo et al. concluded that saddle point for oxygen reconfiguration is in the $\langle 110 \rangle$ direction from the substitutional site [DeLeo 1984], while Chadi and Pesola et al. proposed that the saddle point configuration has a trigonal symmetry [Chadi 1996], [Pesola 1999]. Pesola et al. also found that there is an alternative saddle point of cubic T_d symmetry (substitutional position of oxygen). Figure 6.1(b) depicts the trigonal saddle point structure, to be discussed in more detail later in the chapter.

6.2 Sample preparation

Samples were prepared from (110) oriented Cz n-type silicon of resistivity 20 Ω -cm. The material was cut into $\sim 7 \times 2 \times 1$ mm bars with the long dimension parallel to one of the major crystallographic directions, $\langle 100 \rangle$, $\langle 110 \rangle$ and $\langle 111 \rangle$. The samples were either implanted with protons of energy 350-600 keV to a dose of $\sim 1 \times 10^{10}$ cm $^{-2}$ or irradiated with electrons of energy 2 MeV to a dose of $\sim 6 \times 10^{13}$ cm $^{-2}$. Implantations and irradiations were carried out by Knud Bonde Nielsen at University of Aarhus, Denmark. Schottky diodes and Ohmic contacts were formed by evaporation of gold and aluminum, respectively.

6.3 Experimental results

Figure 6.2 shows the 88 K Laplace DLTS spectra of the acceptor level of the VO complex obtained at zero stress and under 0.20 GPa uniaxial stress along the three major crystallographic directions, $\langle 100 \rangle$, $\langle 110 \rangle$ and $\langle 111 \rangle$. For each direction of stress, the zero-stress peak splits into two well-resolved components. The amplitudes

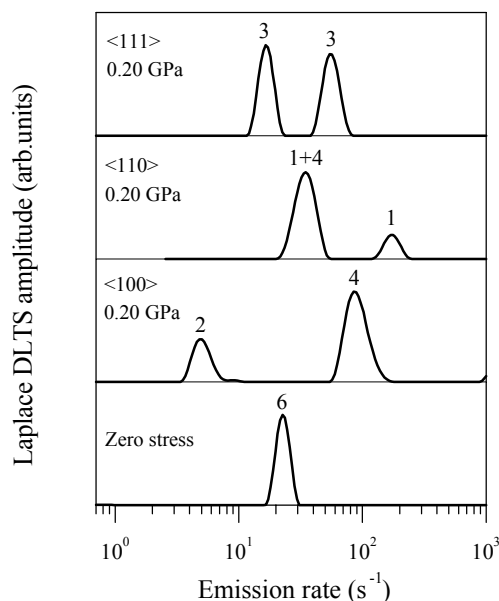


Figure 6.2: 88 K Laplace DLTS spectra of VO ($-/0$) obtained at zero stress and under 0.20 GPa stress along the three major crystallographic directions, $\langle 100 \rangle$, $\langle 110 \rangle$ and $\langle 111 \rangle$. The splitting pattern establishes the orthorhombic-I symmetry of the VO complex.

of the split lines sum up to the amplitude of the zero-stress peak, normalized to a value of 6 units. Within experimental error, the relative amplitudes of the individual peaks in Figure 6.2 agree with the ratios expected for an orthorhombic-I centre, i.e. $2 : 4$ for the $\langle 100 \rangle$ stress direction, $(1 + 4) : 1$ for the $\langle 110 \rangle$ stress direction and $3 : 3$ for the $\langle 111 \rangle$ stress direction (Table 2.2). The peak at lower emission rate for the $\langle 110 \rangle$ direction is unresolved. Thus, the splitting pattern confirms the orthorhombic-I C_{2v} symmetry of the VO complex.

A similar splitting pattern has been observed also with the use of conventional DLTS combined with uniaxial stress [Meese 1983], [Qin 1985], [Yao 1987]. In our experience, however, the use of this technique leads to serious difficulties in the data interpretation due to the fact that the VO complex reorients at temperatures only slightly higher than the DLTS measurement temperatures (see below). This means that, during the temperature scanning, the amplitude of the high-temperature component is affected by the defect reorientation process, leading to possible mis-interpretation of the data.

6.3.1 Influence of stress on the emission and capture processes

A detailed analysis of the electronic properties of the VO complex at zero stress is given in Chapter 7. The zero-stress activation enthalpy for the VO ($-/0$) level was obtained as 153 meV (Table 7.1). We have studied the influence of uniaxial stress on the ionization process $\text{VO}^- \rightarrow \text{VO}^0 + e_c$ for the various non-equivalent orientations. The emission rates of the split lines were monitored at a number of stresses at 85 K for the $\langle 100 \rangle$ stress direction and at 88 K for the $\langle 110 \rangle$ and $\langle 111 \rangle$ stress directions. Figure 6.3 shows the energy shifts $k_B T \ln \left(\frac{e_n(P)}{e_n(0)} \right)$ versus stress for the individual lines presented in Figure 6.2. The shifts are linear in stress for the $\langle 110 \rangle$ and $\langle 111 \rangle$ stress directions. We obtain the stress coefficients as 12 meV/GPa and 99 meV/GPa for the $\langle 110 \rangle$ stress direction and -19 meV/GPa and 47 meV/GPa for the $\langle 111 \rangle$ stress direction. This gives energy splittings of 87 meV/GPa and 66 meV/GPa, respectively. For the $\langle 100 \rangle$ stress direction, the shift of the low frequency line displays a significant bowing. The non-linearity has been observed at various temperatures between 82 K and 110 K and has been reproduced in a number of samples. The splitting of the low frequency line and the high frequency line is estimated as 56 meV/GPa in the high stress regime. The energy splittings for all directions of stress are displayed in Table 6.1.

In order to address the effect of bowing, we have examined the stress dependence of the capture process for the low frequency branch in the $\langle 100 \rangle$ stress direction. The capture measurements were carried out at 85 K by using the filling pulse method in combination with Laplace DLTS. Unfortunately, it was not possible to examine the capture process reliably at zero stress under the given experimental conditions. The VO complex forms a very effective centre for capture of electrons, hence a study of the capture process requires either a large reduction of the fill pulse width² or the use of lowly doped material. Below, we use the value of the zero-stress electron capture cross section obtained from the data presented in Chapter 7, where material of higher

²The experimental set-up used for this work allows a minimum fill pulse width of ~ 50 ns.

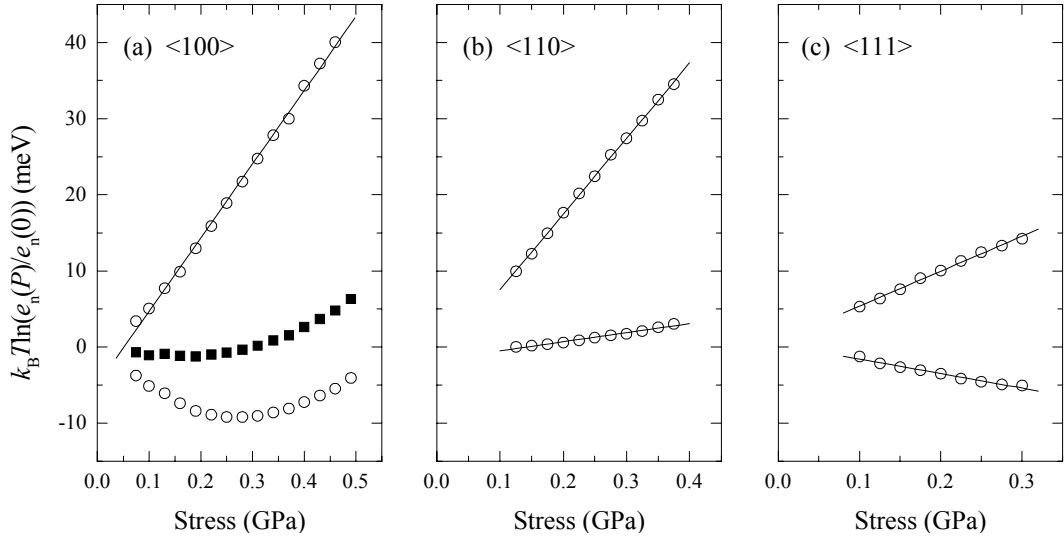


Figure 6.3: Energy shifts $k_B T \ln\left(\frac{e_n(P)}{e_n(0)}\right)$ versus applied stress for the non-equivalent orientations of the VO complex for stress along (a) the $\langle 100 \rangle$ direction, (b) the $\langle 110 \rangle$ direction and (c) the $\langle 111 \rangle$ direction. Solid symbols in (a) show the emission data corrected by the capture data for the low frequency line. The emission data for the $\langle 100 \rangle$ stress direction have been measured by Laurent Rubaldo.

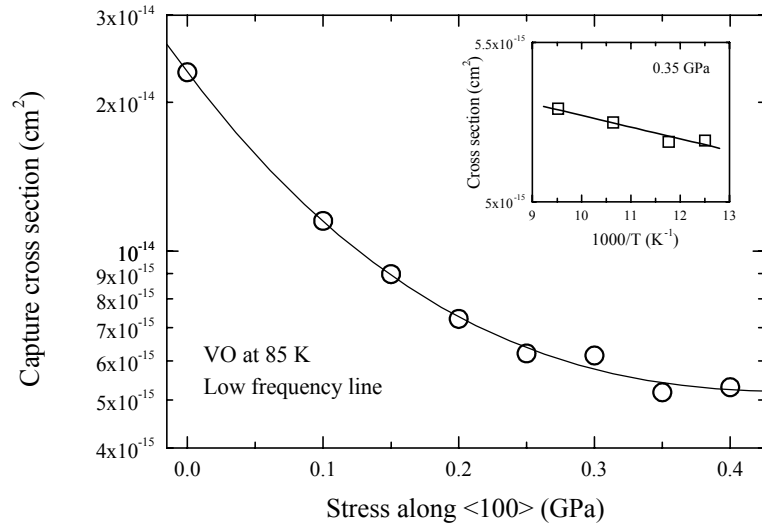


Figure 6.4: Electron capture cross section at 85 K versus stress for the low frequency branch in the $\langle 100 \rangle$ stress direction. The zero-stress value has been obtained from the data presented in Chapter 7. Inset shows an Arrhenius plot for the cross section measured at 0.35 GPa.

resistivity was used ($\sigma_n = 2.4 \times 10^{-14} \text{ cm}^2$). The capture data for the low frequency branch obtained at stresses 0.1-0.4 GPa were well described by purely exponential refilling kinetics in the range 50-250 ns. Figure 6.4 depicts the value of electron capture cross section as a function of stress. The data demonstrate that the capture kinetics are significantly slowed down by the stress. The dependence is rather strong at lower stresses but eventually levels off. A similar dependence has been reported previously for this particular branch [Yao 1987]. The inset in Figure 6.4 shows an Arrhenius plot for the electron capture cross section of the low frequency branch measured at 0.35 GPa. The temperature dependence of the cross section is extremely weak and within experimental error. Capture measurement carried out at 88 K for the two lines in the $\langle 111 \rangle$ stress direction showed no measurable influence of the applied stress on the electron capture process.

The magnitude of the capture cross section is involved in the relation between the carrier emission rate and the ionization energy as a pre-exponential factor (equation (2.24)). Hence, the stress dependence of the capture process offers a possible explanation for the non-linearity of the emission data. Figure 6.3(a) (solid symbols) shows the “corrected” shift $k_B T \ln \left(\frac{e_n(P)}{e_n(0)} / \frac{\sigma_n(P)}{\sigma_n(0)} \right)$ of the ionization energy with stress for the low frequency line in the $\langle 100 \rangle$ stress direction, where $\frac{\sigma_n(P)}{\sigma_n(0)}$ has been obtained from the fit to the data in Figure 6.4 (solid line). The stress-dependence of the capture process goes some way towards explaining the effect of bowing though the corrected data still depart from linearity. This may be related to a significant uncertainty of the capture data, which were obtained under far from ideal experimental conditions. Further, equation (2.24) may be too simplistic if the nature of the capture process is modified by the stress. To conclude, the results indicate that the bowing of the low frequency branch in the $\langle 100 \rangle$ stress direction is caused by the stress dependence of the capture process. A complete picture requires more detailed stress capture measurements and a more detailed analysis.

6.3.2 Stress-induced alignment

Stress-induced alignment experiments of the two charge states of the VO complex have been carried out for all directions of stress. The equilibrium distributions between the non-equivalent orientations have been reached by applying the stress at a relatively high temperature of 145 K for approximately 15 minutes. Subsequently, the sample was cooled quickly to the measurement temperature (85-90 K) and the occupancy ratio of defects in non-equivalent orientations was evaluated from the amplitudes of the corresponding Laplace DLTS peaks. It was directly checked that the steady-state condition was reached. The charge state of the VO centres during alignment was controlled by the bias applied to the sample, i.e. the complexes were in the neutral state when the reverse bias was on and in the negative state when the bias was off. During the cool-down of the sample, the bias was off. This was found to slow down the reorientation process (see below), hence partially preventing further reorientation during cooling.

For stress along the $\langle 100 \rangle$ direction, complete alignment in the neutral and the negative charge states changes the 2 : 4 splitting in Figure 6.2 to a 0 : 6 splitting. Figure 6.6(a) shows the 145 K equilibrium amplitude ratio of the low frequency and high frequency lines versus applied stress for VO^0 and VO^- . The experimental data are well described by Boltzmann statistics, equation (2.31). We obtain the alignment stress coefficients as 151 meV/GPa for the neutral charge state and 120 meV/GPa for the negative charge state.

For the $\langle 110 \rangle$ stress direction, alignment in the neutral charge state changes the 1 : 4 : 1 splitting (seen as 5 : 1) in Figure 6.2 to a 3 : 0 : 3 splitting (seen as 3 : 3). Figure 6.5 shows Laplace DLTS spectra obtained before and after alignment in the $\langle 110 \rangle$ stress direction. The 3 : 3 splitting observed after alignment shows that the two configurations of degeneracy 1 are equal in total energy. Figure 6.6(b) depicts the 145 K equilibrium amplitude ratio of the low frequency and high frequency lines as a function of applied stress for VO^0 . The experimental data are well described by

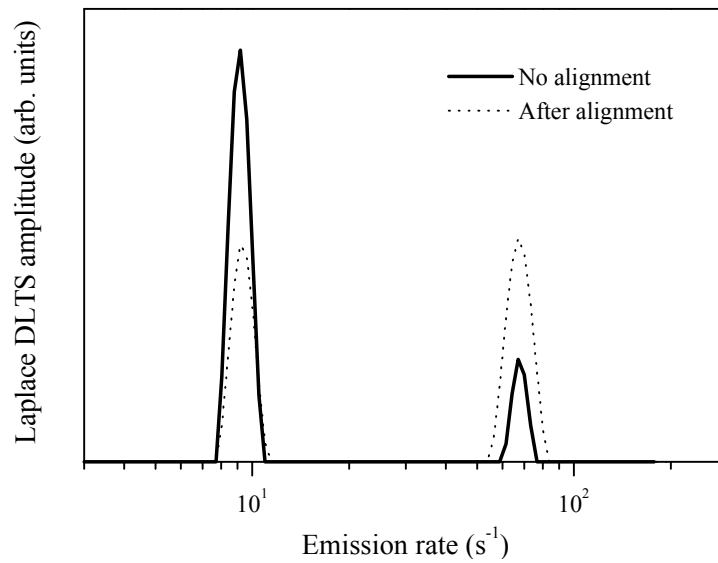


Figure 6.5: Laplace DLTS spectra of VO ($-/0$) obtained at 85 K under 0.15 GPa stress along the $\langle 110 \rangle$ directions before and after alignment of the neutrally charged defect.

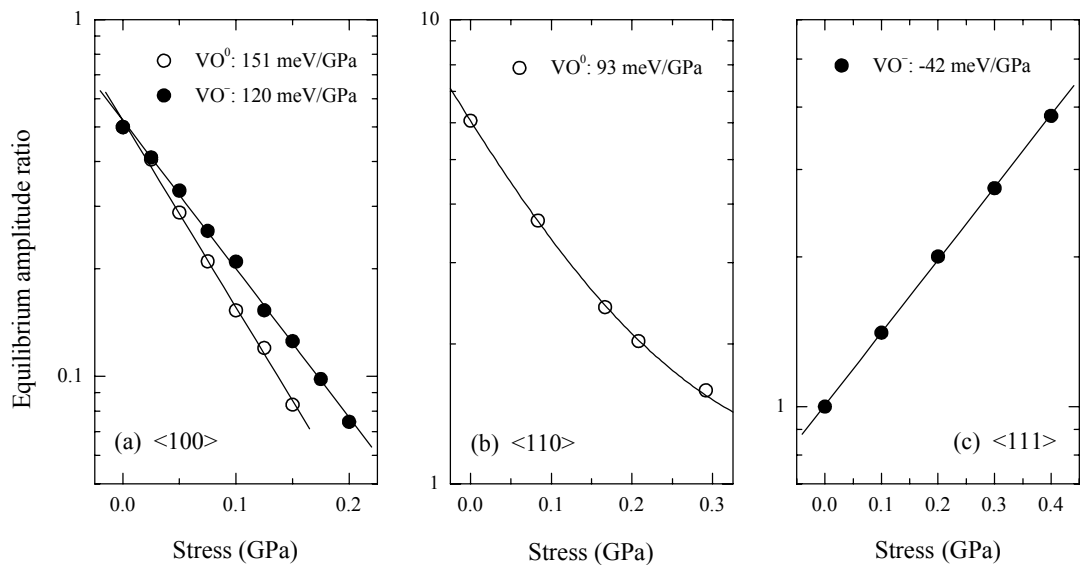


Figure 6.6: Equilibrium amplitude ratio at 145 K for the low frequency and high frequency lines of the VO complex for (a) the $\langle 100 \rangle$ stress direction, (b) the $\langle 110 \rangle$ stress direction and (c) the $\langle 111 \rangle$ stress direction.

| Stress direction | Splitting, VO (-/0) | Alignment, VO ⁰ | Alignment, VO ⁻ |
|------------------|---------------------|----------------------------|----------------------------|
| <100> | 56 | 151 | 120 |
| <110> | 87 | 93 | 0 |
| <111> | 66 | 0 | -42 |

Table 6.1: Splitting and alignment data for the VO complex. The splitting for the <100> stress direction has been obtained in the high-stress regime. All values are given in meV/GPa.

Boltzmann statistics with the alignment stress coefficient 93 meV/GPa. No effect of alignment was observed for the negatively charged complex.

For the <111> stress direction, no alignment was observed in the neutral charge state. In the negative charge state, complete alignment changes the 3 : 3 splitting in Figure 6.2 to a 6 : 0 splitting. Figure 6.6(c) shows the equilibrium occupancy ratio of the low frequency and high frequency lines as a function of applied stress for VO⁻. We obtain the alignment stress coefficient as -42 meV/GPa. The alignment data for all directions of stress and both charge states are displayed in Table 6.1.

6.3.3 Influence of stress on the reorientation barriers

The influence of stress on the defect reorientation barrier has been studied for the <100> and <110> stress directions. For this purpose, the stress-induced alignment process was carried out in a sequence of isothermal annealing steps with a duration of typically 10-15 minutes each. After each step, the sample was cooled quickly to the measurement temperature (85-90 K) and the occupancies of defects in non-equivalent orientations were evaluated from the amplitudes of the corresponding Laplace DLTS peaks. This approach enabled us to observe the kinetics of the reorientation process at the given stress. The charge state of the complex during alignment was controlled by the bias applied to the sample.

Figure 6.7 illustrates the reorientation kinetics at 132 K of the negatively charged complex for the <100> stress direction. The graph shows the decay of the amplitude of the low frequency line as a function of annealing time for several stresses. The

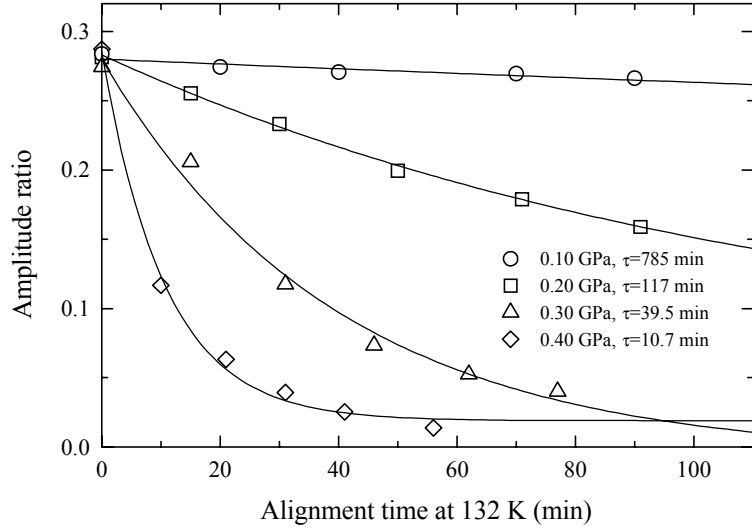


Figure 6.7: Reorientation kinetics at 132 K of the negatively charged complex VO^- for the $\langle 100 \rangle$ stress direction. The graph shows the amplitude of the low frequency line relative to the sum of the two lines as a function of annealing time for several stresses.

data demonstrate that the stress speeds up the reorientation process, i.e. the effective reorientation barrier for VO^- is decreased by a stress along the $\langle 100 \rangle$ direction. We obtain the barrier stress coefficient as -149 meV/GPa . A similar approach gave a barrier stress coefficient of -84 meV/GPa for the neutrally charged complex VO^0 . In contrast to the $\langle 100 \rangle$ direction, a stress along the $\langle 110 \rangle$ direction is found to increase the reorientation barrier with a stress coefficient of $+100 \text{ meV/GPa}$ for VO^0 . This value relates to the transformation from the 5 : 1 splitting observed before alignment to the 3 : 3 splitting observed after alignment (Figure 6.5). The zero-stress reorientation barriers were obtained by studying the kinetics of the mis-alignment process at a number of temperatures. The procedure was similar to the approach used for the hydrogen-carbon pair in Chapter 5. Arrhenius plots for the zero-stress reorientation processes gave an effective energy barrier of 388 meV and a pre-exponential factor of $2 \times 10^{13} \text{ s}^{-1}$ for the neutrally charged complex and an effective energy barrier of 512 meV and a pre-exponential factor of $7 \times 10^{14} \text{ s}^{-1}$ for the negatively charged complex. The zero-stress barriers for VO^0 and VO^- and the stress coefficient for the barrier in the $\langle 110 \rangle$ stress direction for VO^0 were obtained from measurements carried out by Laurent Rubaldo

and Leszek Dobaczewski.

6.4 Discussion

6.4.1 Piezospectroscopic parameters for the stable VO configuration

The well-established structure of the stable VO complex depicted in Figure 6.1(a) has the orthorhombic-I C_{2v} symmetry. Thus, the defect has two non-equivalent orientations labelled $1A$, $1B$ of degeneracy 2 and 4 for stress along the $\langle 100 \rangle$ direction, three non-equivalent orientations labelled $2A$, $2B$, $2C$ of degeneracy 1, 4, and 1 for stress along the $\langle 110 \rangle$ direction and two non-equivalent orientations labelled $3A$, $3B$ of degeneracy 3 and 3 for stress along the $\langle 111 \rangle$ direction (Table 2.2). The principal axes of the complex are $[001]$, $[1\bar{1}0]$ and $[110]$ with corresponding eigenvalues B_1 , $B_2 - B_3$ and $B_2 + B_3$, respectively, where B_1 , B_2 and B_3 are defined as in Table 2.1. Thus, $B_2 - B_3$ measures the change in total defect energy per unit strain along the axis of the two silicon atoms in the Si-O-Si unit, while $B_2 + B_3$ measures the change in total defect energy per unit strain along the axis of the two silicon atoms in the Si-Si unit (Figure 6.1(a)).

The alignment data allow us to analyze the components of the piezospectroscopic tensor for both charge states. We denote by $\alpha_{A,B}$ the stress coefficient for the total energy difference between configurations A and B . A positive stress coefficient $\alpha_{A,B}$ means that configuration A is higher in total energy than configuration B . Our alignment data gave the values $\alpha_{1A,1B}^0 = 151$ meV/GPa and $\alpha_{3A,3B}^0 = 0$ meV/GPa for the neutral charge state and $\alpha_{1A,1B}^- = 120$ meV/GPa and $\alpha_{3A,3B}^- = -42$ meV/GPa for the negative charge state (Table 6.1). The stress coefficients are related to the piezospectroscopic tensor components by the expressions $\alpha_{1A,1B} = (B_2 - B_1)(s_{11} - s_{12})$ and $\alpha_{3A,3B} = \frac{2}{3}B_3s_{44}$ (Table 2.2). From a simple analysis, we obtain $(B_2^0 - B_3^0) - (B_2^0 + B_3^0) = 0$ eV and $(B_2^0 - B_3^0) - B_1^0 = 15.4$ eV for the neutrally charged defect VO^0 and $(B_2^- - B_3^-) - (B_2^- + B_3^-) = 10.0$ eV and $(B_2^- - B_3^-) - B_1^- = 17.2$ eV for the negatively charged defect VO^- . A positive tensor component shows that the total energy

| | Laplace DLTS | EPR | Theory |
|-----------------|--------------|----------------|-----------------|
| | This work | [Watkins 1961] | [Coutinho 2000] |
| B_1^0 | -10.2 | -11.1 | -9.8 |
| $B_2^0 - B_3^0$ | 5.1 | 6.1 | 5.5 |
| $B_2^0 + B_3^0$ | 5.1 | 4.9 | 4.5 |
| B_1^- | -8.1 | -8.4 | -6.8 |
| $B_2^- - B_3^-$ | 9.0 | 8.8 | 7.8 |
| $B_2^- + B_3^-$ | -0.9 | -0.4 | -0.6 |

Table 6.2: Piezospectroscopic tensor components for both charge states of the VO complex. Our Laplace DLTS results are compared to data obtained by EPR and theoretical modeling. All values are given in eV.

of the defect is decreased by a compressive stress applied along the corresponding principal axis. We conclude that the total energy of the VO complex is lowered almost equally by compression along the Si-O-Si unit and compression along the Si-Si unit in the neutral charge state, while the energy lowering is stronger for compression along the Si-O-Si unit in the negative charge state. Thus, there is a strong inward relaxation of the two silicon atoms in the Si-Si unit for the neutrally charged complex.

In order to directly compare our results to literature data, we further apply the assumption of a traceless piezospectroscopic tensor, i.e. $B_1 + 2B_2 = 0$. This additional constraint allows us to calculate the eigenvalues B_1 , $B_2 - B_3$ and $B_2 + B_3$ of the piezospectroscopic tensor for both charge states of the VO complex. The results are displayed in Table 6.2 and compared to data from EPR [Watkins 1961] and theoretical modeling [Coutinho 2000]. There is a remarkable agreement between the three sets of data for both charge states. The present study of the VO complex is the first ever determination of a defect piezospectroscopic tensor by means of DLTS. The excellent agreement with the EPR results has given us a tremendous belief and confidence in our technique and experimental approach. In many ways, the initial work on the VO complex has formed a role model for the study of other defect systems by means of

uniaxial stress Laplace DLTS, some of which are presented in this thesis.

6.4.2 Stress dependence of the emission and capture processes

The stress-induced shifts of the Laplace DLTS peaks reflect the influence of stress on the ionization process $\text{VO}^- \rightarrow \text{VO}^0 + e_c$. Hence, it is expected that the energy splitting of the high and low frequency branches equals the difference $\alpha_{A,B}^0 - \alpha_{A,B}^-$ between the stress coefficients for the neutral and negative charge states obtained from alignment experiments. The experimental results displayed in Table 6.1 show that there is a satisfactory agreement between alignment and splitting data for the $\langle 110 \rangle$ and $\langle 111 \rangle$ stress directions. For the $\langle 100 \rangle$ stress direction, a significant non-linearity of the emission data was observed for the low frequency branch (Figure 6.3(a)). Thus, there is a lack of correspondence with the alignment data, which are linear for both of the two charge states. We have argued that the bowing of the low frequency branch can be explained by the stress dependence of the capture process. The splitting of the low frequency and high frequency branches in the high stress regime is in reasonable agreement with the alignment data (Table 6.1). We conclude that the splitting and alignment data are fully consistent, when the stress dependence of the capture process is taken into account.

It is a remarkable conclusion that the kinetics of the capture process are strongly modified by the application of a stress. The piezospectroscopic parameters obtained for the VO complex allowed us to conclude that significant lattice relaxations are associated with the emission and capture processes. That is, the two silicon atoms in the Si-Si unit of the defect relax inward after electron emission and outwards after electron capture. This complies with observations of a substantial decrease in defect volume upon electron emission [Samara 1986]. We propose that the stress dependence of the capture kinetics is related to a stress-induced modification of the lattice relaxations associated with the emission process. It is possible that such modifications can influence the subsequent capture process. The low-frequency branch, which displays the capture stress dependence, corresponds to the stress applied along the [001] direction for the

structure shown in Figure 6.1(a). For this direction of stress, the silicon lattice experiences considerable tensile strain along the [110] direction, i.e. along the direction for which the lattice relaxations occur. This possibly explains why the stress dependence of the capture process is observed for the low frequency branch in the $\langle 100 \rangle$ stress direction. More detailed capture measurements under stress are currently planned in order to pursue these preliminary ideas.

6.4.3 Charge state dependent reorientation

The energy barrier for the reorientation process is given by the energy difference between the stable defect configuration and the saddle point on the reorientation trajectory. For the neutrally charged complex VO^0 , we found a zero-stress reorientation barrier of 388 meV in excellent agreement with previous results obtained by means of EPR (0.38 eV [Watkins 1961]) and conventional DLTS (0.37 eV [Meese 1983]). For the negatively charged complex VO^- , two possible scenarios can take place for the reorientation process. The defect can either reorient in the negative charge state, or it can get ionized then reorient in the neutral charge state and finally capture an electron. Our experimental results suggest the latter of these possibilities. During the reorientation process, the occupancy of VO defects in the neutral charge state is given by:

$$\frac{N_t^0}{N_t} = 1 - f_{FD}(E_t) = \frac{\exp\left(\frac{E_t - E_F}{k_B T}\right)}{1 + \exp\left(\frac{E_t - E_F}{k_B T}\right)}, \quad (6.1)$$

where $f_{FD}(E)$ is the Fermi-Dirac distribution function and E_t is the VO ($-/0$) energy level. Assuming $E_F - E_t \gg k_B T$, equation (6.1) reduces to:

$$\frac{N_t^0}{N_t} \approx \exp\left(\frac{E_t - E_F}{k_B T}\right) = \frac{N_c}{n_c} \exp\left(-\frac{E_c - E_t}{k_B T}\right). \quad (6.2)$$

If the reorientation of the VO defect only takes place in the neutral charge state, the effective Arrhenius expression for the reorientation process is given by:

$$1/\tau = \frac{N_c}{n_c} R_0^0 \exp\left(-\frac{\Delta E^0 + (E_c - E_t)}{k_B T}\right), \quad (6.3)$$

where ΔE^0 and R_0^0 are the energy barrier and the pre-exponential factor for the reorientation in the neutral charge state, respectively. Thus, the process will be activated

by an energy being the sum of the energy barrier for the reorientation of VO^0 (388 meV at zero stress) and the distance between the conduction band and the $\text{VO}(-/0)$ energy level (153 meV at zero stress). The effective activation energy for the reorientation of VO^- observed experimentally (512 meV) is close to the sum of these two contributions. The effective pre-exponential factor will be by a factor of $\frac{N_c}{n_c}$ ($\sim 4 \times 10^4$ under the given experimental conditions) larger than the pre-exponential for VO^0 ($2 \times 10^{13} \text{ s}^{-1}$). Indeed, a rather large effective pre-exponential factor of $7 \times 10^{14} \text{ s}^{-1}$ was observed for VO^- . The smaller than predicted values of the effective activation energy and pre-exponential factor can be explained by the departure from the assumption $E_F - E_t \gg k_B T$. To further support our interpretation, the stress coefficient of the effective energy barrier for VO^- in the $\langle 100 \rangle$ direction (-149 meV/GPa) is in reasonable agreement with the sum of the corresponding stress coefficient for VO^0 (-84 meV/GPa) and the shift of the distance between the conduction band and the $\text{VO}(-/0)$ energy level (approximately -40 meV/GPa). Thus, our results suggest that it is energetically favorable for the defect to reorient through the neutral charge state. We conclude that the energy barrier for the reorientation of the negatively charged complex is larger than $\sim 0.51 \text{ eV}$.

6.4.4 The saddle point configuration

We have concluded that the structure of the saddle point on the reconfiguration trajectory has a trigonal symmetry. A careful analysis of the experimental data has allowed us to rule out the previously suggested possibilities of orthorhombic and cubic symmetries. In contrast, as shown below, the data are in excellent agreement with a trigonal configuration. The key to this conclusion lies in the decrease of the reorientation barrier with stress for the $\langle 100 \rangle$ stress direction and the increase of the reorientation barrier with stress for the $\langle 110 \rangle$ stress direction.

Figure 6.1(b) illustrates the trigonal saddle point configuration of the VO complex. The oxygen atom is attached to three nearest neighbor silicon atoms and is located on the trigonal axis of the defect. The piezospectroscopic tensor of the saddle point config-

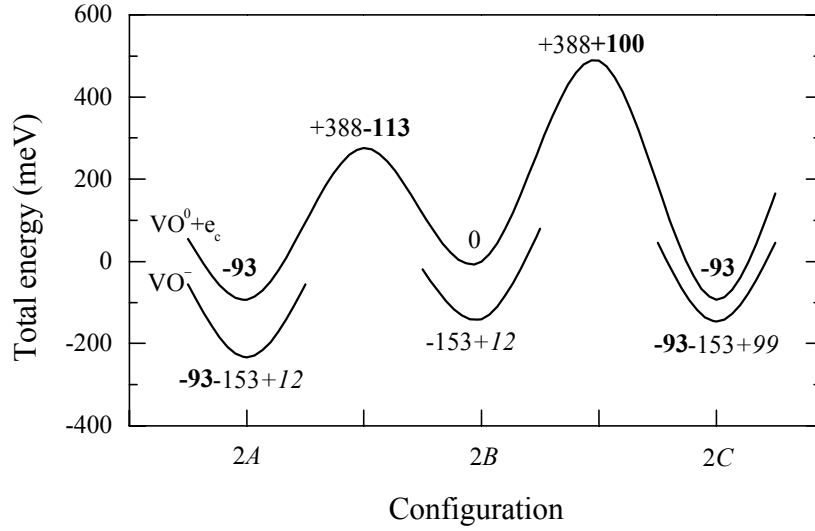


Figure 6.8: Total energy diagrams for the neutral and negative charge states of the VO complex under 1 GPa stress along the $\langle 110 \rangle$ direction. Zero-stress values are given in normal font, stress coefficients for the ionization process are given in italic font and stress coefficients obtained from alignment experiments are given in bold font. The construction of the diagram is specified in the text.

uration contains a hydrostatic (diagonal) component B_h and a trigonal (off-diagonal) component B_t . The principal axes of the complex are $[\bar{1}10]$, $[11\bar{2}]$ and $[111]$ with corresponding eigenvalues $B_h - B_t$, $B_h - B_t$ and $2B_t + B_h$, respectively (Table 2.1).

In Figure 6.8, we document and visualize the trigonal symmetry of the saddle point through the construction of a total energy diagram for the VO complex under 1 GPa stress along the $\langle 110 \rangle$ direction. The non-equivalent configurations $2A$, $2B$, $2C$ for the stable VO complex (degeneracy 1, 4, and 1) each form energy minima separated by reorientation barriers. The trigonal symmetry of the saddle point configuration means that there are two non-equivalent barriers for the $\langle 110 \rangle$ stress direction. The zero points of the energy scale have been chosen to equal the total energy of the neutral complex VO^0 in configuration $2B$. All values displayed in Figure 6.8 are given in respect to this configuration.

From the alignment experiments, we conclude that the total energies of the neutral complex in configurations $2A$ and $2C$ are shifted equally in respect to the reference point ($\alpha_{2B,2A}^0 = \alpha_{2B,2C}^0 = 93$ meV/GPa). The minima for the negative charge states

are shifted downwards in energy by the ionization enthalpy for the given configuration, i.e. the zero-stress value (153 meV) corrected by the stress coefficient for the ionization enthalpy (12 meV/GPa for 2A and 2B, 99 meV/GPa for 2C). Configuration 2C is increased in concentration during alignment and, consequently, we ascribe the measured stress increasing barrier to the one from configuration 2B to 2C. The barrier height is obtained as the zero-stress energy barrier (388 meV) shifted by the stress coefficient for the barrier (+100 meV/GPa). The barrier from configuration 2B to 2A is calculated below. Similar diagrams to the one presented in Figure 6.8 can be constructed for the $\langle 100 \rangle$ and $\langle 111 \rangle$ stress directions.

Let us consider the piezospectroscopic parameters for the saddle point configuration. The total energy of the barrier top for the $\langle 100 \rangle$ direction shifts by the term $-B_h(s_{11} + 2s_{12})$, while the two components for the $\langle 110 \rangle$ stress direction shift by the terms $-B_h(s_{11} + 2s_{12}) \pm \frac{1}{2}B_t s_{44}$ (Table 2.2). The energy shift of a given saddle point structure is determined experimentally as the sum of the energy shift of the stable configuration and the directly measured energy barrier for the reorientation process. Thus, it is not possible to derive the absolute shifts of the top of the barriers independently of the hydrostatic component for the stable configuration. For the purpose of this study, it is assumed that there is no hydrostatic component for the stable configuration, i.e. the piezospectroscopic tensor is traceless ($B_1 + 2B_2 = 0$). Thus, the hydrostatic component ascribed to the saddle point configuration describes the change of the defect volume relative to the stable configuration with oxygen forming the Si-O-Si bridge. From the decrease of the reconfiguration barrier in the $\langle 100 \rangle$ direction (-84 meV/GPa), we obtain the relative hydrostatic component as $B_h^{rel} = -5$ eV. The negative value of the hydrostatic component means that the effective volume of the unit cell is increased when the oxygen atom moves to the saddle point. Subsequently, from the increase of the barrier in the $\langle 110 \rangle$ direction (+100 meV/GPa), we obtain the trigonal component as $B_t = \pm 17$ eV. The evaluation of the piezospectroscopic parameters B_h and B_t allows us to estimate the stress coefficient of the energy barrier for the reorientation from configuration 2B to configuration 2A as -113 meV/GPa (Figure 6.8).

6.5 Summary

We have carried out a detailed piezospectroscopic analysis of the vacancy-oxygen complex in silicon by using Laplace DLTS in combination with uniaxial stress. The piezospectroscopic tensor for the stable configuration was obtained for the neutral and negative charge states by stress-induced alignment experiments. The results were in excellent agreement with EPR data. This is the first ever determination of a piezospectroscopic tensor by DLTS. The reorientation kinetics of the defect allowed us to conclude that the saddle point on the reorientation trajectory has a trigonal symmetry, with the oxygen atom attached to three nearest neighbor silicon atoms. The electron capture cross section was found to depend strongly on the stress for the $\langle 100 \rangle$ stress direction, possibly as a result of a stress-induced modification of the lattice relaxations associated with the emission process. The remarkable feature of a stress-dependent capture process is currently under further investigations.

Chapter 7

Interactions of hydrogen with radiation induced defects

Frenkel pairs of vacancies and self-interstitials are produced by high energy (\sim MeV) irradiation of silicon. In most cases, the vacancies and interstitials annihilate immediately but each can also migrate through the lattice and subsequently interact with impurities, dopants or other vacancies/interstitials to form point defects or clusters [Watkins 1999]. Hydrogen has a well-known ability to interact with radiation induced defects and significantly alter their electronic properties. The aim of this chapter is to study these interactions in electron irradiated n-type and p-type silicon hydrogenated by remote plasma treatment. Our main focus is the passivation of the vacancy-oxygen complex and the divacancy.

7.1 Background

7.1.1 Interactions of hydrogen with the vacancy-oxygen complex

The ability of hydrogen to be trapped at dangling bonds or break Si-Si bonds is well-known. This occurs in numerous vacancy-related complexes since it is energetically favorable to form a Si-H bond at the expense of breaking a weak Si-Si bond [Xu 1992], [Bech 1997], [Stallinga 1998]. The vacancy-oxygen complex, described in

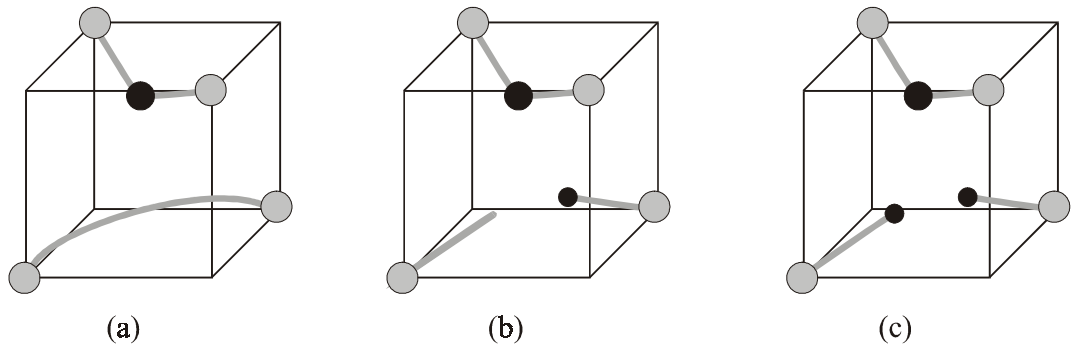


Figure 7.1: Predicted structures of the complexes (a) VO, (b) VOH and (c) VOH₂. Silicon atoms are shown as grey spheres, oxygen and hydrogen atoms as large and small black spheres, respectively.

detail in Chapter 6, is an example of such a vacancy-structure. In this defect, the oxygen atom forms a strong covalent Si-O-Si bond with two of the silicon atoms bordering the vacancy, while the two remaining host atoms form a weak Si-Si bond. Thus, we expect formation of the structures VOH and VOH₂ by attachment of a hydrogen atom to one or both of the two silicon atoms in the Si-Si unit of the defect. Detailed theoretical calculations support this simple model of hydrogen partially or completely saturating the VO defect [Coutinho 2000], [Markevich 2000b]. The predicted structures of the VO, VOH and VOH₂ complexes are illustrated in Figure 7.1.

The VOH complex can exist in the negative, neutral and positive charge states (VOH⁻, VOH⁰, VOH⁺). The neutrally charged centre has been identified in proton implanted Cz silicon by means of EPR [Johannesen 2000]. The complex displays a transition from monoclinic-I C_{1h} symmetry to orthorhombic-I C_{2v} symmetry in the temperature range 180-240 K, arising from the averaging of rapid thermally activated jumps of the hydrogen atom between the two equivalent sites lying in the (110) mirror plane of the defect. The energy barrier for this jump is found to equal 0.18 eV. Calculations of the barrier give 0.18 eV for VOH⁻, 0.11 eV for VOH⁰ [Coutinho 2000] and ~ 0.1 eV for VOH⁺ [Coutinho]. In addition to the hopping of hydrogen, the oxygen atom can also jump between equivalent sites. This barrier is calculated to 0.72 eV for VOH⁻, 0.42 eV for VOH⁰ [Coutinho 2000] and ~ 0.1 eV for VOH⁺ [Coutinho]. A deep level at $E_c - 0.31$ eV observed in numerous DLTS studies of hydrogenated, irra-

diated n-type silicon has been ascribed to the acceptor level of the VOH defect. The arguments for this identification include simultaneous increase of VOH ($-/0$) and decrease of VO ($-/0$) [Tokuda 1998], [Peaker 1999b], correlation with EPR annealing data [Bonde 1999a] and symmetry determination by uniaxial stress Laplace DLTS measurements [Bonde 1999a]. Despite some dispute about this identification [Feklisova 1997], reasonable agreement has now been established [Feklisova 1999]. Recently, it was proposed that a level at $E_v + 0.28$ eV observed in hydrogenated, irradiated p-type silicon forms another charge state of the VOH complex [Feklisova 2001]. This conclusion is supported by earlier observations of similar annealing behavior of the traps with levels located at $E_c - 0.31$ eV and $E_v + 0.28$ eV [Irmscher 1984].

The VOH₂ complex was recently identified by infrared absorption measurements in samples hydrogenated by indiffusion from a H₂ gas at 1200-1300 °C and subsequently irradiated with electrons [Markevich 2000b]. No electrical activity is expected from this fully saturated complex.

7.1.2 Interactions of hydrogen with the divacancy

The silicon divacancy V₂ is formed either directly in a collision cascade during irradiation or as a result of interaction between two migrating monovacancies. The two vacancies in the complex are positioned at adjacent lattice sites [Watkins 1965]. The centre can exist in four charge states (V₂⁻, V₂⁻, V₂⁰, V₂⁺,) and introduces three deep levels, V₂ ($= /-$), V₂ ($-/0$) and V₂ ($+/0$), into the band gap located at $E_c - 0.23$ eV, $E_c - 0.41$ eV and $E_v + 0.20$ eV, respectively [Evwaraye 1976], [Brotherton 1982], [Svensson 1991]. These identifications are fairly well established despite frequently observed intensity differences between the DLTS peaks corresponding to the single and double acceptor levels. Although subject for some debate, it now seems certain that this effect is related to the interference between the single acceptor level and other traps with similar electronic properties [Peaker 2000].

The interactions of hydrogen with the divacancy are poorly known. The divacancy has six dangling bonds and theory predicts up to six V₂H_{*n*} ($n = 1, \dots, 6$) complexes,

presumably all with electrical activity except for the fully saturated V_2H_6 centre. However, only observations of the divacancy binding one hydrogen atom are reported in the literature. The neutrally charged complex V_2H^0 was observed by EPR after low temperature proton implantation followed by heating to room temperature [Stallinga 1998]. Subsequently, the acceptor level of the V_2H complex has been associated with both an electron trap with a level at $E_c - 0.43$ eV observed by Laplace DLTS [Bonde 1999a] and an electron trap with a level at $E_c - 0.45$ eV observed by conventional DLTS [Lévêque 2001]. Despite the close values of the activation energies, the two levels assigned to $V_2H (-/0)$ are not identical.

7.2 Sample preparation

Samples were prepared from three different silicon substrates: (111) oriented FZ n-Si of resistivity 38-50 Ω -cm, (110) oriented Cz n-Si of resistivity 20 Ω -cm and (110) oriented Cz p-Si of resistivity 20 Ω -cm. The two (110) oriented substrates were cut into shapes of $\sim 7 \times 2 \times 1$ mm bars with the long dimension parallel to one of the major crystallographic directions, $\langle 100 \rangle$, $\langle 110 \rangle$ and $\langle 111 \rangle$. The samples were either implanted with protons of energy 350-600 keV to a dose of $\sim 1 \times 10^{10}$ cm^{-2} or irradiated with electrons of energy 2 MeV to a dose of $0.5-10 \times 10^{14}$ cm^{-2} . Implantations and irradiations were carried out by Knud Bonde Nielsen at University of Aarhus, Denmark. The irradiated samples were hydrogenated by remote plasma treatments either at room temperature or at 120 °C, using a gas pressure of ~ 1.0 mbar, treatment times of 20-60 minutes and powers in the range 10-50 W. Details of the plasma system were given in Chapter 4. Schottky diodes and Ohmic contacts were formed on n-Si by evaporation of gold and aluminum, respectively. Schottky diodes and Ohmic contacts were formed on p-Si by sputtering of titanium and evaporation of gold, respectively.

7.3 Overview

Figure 7.2 shows conventional DLTS spectra of as-irradiated and hydrogenated, irradiated FZ n-type silicon and Cz p-type silicon. In the as-irradiated materials (solid curves), the DLTS spectra are dominated by the well-known levels of the pure damage defects introduced by the irradiation. As labelled in Figure 7.2, the dominant peaks are the single acceptor level of the vacancy-oxygen complex, VO ($-/0$), three different charge states of the divacancy, V_2 ($= /-$), V_2 ($-/0$) and V_2 ($+/0$), and the single donor level of the interstitial carbon-oxygen complex, C_iO_i ($+/0$). Hydrogenation by remote plasma treatment causes a significant decrease in the concentrations of these defects as a result of their interactions with hydrogen (dotted curves). The decrease is accompanied by the appearance of three distinct hydrogen-related peaks. Anticipating the identifications made below, we label these peaks VOH ($-/0$) (at ~ 175 K in n-Si), V_2H ($-/0$) (at ~ 275 K in n-Si) and VOH ($+/0$) (at ~ 130 K in p-Si). Further, a broad structure is observed in the high-temperature range in p-Si after hydrogenation. In general, the conventional DLTS spectra in Figure 7.2 are in good agreement with literature data obtained for proton implanted and hydrogenated, irradiated n-type silicon [Irmscher 1984], [Hüppi 1990], [Palmetshofer 1992], [Hallén 1996], [Tokuda 1998], [Feklisova 1999] and p-type silicon [Fatima 1999], [Feklisova 2001].

The high temperature regions of the DLTS spectra in Figure 7.2 contain a number of closely spaced, overlapping peaks for both n-Si and p-Si. Unfortunately, the identities of practically all the hydrogen-related peaks in this mid-gap region remain unknown. This lack of assignments may be related to the very similar electronic properties of the levels, which make it extremely difficult to separate the DLTS peaks and reliably obtain their characteristics. We have explored this difficult mid-gap region by taking advantage of the improved resolution offered by Laplace DLTS.

Figure 7.3 depicts Laplace DLTS spectra of as-irradiated and hydrogenated, irradiated FZ n-Si recorded at 240 K. The spectrum obtained after hydrogenation (middle spectrum) reveals three separated peaks of which the slowest emission component cor-

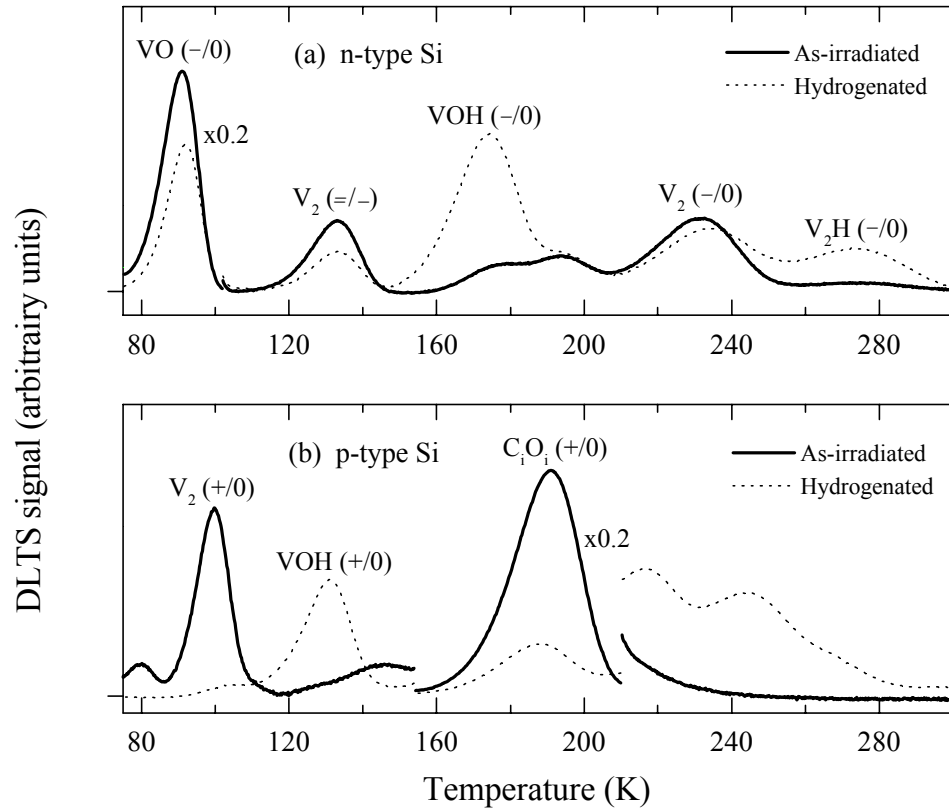


Figure 7.2: (a) 200 s^{-1} conventional DLTS spectra of as-irradiated and irradiated, hydrogenated 38-50 $\Omega\text{-cm}$ FZ n-type Si. (b) 50 s^{-1} conventional DLTS spectra of as-irradiated and irradiated, hydrogenated 20 $\Omega\text{-cm}$ Cz p-type Si. Irradiations were carried out with 2 MeV electrons. Hydrogenations were carried out by exposure to a remote plasma for (a) 20 minutes at room temperature and (b) 60 minutes at 120 $^{\circ}\text{C}$.

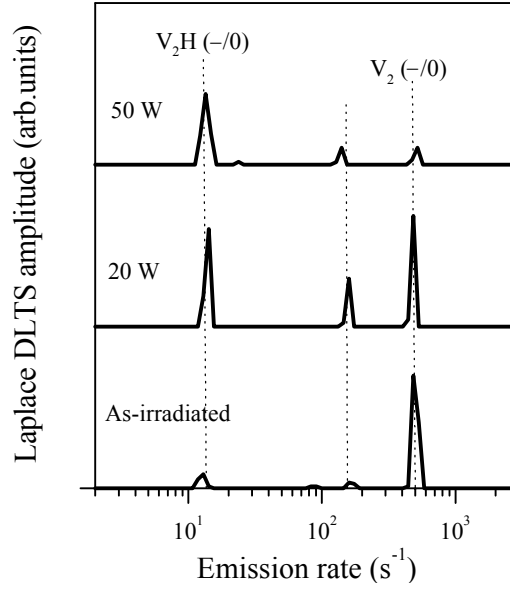


Figure 7.3: 240 K Laplace DLTS spectra of as-irradiated and irradiated, hydrogenated 38-50 Ω -cm FZ n-type Si. Hydrogenations were carried out by 20 minutes room temperature plasma treatments at powers of 20 W and 50 W.

responds to $V_2H (-/0)$ and the fastest emission component corresponds to $V_2 (-/0)$, the peak position of the latter coinciding with the only dominant peak observed in the as-irradiated material. The intermediate peak, only resolved by Laplace DLTS, is related to hydrogen. The appearance of this peak after hydrogenation is consistent with the conventional DLTS spectra in Figure 7.2(a), where the reduction of $V_2 (-/0)$ is less than the reduction of $V_2 (= /-)$ and the peak position of $V_2 (-/0)$ is slightly shifted towards higher temperature by the hydrogenation. The relative positions of the three peaks in Figure 7.3 are in excellent agreement with the dominant peaks observed in a recent Laplace DLTS study carried out on proton implanted n-Si [Bonde 1999a].

Laplace DLTS measurements carried out on hydrogenated, irradiated Cz p-Si in the temperature range 220-280 K were not conclusive. The broad structure seen by conventional DLTS (Figure 7.2(b)) was resolved by Laplace DLTS into at least four separated components. Unfortunately, the computation of the spectra showed some inconsistencies, i.e. in some cases the peak positions were slightly shifted or a small additional component was introduced. Thus, we cannot reliably conclude about the

true splitting pattern.

The results presented above demonstrate the passivation of the pure radiation induced defects and the resulting formation of electrically active hydrogen-related complexes. In addition, it was observed that practically all the hydrogen-related centres themselves can become passivated in regions with high hydrogen concentration. In strongly hydrogenated samples, the overall concentration of electrically active defects was reduced to less than 30% of the as-irradiated value. Thus, our results illustrate the general trend, also discussed in the background section, that hydrogen can be trapped at dangling bonds or break weak Si-Si bonds to form covalent Si-H bonds, hence shifting electronic energy levels within the band gap or completely removing the electrical activity of the original structure. Below, we discuss these transformations in more detail for the VO complex and the divacancy.

7.4 Hydrogen passivation of the VO complex

7.4.1 Electronic properties

Laplace DLTS measurements reveal single emission components of VO ($-/0$), VOH ($-/0$) and VOH ($+/0$). Figure 7.4 shows Arrhenius plots for the majority carrier emissions obtained from series of Laplace DLTS measurements carried out at different temperatures. We determine the activation enthalpies as $\Delta H_n = 0.153$ eV for VO ($-/0$), $\Delta H_n = 0.312$ eV for VOH ($-/0$) and $\Delta H_p = 0.263$ eV for VOH ($+/0$). The results are displayed in Table 7.1. The activation enthalpies are close to the values reported for the levels previously related to VO ($-/0$) [Evwaraye 1976], [Brotherton 1982], VOH ($-/0$) [Bonde 1999a], [Peaker 1999b] and VOH ($+/0$) [Feklisova 2001].

The capture of majority carriers into the levels has been studied by using the filling pulse method in combination with Laplace DLTS at temperatures 90 K for VO ($-/0$), 170 K for VOH ($-/0$) and 135 K for VOH ($+/0$). The data were well described by purely exponential refilling kinetics, equation (3.20). The majority carrier capture cross sections were determined from the capture rates by estimating the concentrations and

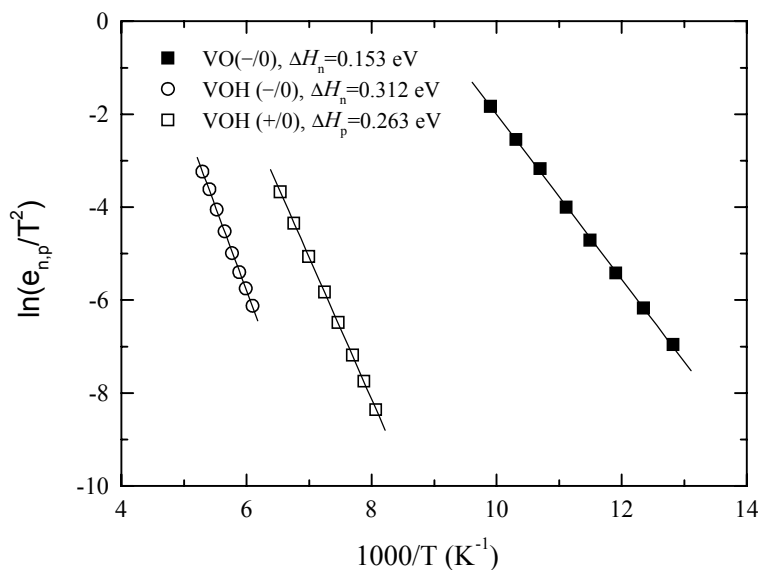


Figure 7.4: Arrhenius plots for the majority carrier emissions from VO (-/0), VOH (-/0) and VOH (+/0).

average thermal velocities of majority carriers under the given experimental conditions. We obtain the electron capture cross sections $\sigma_n = 2 \times 10^{-14} \text{ cm}^2$ for VO (-/0) and $\sigma_n = 1 \times 10^{-15} \text{ cm}^2$ for VOH (-/0) and the hole capture cross section $\sigma_p = 3 \times 10^{-16} \text{ cm}^2$ for VOH (+/0). The results are displayed in Table 7.1. The electronic properties indicate that no strong Coulombic interaction takes place between the carriers and the defect centres, implying capture into neutral defects.

| $\Delta H_{n,p}$ (eV) | $\sigma_{n,p}$ (cm^2) | Identification |
|-----------------------|----------------------------------|------------------|
| 0.153 | 2×10^{-14} (90 K) | VO (-/0) |
| 0.312 | 1×10^{-15} (170 K) | VOH (-/0) |
| 0.263 | 3×10^{-16} (135 K) | VOH (+/0) |
| Passive | | VOH ₂ |

Table 7.1: Activation enthalpies $\Delta H_{n,p}$ for the majority carrier emission processes, directly measured majority carrier capture cross sections $\sigma_{n,p}$ and proposed identifications of the deep levels under study.

7.4.2 Effect of hydrogen on defect concentrations

The conventional DLTS spectra in Figure 7.2 demonstrate that a reduction in the amplitude of the peak related to the VO complex is accompanied by an increase in the amplitudes of the peaks related to the VOH complex. In general, however, the increase of VOH does not account for the corresponding decrease of VO. After strong hydrogenation, the sum-signal of VO and VOH in n-Si is decreased by more than 70% compared to the as-irradiated value. No other levels with expected relation to the VO centre were observed in the DLTS spectra. Thus, the hydrogenation causes an overall loss of electrically active defects related to the VO complex. We propose that this loss is due to the formation of the electrically inert VOH₂ defect.

The above picture is supported by the spatial distributions of the VOH complexes in the hydrogenated materials. For both charge states, the trap profiles show a significant reduction of the defect concentration towards the sample surface, indicating a passivation of the complex by the formation of VOH₂ in regions with high hydrogen concentration.

Finally, passivation of the VO complexes was observed during isothermal annealing at 180 °C of a FZ n-Si sample hydrogenated by plasma treatment at room temperature. Figure 7.5 shows the change in the amplitudes of the DLTS peaks related to VO and VOH relative to the initial amplitude of VO as a function of annealing time. The annealing significantly reduces the concentration of the VO complex, again indicating interactions with hydrogen. Possible sources of hydrogen release include dissociation of hydrogen-phosphorous pairs and diffusion of interstitial hydrogen molecules formed by the plasma treatment. The concentration of the VOH complex is initially increased upon annealing but eventually saturates after ~ 100 minutes. We suggest that a direct transformation from VO to VOH₂ takes place as mobile hydrogen molecules are trapped by the VO defect. In support of this interpretation, the interactions of mobile molecules with the VO complex and subsequent formation of VOH₂ complexes has previously been observed by infrared absorption measurements [Markevich 2000b].

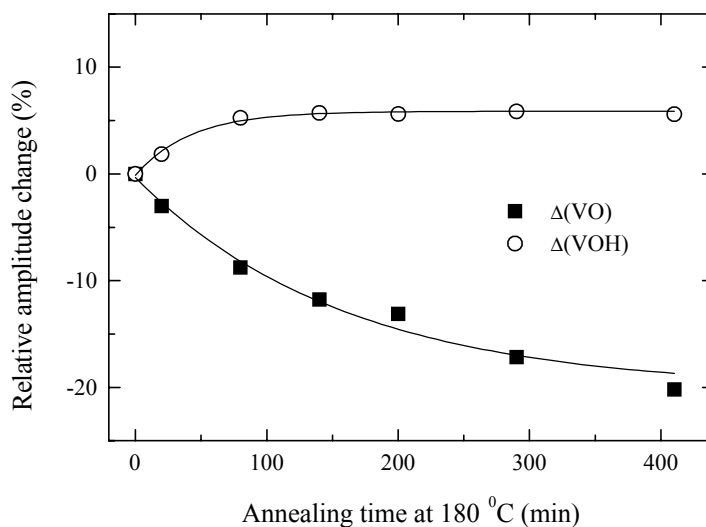


Figure 7.5: Isothermal (180 °C) annealing data of VO ($-/0$) and VOH ($-/0$) obtained in a 38-50 Ω -cm FZ n-Si sample hydrogenated by room temperature remote plasma treatment. The graph shows the change in the amplitudes of VO and VOH relative to the initial amplitude of VO versus annealing time.

7.4.3 Uniaxial stress study of the VOH acceptor level

Figure 7.6 shows Laplace DLTS spectra of VOH ($-/0$) obtained at (a) 155 K under 0.45 GPa stress along the $\langle 100 \rangle$ direction and (b) 165 K under 0.40 GPa stress along the $\langle 111 \rangle$ direction (lowest spectra, solid curves). The spectra recorded at zero stress are also shown (dotted curves). For both directions of stress, the zero-stress peak splits into two well-resolved peaks. Within experimental error, the amplitude ratios of the split peaks agree with those expected for an orthorhombic-I centre, i.e. 2 : 4 for the $\langle 100 \rangle$ stress direction and 3 : 3 for the $\langle 111 \rangle$ stress direction (Table 2.2). The $\langle 110 \rangle$ stress direction displays a very small line splitting but the expected $(4 + 1) : 1$ ratio has been obtained at larger stresses [Bonde 1999a].

The orthorhombic-I symmetry class is consistent with the VOH complex. As discussed in the background section, the hydrogen atom swiftly jumps between equivalent sites in the (110) mirror plane of the defect (Figure 7.1(b)). The hydrogen jump rate is much larger than the rate of the electron ionization process monitored in the Laplace DLTS measurement, by approximately 5 orders of magnitude at the measurement tem-

perature [Johannesen 2000]. Consequently, the static monoclinic-I C_{1h} symmetry is lowered to an effective orthorhombic-I C_{2v} symmetry under the given experimental conditions in agreement with the observed splitting pattern.

Stress-induced alignment experiments of the neutrally charged VOH complex have been carried out for the $\langle 100 \rangle$ and $\langle 111 \rangle$ stress directions. In both cases, a significant effect of alignment was observed at temperatures above 200 K. The equilibrium distribution between the non-equivalent orientations was reached by applying the stress for approximately 15 minutes at 221 K for the $\langle 100 \rangle$ stress direction and at 225 K for the $\langle 111 \rangle$ stress direction. Subsequently, the sample was cooled quickly to the measurement temperature and the occupancy ratio of defects in non-equivalent orientations was evaluated from the amplitudes of the corresponding Laplace DLTS peaks. It was directly checked that the steady-state condition was reached. The VOH complexes were kept in the neutral charge state by applying a reverse bias of -7 V during alignment. No alignment experiments were carried out for the negatively charged complexes.

Figure 7.6 shows Laplace DLTS spectra of VOH ($-/0$) obtained after stress-induced alignment at 0.20 GPa along the $\langle 100 \rangle$ and $\langle 111 \rangle$ stress directions (spectra at top of diagram). The data demonstrate that the amplitude ratio of the low frequency and the high frequency lines is decreased by alignment for the $\langle 100 \rangle$ direction and increased by alignment for the $\langle 111 \rangle$ direction. For both directions of stress, the sum of the amplitudes of the split lines is independent of the alignment stress and equal to the zero-stress amplitude. Figure 7.7 shows the equilibrium amplitude ratio of the low frequency and the high frequency lines versus alignment stress. The data are well described by Boltzmann statistics, equation (2.31). We obtain the stress coefficients $+109$ meV/GPa for the $\langle 100 \rangle$ stress direction and -109 meV/GPa for the $\langle 111 \rangle$ stress direction.

The analysis of the alignment data for VOH⁰ is far from trivial. The effective orthorhombic-I C_{2v} symmetry observed experimentally arises from thermal averaging of the static monoclinic-I C_{1h} symmetry of the defect. In general, however, it is not appropriate to treat the defect as a pure C_{2v} structure in the analysis of the experi-

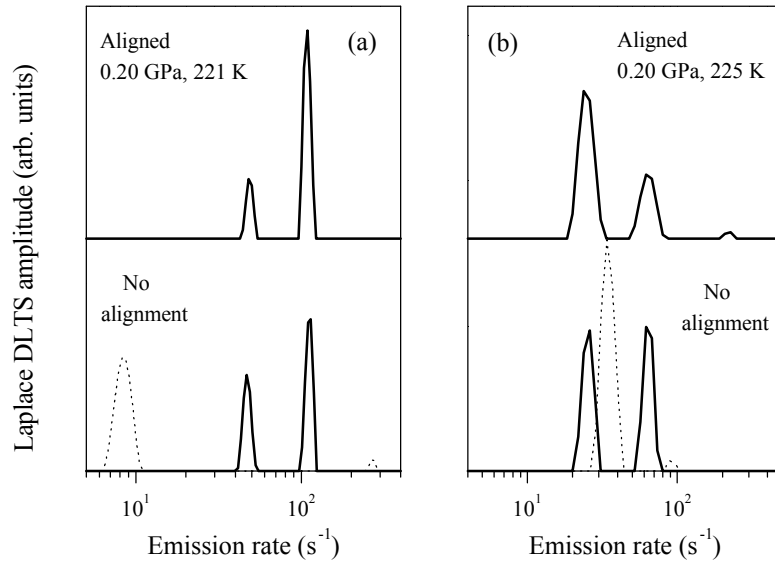


Figure 7.6: Laplace DLTS spectra of VOH ($-/0$) recorded at (a) 155 K under 0.45 GPa stress along the $\langle 100 \rangle$ direction and (b) 165 K under 0.40 GPa stress along the $\langle 111 \rangle$ direction. The spectra have been obtained before and after alignment of the neutral complex. The alignment was carried out at 221 K for the $\langle 100 \rangle$ direction and at 225 K for the $\langle 111 \rangle$ direction with a stress of 0.20 GPa. Dotted curves show spectra recorded at zero stress.

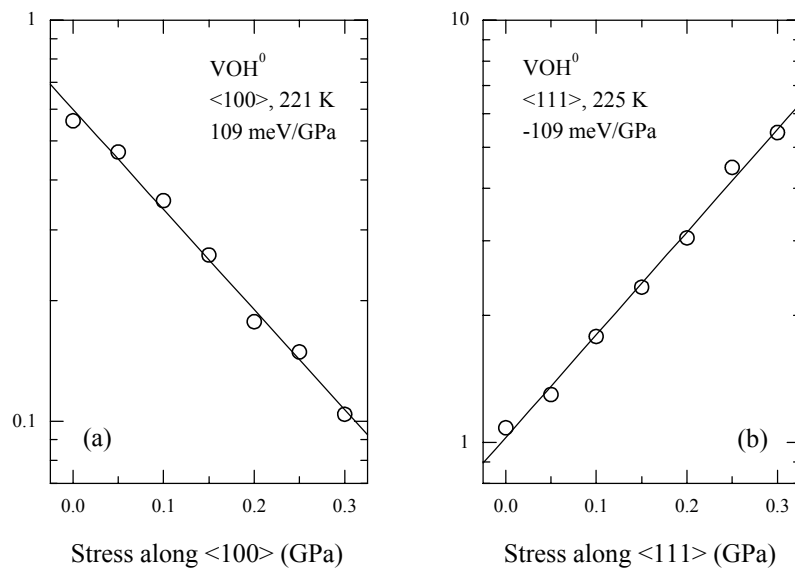


Figure 7.7: Equilibrium amplitude ratio of the low frequency and the high frequency lines versus alignment stress applied to the neutrally charged complexes (a) along the $\langle 100 \rangle$ direction at 221 K and (b) along the $\langle 111 \rangle$ direction at 225 K.

mental data. Consider the $\langle 111 \rangle$ stress direction, where the C_{1h} symmetry has three non-equivalent orientations labelled A , B and B' of degeneracy 6, 3 and 3, respectively. During stress-induced alignment at elevated temperatures, the population of A , B and B' is described by the Boltzmann distribution between all three configurations. During the DLTS experiment, the population of B and B' is described by a Boltzmann distribution, while the population of configuration A is frozen-in. The thermal averaging of B and B' results in a single Boltzmann-averaged level observed experimentally. Thus, the piezospectroscopic analysis of the alignment (and splitting) data for the $\langle 111 \rangle$ stress direction must be carried out by using the C_{1h} symmetry and not the C_{2v} symmetry, which assumes that configurations B and B' are equally populated. This rather complex issue is currently examined in collaboration with the theoretical group in Exeter. For the $\langle 100 \rangle$ stress direction, there are no additional configurations for the C_{1h} symmetry compared to the C_{2v} symmetry, hence it is justified to use the latter symmetry for the analysis. By using this approach, preliminary theoretical calculations of the piezospectroscopic tensor for VOH^0 gave a stress coefficient of +96 meV/GPa for the energy difference between the two non-equivalent configurations in the $\langle 100 \rangle$ stress direction [Coutinho]. This is in good agreement with the experimental value of +109 meV/GPa. Detailed knowledge of the piezospectroscopic properties of the VOH^0 defect can be obtained after analysis of the alignment data for the $\langle 111 \rangle$ stress direction.

7.4.4 Uniaxial stress study of the VOH donor level

The donor level $\text{VOH} (+/0)$ has also been studied by uniaxial stress in combination with Laplace DLTS. The majority of the stress measurements were carried out at a temperature of 135 K. No line splitting was observed for any of the three major crystallographic directions for stresses up to 0.40 GPa for the $\langle 100 \rangle$ direction, 0.50 GPa for the $\langle 110 \rangle$ direction and 0.55 GPa for the $\langle 111 \rangle$ direction. Further, no broadening of the peak was observed even at high stresses. These conclusions were confirmed at temperatures 120 K and 145 K for the $\langle 111 \rangle$ stress direction. For all directions of stress, the level position in the band gap approached the valence band

linearly with the stress. The stress coefficients were obtained as 40 meV/GPa for the $\langle 100 \rangle$ direction, 19 meV/GPa for the $\langle 110 \rangle$ direction and 21 meV/GPa for the $\langle 111 \rangle$ direction.

The lack of splitting indicates that the effective symmetry of the defect is cubic. It seems unlikely that the defect belongs to a lower symmetry class with a line splitting too small to be detected experimentally. The observed cubic symmetry can arise from either (i) a defect with a true, static cubic symmetry or (ii) a defect of lower symmetry which displays an effective cubic symmetry due to thermal averaging at the measurement temperature. The latter of these explanations is consistent with the VOH (+/0) complex. This explanation requires that the reorientation rate of the defect, determined by the jump rates of oxygen and hydrogen, is much larger than the ionization rate at the measurement temperature. There are several indications of rather fast reorientation kinetics for the positively charged VOH complex. The first argument comes from comparison with the VO complex in both silicon and germanium. For these defects, the energy barriers for the reorientation process become systematically larger as more electrons are bound to the defect. In silicon, the reorientation barrier is obtained as 0.388 eV for the neutral charge state, while it is larger than ~ 0.51 eV for the negative charge state (see Chapter 6). In germanium, recent Laplace DLTS uniaxial stress studies indicate that the barrier is significantly larger for the double negative and single negative charge states than for the neutral charge state [Markevich]. Similar to the present study of VOH, this results in a splitting of the (= /-) level in agreement with an orthorhombic-I symmetry, while no line splitting is observed for the (-/0) level because of the thermal averaging. It seems probable that a similar trend to the one observed for the VO complex in silicon and germanium applies to the VOH complex in silicon, i.e. that the reorientation barrier in the positive charge state is significantly lower than the barrier in the neutral charge state determined as 0.56 eV [Andersen 2000]. As discussed in the background section, calculations of the barriers for the hopping of oxygen and hydrogen in the VOH complex confirm these observations. Both barriers were estimated as only ~ 0.1 eV for the positively charged defect [Coutinho]. Thus,

the lack of line splitting is fully consistent with the donor level of the VOH complex. Our results indicate that the reorientation barrier for the positively charged complex is less than ~ 0.3 eV.

7.5 Hydrogen passivation of the divacancy

7.5.1 Electronic properties

Figure 7.8 shows Arrhenius plots for the majority carrier emissions from the levels related to the different charge states of the divacancy and the level here assigned to the single acceptor level of the divacancy-hydrogen complex V_2H . The data were obtained from series of Laplace DLTS measurements carried out at different temperatures. We obtain the activation enthalpies as $\Delta H_n = 0.224$ eV for $V_2 (= /-)$, $\Delta H_n = 0.384$ eV for $V_2 (-/0)$, $\Delta H_p = 0.203$ eV for $V_2 (+/0)$ and $\Delta H_n = 0.415$ eV for $V_2H (-/0)$. The emission data are displayed in Table 7.2. The activation enthalpies for the three charge states of the divacancy are in reasonable agreement with literature data [Brotherton 1982], [Irscher 1984]. Unfortunately, the literature contains serious scattering and inconsistencies for the electronic properties of the peak here assigned to $V_2H (-/0)$, e.g. activation enthalpies between 0.39 eV [Hüppi 1990], [Palmetshofer 1992] and 0.49 eV [Tokuda 1998] have been reported. Presumably, this is related to the poor resolution offered by conventional DLTS, which often displays $V_2H (-/0)$ only as a shoulder to the more dominant $V_2 (-/0)$. In general, we find that the improved resolution offered by Laplace DLTS provides a much more reliable determination of the activation enthalpy.

The capture of majority carriers into the defects has been examined by using the filling pulse method in combination with Laplace DLTS. The measurements were carried out at temperatures 130 K for $V_2 (= /-)$, 240 K for $V_2 (-/0)$ and 240-290 K for $V_2H (-/0)$. The high capture rate for $V_2 (+/0)$ made it impossible to study the capture process for this defect. We obtain the electron capture cross sections as $\sigma_n = 3 \times 10^{-16}$ cm² for $V_2 (= /-)$, $\sigma_n = 5 \times 10^{-15}$ cm² for $V_2 (-/0)$ and $\sigma_n = 2 \times 10^{-17}$ cm² for

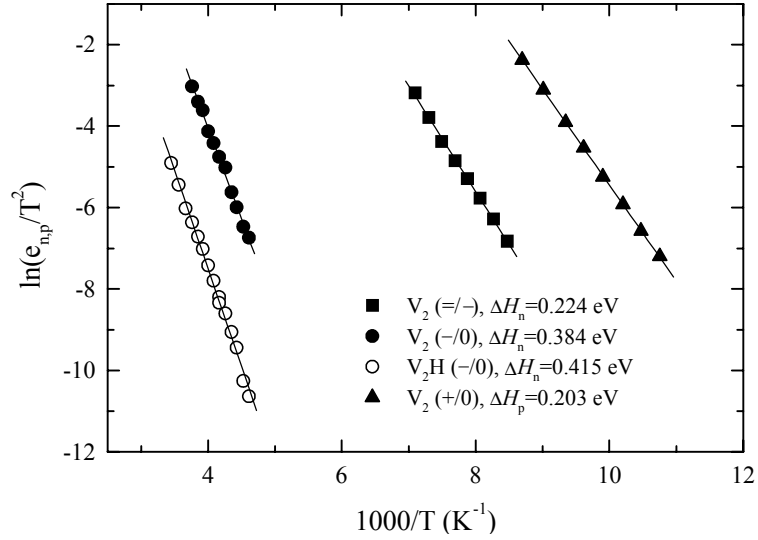


Figure 7.8: Arrhenius plots for the majority carrier emissions from $V_2 (= /-)$, $V_2 (-/0)$, $V_2 (+/0)$ and $V_2\text{H} (-/0)$.

$V_2\text{H} (-/0)$. In the case of $V_2\text{H} (-/0)$, we investigated the temperature dependence of the capture process and found a very small energy barrier ($E_{\sigma_n} \lesssim 0.02$ eV) for the capture of electrons into the defect. The capture data are displayed in Table 7.2. In general, the results are in excellent agreement with a previous capture study carried out by Hallén et al. [Hallén 1996]. We propose that $V_2\text{H} (-/0)$ is a single acceptor level but, as a result of the rather low electron capture cross section associated with the trap, we cannot rule out the possibility of a double acceptor level.

| $\Delta H_{n,p}$ (eV) | $\sigma_{n,p}$ (cm^2) | Identification |
|-----------------------|----------------------------------|---------------------|
| 0.224 | 3×10^{-16} (130 K) | $V_2 (= /-)$ |
| 0.384 | 5×10^{-15} (240 K) | $V_2 (-/0)$ |
| 0.203 | | $V_2 (+/0)$ |
| 0.415 | 2×10^{-17} (240-290 K) | $V_2\text{H} (-/0)$ |

Table 7.2: Activation enthalpies $\Delta H_{n,p}$ for the majority carrier emission processes, directly measured majority carrier capture cross sections $\sigma_{n,p}$ and proposed identifications of the deep levels under study.

7.5.2 Effect of hydrogen on defect concentrations

Our identification of the divacancy-hydrogen complex V_2H is based on the observation of an anti-correlation with the divacancy in regions with different hydrogen concentration. The effect is well illustrated by the Laplace DLTS spectra presented in Figure 7.3. In the as-irradiated material, $V_2 (-/0)$ is the only dominant peak in the spectrum, while $V_2 (-/0)$ and $V_2H (-/0)$ are comparable in magnitude after 20 W plasma treatment. Finally, after strong hydrogenation at a power of 50 W, $V_2 (-/0)$ vanishes and $V_2H (-/0)$ is the only dominant peak in the spectrum.

Figure 7.9(a) shows depth distributions of $V_2 (= /-)$ and $V_2H (-/0)$ in FZ n-Si hydrogenated by room temperature plasma treatment at a power of 20 W. The trap profiles were obtained from Laplace DLTS measurements by keeping a fixed reverse bias of -9 V and gradually changing the fill pulse. The two profiles are anti-correlated, with the concentration ratio of V_2H and V_2 systematically increasing towards the treated surface. Throughout the material, the sum-signal of V_2 and V_2H is practically constant and equal to the as-irradiated divacancy concentration. The profile shape of V_2H is comparable to that of the VOH complex (not shown). The small decrease in the concentration of V_2H close to the surface has been observed in a number of samples and indicates the formation of higher order hydrogen complexes in the strongly hydrogenated sub-surface region.

Figure 7.9(b) depicts the amplitudes of the DLTS signals $V_2 (= /-)$ and $V_2H (-/0)$ as a function of power during room temperature plasma treatment. The DLTS measurements were carried out with a reverse bias of -5 V and a fill pulse of -0.5 V. Similar to the depth profiles, the concentrations of the two defects are anti-correlated for different levels of hydrogenation. The sum-signal of V_2 and V_2H is significantly decreased after strong hydrogenation at a power of 50 W.

Isothermal annealing experiments have been carried out at 180 °C on a FZ n-Si sample hydrogenated by remote plasma treatment at room temperature. Figure 7.10 depicts the change in the amplitudes of the Laplace DLTS signals $V_2 (= /-)$ and V_2H

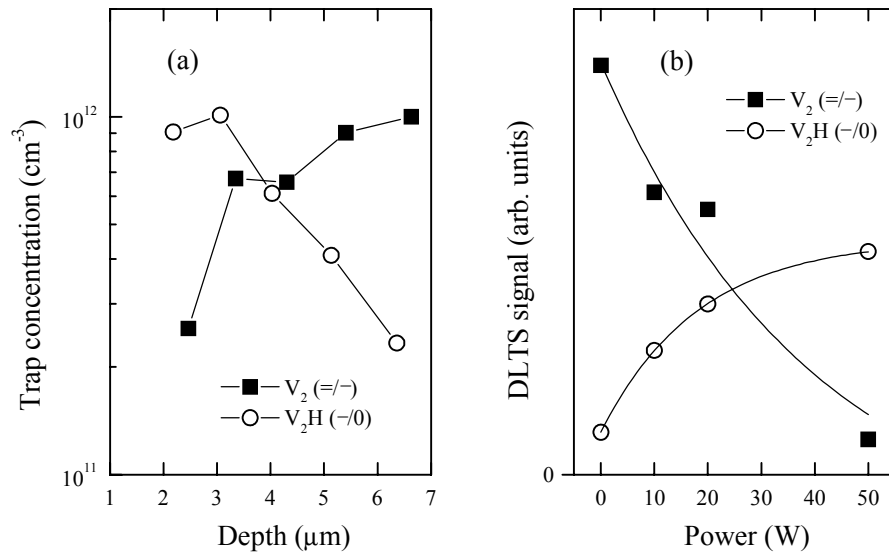


Figure 7.9: (a) Depth distributions of V₂ (= /-) and V₂H (- /0) in 38-50 Ω-cm FZ n-Si hydrogenated by 20 minutes room temperature plasma treatment at a power of 20 W. (b) Amplitude of the DLTS signals V₂ (= /-) and V₂H (- /0) as a function of power during 20 minutes room temperature plasma treatment.

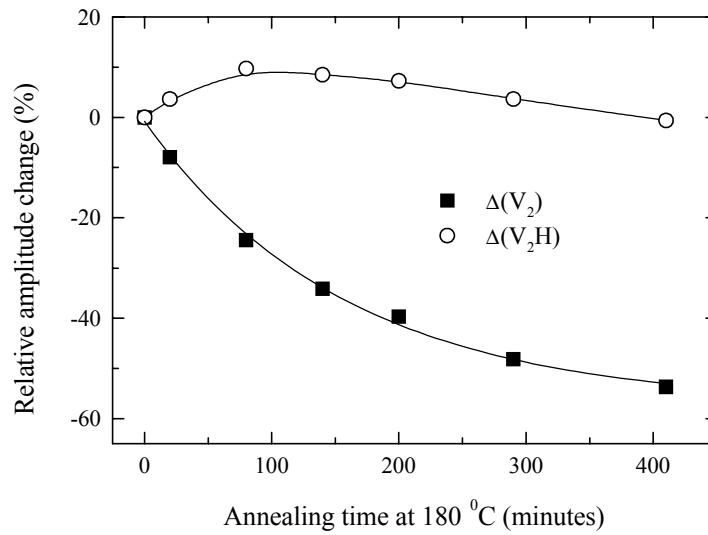


Figure 7.10: Isothermal (180 °C) annealing data of V₂ (= /-) and V₂H (- /0) obtained in a 38-50 Ω-cm FZ n-Si sample hydrogenated by room temperature remote plasma treatment. The graph shows the change in the amplitudes of V₂ and V₂H relative to the initial amplitude of V₂ versus annealing time.

($-/0$) relative to the initial amplitude of V_2 ($= /-$) as a function of annealing time at 180 °C. The annealing data demonstrate a clear passivation of the divacancy as hydrogen is released during the heat treatment. The concentration of V_2H is initially increased but eventually reaches a maximum and starts to decrease after ~ 100 minutes annealing. Similar to the data presented above, this indicates that V_2H itself can interact with hydrogen to form higher order V_2H_n complexes. The transformations between the V_2 and V_2H complexes are somewhat similar to those observed between the VO and VOH complexes during the same annealing sequence (Figure 7.5).

7.5.3 Discussion

The experimental results presented in this section clearly demonstrate that the divacancy can interact with hydrogen to form divacancy-hydrogen complexes. We have suggested that the level located at $E_c - 0.415$ eV is related to the single acceptor level of the divacancy-hydrogen complex, V_2H ($-/0$), formed as a result of the reaction $V_2 + H \rightarrow V_2H$. It seems unlikely that a defect formed by interactions of hydrogen with another radiation induced defects shows the same anti-correlation to the divacancy. Further, several of the dominant hydrogen-related deep level defects in irradiated material (e.g. VOH and C_iO_i-H) have been identified as having different electronic properties to those established for the peak assigned to V_2H ($-/0$). The correlation between the depth distributions of V_2H and the VOH centre suggests that the two complexes contain the same number of hydrogen atoms. To further support our identification, similar transformations were observed between VO and VOH and between V_2 and V_2H during isothermal annealing at 180 °C. Both VOH and V_2H are formed by attachment of one hydrogen atom to the original defect and both complexes can themselves interact with hydrogen to form VOH_2 and higher order V_2H_n centres, respectively. Finally, the electrical properties of V_2H are expected to resemble those of the phosphorous-vacancy complex [Stallinga 1998] with a single acceptor level close to the position at $E_c - 0.415$ eV observed experimentally in the present work.

In addition to the formation of V_2H , the experimental data demonstrate the for-

mation of higher order divacancy-hydrogen complexes. As discussed in the background section, the V_2H_n ($n = 2, \dots, 6$) centres are all predicted to be electrically active with exception of the fully saturated V_2H_6 complex. The present work does not allow us to reliably identify these complexes. However, as illustrated in the Figures 7.2 and 7.3, the mid-gap region contains several unidentified hydrogen-related levels of rather low concentrations compared to the as-irradiated divacancy concentration. Further, a peak located at approximately 110 K in a conventional DLTS spectrum of irradiated n-Si has been observed in a number of samples after strong hydrogenation. These levels form possible candidates for higher order V_2H_n complexes.

7.6 Summary

We have studied the interactions of hydrogen with radiation induced defects in electron irradiated n-type and p-type silicon hydrogenated by remote plasma treatment. The passivation of the pure radiation induced defects and resulting formation of electrically active hydrogen-related complexes was demonstrated. The interactions of hydrogen with the vacancy-oxygen complex VO and the divacancy V_2 were studied in detail. It was established that the VOH complex introduces an acceptor level at $E_c - 0.312$ eV and a donor level at $E_v + 0.263$ eV, while the V_2H complex introduces an acceptor level at $E_c - 0.415$ eV. Further, these levels can themselves interact with hydrogen to form the higher order hydrogen complexes VOH_2 and V_2H_n ($n = 2, \dots, 6$), respectively. A new hydrogen-related level positioned close to the acceptor level of the divacancy was resolved by Laplace DLTS. Uniaxial stress measurements of both charge states of the VOH complex were carried out. The data established the general trend (also seen for the VO complex in silicon and germanium) that the reorientation barrier is systematically increased as more electrons are bound to the defect.

Chapter 8

Polarization of a hydrogen related defect in silicon studied by DLTS

The majority of the experimental work presented in this thesis deals with studies of majority carrier traps in silicon by means of DLTS. The analysis of deep level defects by DLTS is a proven and tested technique, used for numerous experimental studies during the past three decades. In this chapter, we present DLTS data related to a completely different effect. The fundamental experimental result is the observation of capacitance changes with opposite sign to those related to majority carrier emission from deep energy levels in the band gap. The aim of this chapter is to characterize the properties of these capacitance changes and present a preliminary model that goes some way towards explaining the effect. The first observations of these unusual capacitance were reported by Jonathan Terry [Terry 1999]. Subsequently, Janet Jacobs and Bruce Hamilton have carried out a detailed analysis of the effect, which has formed the background for the present work. I sincerely thank Janet and Bruce for their contributions.

8.1 Experimental details

8.1.1 Sample preparation

The majority of the samples were prepared from a (100) oriented Cz grown boron-doped p-type silicon wafer of resistivity 25 Ω -cm. A number of other boron-doped silicon substrates were used for comparison. These were (100) oriented 22 Ω -cm FZ p-Si, (100) oriented 0.6 Ω -cm Cz p-Si and (111) oriented 5-10 Ω -cm Cz p-Si. The various materials are listed in Table 8.1. The samples were hydrogenated by either wet chemical etching or exposure to a remote plasma. The etchings were carried out by immersing the samples in either (i) a CP4 solution of HNO₃ (70%), CH₃COOH and HF (48%) in the ratio 5 : 3 : 3 for 90 seconds, (ii) a solution of HF (48%) and H₂O in the ratio 1 : 10 for 90 seconds or (iii) HF (48%) for 30 minutes. Plasma treatments were carried out at room temperature, using a hydrogen gas pressure of \sim 1.0 mbar and a power of 30 W. Details of the plasma system were given in Chapter 4. Deuterated samples were prepared by immersing the samples in a solution of HF (48%) and D₂O in the ratio 1 : 10 for 90 seconds. Schottky barriers and Ohmic contacts were formed by sputtering of titanium and evaporation of gold, respectively.

Several phosphorous-doped n-type silicon samples of different resistivities, growth methods and surface orientations were prepared. The various materials are listed in Table 8.1. These samples were also hydrogenated at room temperature by either wet chemical etching or remote plasma treatment. Schottky barriers and Ohmic contacts

| p-type silicon | n-type silicon |
|--------------------------------------|---------------------------------------|
| (100) Cz p-Si (B), 25 Ω -cm | (100) Cz n-Si (P), 30-70 Ω -cm |
| (100) FZ p-Si (B), 22 Ω -cm | (100) FZ n-Si (P), 25 Ω -cm |
| (100) Cz p-Si (B), 0.6 Ω -cm | (100) Cz n-Si (P), 1.3 Ω -cm |
| (111) Cz p-Si (B), 5-10 Ω -cm | (111) Cz n-Si (P), 0.6 Ω -cm |

Table 8.1: List of materials used for this study.

were formed by evaporation of gold and aluminum, respectively.

8.1.2 Electric field distributions

Free carrier profiles were obtained from capacitance-voltage measurements. A reduction in the concentration of free carriers was observed towards the sample surface due to the formation of hydrogen-dopant complexes. The carrier profiles were used to calculate the spatial profile of the electric field. Figure 8.1 shows an example of the estimated field distribution in a hydrogenated 25 Ω -cm Cz p-Si sample for different values of the reverse bias. The electric field is constant several microns into the sample due to complete boron passivation in this region. Similar estimations of the electric field distribution will be used throughout the chapter.

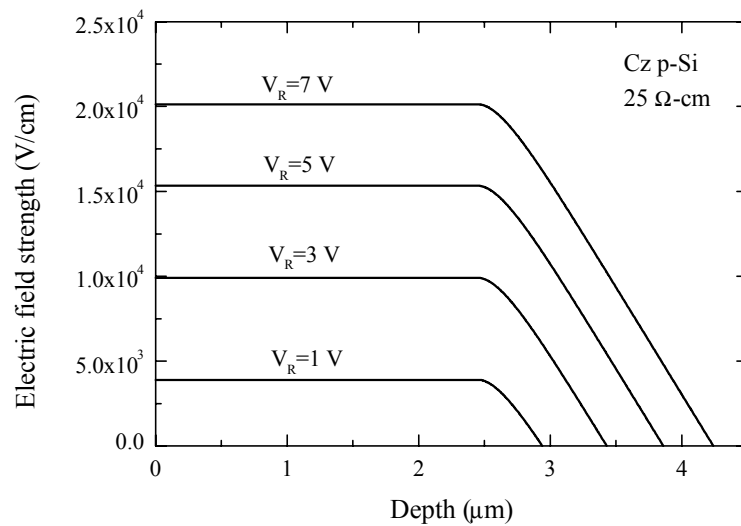


Figure 8.1: Estimated electric field distributions in a hydrogenated 25 Ω -cm Cz p-Si sample for different values of the reverse bias. Note the constant field strength several microns into the sample.

8.2 General effect

The fundamental experimental result is the observation of capacitance changes with opposite sign to those related to majority carrier emission from deep energy levels in the band gap. The effect is illustrated in Figure 8.2, showing isothermal capacitance

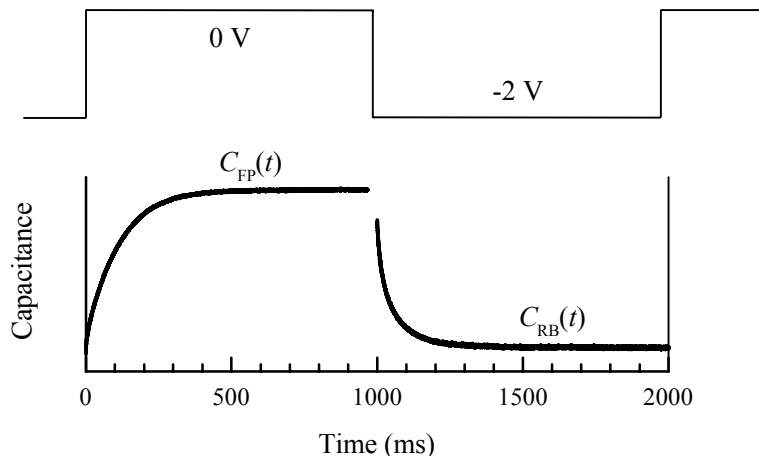


Figure 8.2: Capacitance transients recorded at 65 K during the fill pulse phase and the reverse bias phase of a DLTS pulse train. The two transients are shown on different capacitance scales.

changes during a DLTS pulse train recorded at 65 K in a hydrogenated 25 Ω -cm Cz p-Si sample. The measurements were carried out by Laplace DLTS with a reverse bias of -2 V and a fill pulse of 0 V. Unlike majority carrier emission from deep energy levels, the capacitance $C_{RB}(t)$ decreases during the reverse bias phase of the DLTS pulse train. Further, an increase of the capacitance $C_{FP}(t)$ is observed during the fill pulse phase of the measurement¹. We denote the two processes “the reverse bias phase process” and “the fill pulse phase process”, respectively². As illustrated in Figure 8.4, the effect produces a negative peak in a conventional DLTS spectrum. The aim of this chapter is to characterize and interpret these unusual capacitance changes.

8.3 Preliminary model

In this section, we present a preliminary model for the origin of the unusual capacitance changes. Then, in subsequent sections, we argue that the experimental results are consistent with the proposed model.

¹Laplace DLTS has a facility to carry out “reverse DLTS” in which the capacitance transient is recorded during the fill pulse phase of the measurement.

²We use the term “fill pulse phase process” though, as established below, the process is not related to trap filling.

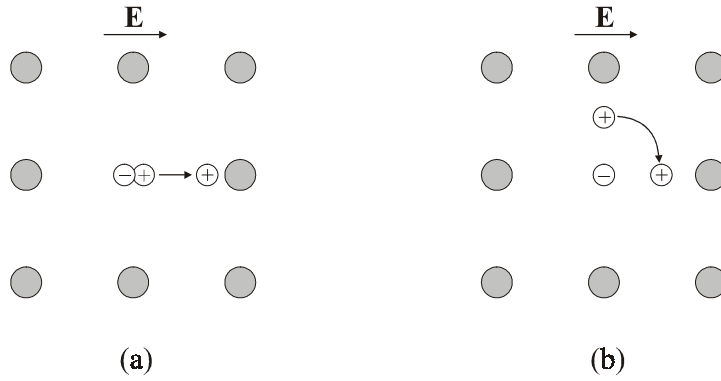


Figure 8.3: Two dimensional illustrations of a localized polarization event in the form of (a) increased charge separation and (b) defect alignment. Host atoms and atoms of the polarizing defect are shown in grey and white, respectively.

We relate the observed effect to a field-induced change of the charge distribution associated with a hydrogen-related defect located within the space charge region. During the reverse bias phase of the DLTS pulse train, a local movement of charge takes place driven by the electric field, while the opposite movement takes place during the fill pulse phase of the pulse train when the electric field strength is decreased. That is, the reverse bias phase process is a localized polarization event, while the fill pulse phase process is the corresponding de-polarization event. There are several ways in which the specific form of the polarization can take place. Two possible scenarios are depicted schematically in Figure 8.3. In Figure 8.3(a), we consider a model in which the electric field applied along the x -axis causes a net increase in the separation between two ions of opposite polarity. The polarization P_x in the x -direction of a population of this charge distribution (an electric dipole) is given by:

$$P_x(x, t) = qa_x(x, t)N_{pol}(x), \quad (8.1)$$

where q is the charges involved in the defect (assumed equal), $N_{pol}(x)$ is the concentration of the polarizing defect and $a_x(x, t)$ is the field-dependent charge separation in the x -direction. A spatial dependence of the charge separation is included to account for the electric field variation through the space charge region. The dependence on time is included in order to consider the non-steady-state conditions during a DLTS pulse

train. Figure 8.3(b) illustrates another model in which the local movement of charge is a field-induced reorientation of an ion, forming an alignment of the defect within the silicon lattice. Other scenarios than the two shown in Figure 8.3 are possible and for the time being we will not restrict ourselves to one specific form of atomic movement.

In the following sections, we argue that the experimentally observed properties of the unusual capacitance changes are, at least to some extent, well described by the proposed model of a localized polarization event of a hydrogen-related defect. We consider (i) the influence of the experimental conditions on the formation of the effect, including the relation to hydrogen, (ii) the sign of the capacitance changes and the local nature of the effect, (iii) the kinetics of the processes as a function of electric field and temperature, (iv) the magnitude of the capacitance changes under different experimental conditions and (v) the annealing characteristics of the effect. Finally, we discuss the possible microscopic identity of the polarizing complex.

8.4 Formation conditions

8.4.1 Relation to hydrogen

There are several arguments to support the suggestion that the effect is related to hydrogen. Firstly, the unusual capacitance changes have been observed in numerous p-Si samples hydrogenated by wet chemical etching. A typical conventional DLTS spectrum of an etched 25 Ω -cm Cz p-Si sample is shown in Figure 8.4(a) (bold line). One sample was prepared without any deliberate hydrogenation by cleaning the material only in trike, acetone and methanol before sputtering of titanium. Obviously, this affected the Schottky diode quality but the devices still showed diode characteristics and were still measurable by DLTS. No signs of the effect were seen in this sample, as illustrated in Figure 8.4(a) (thin line). The sample without hydrogenation was subsequently exposed to a remote hydrogen plasma at room temperature. A comparison of conventional DLTS spectra obtained before plasma treatment and after 6 hours treatment is shown in Figure 8.4(b). The data demonstrate the formation of the negative peak after hydro-

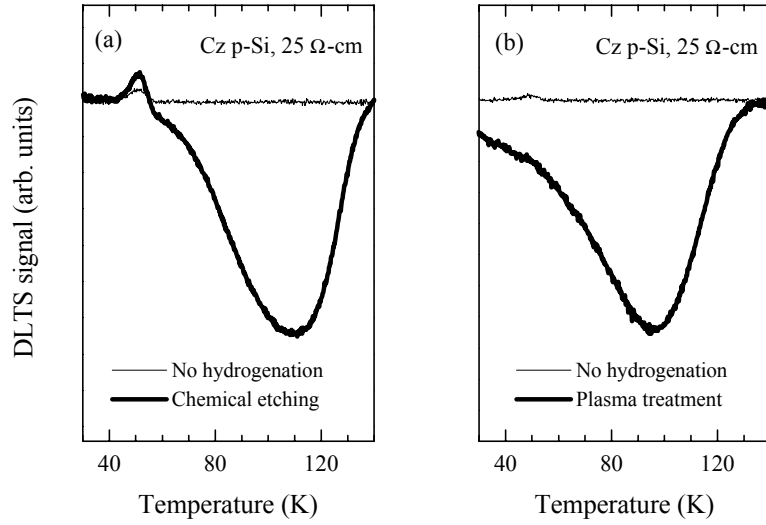


Figure 8.4: (a) 200 s^{-1} conventional DLTS spectra of two $25 \text{ } \Omega\text{-cm}$ Cz p-Si samples prepared without hydrogenation and by chemical etching. Note, that both samples display a small positive peak at $\sim 50 \text{ K}$ related to emission from an unknown majority carrier trap. (b) 200 s^{-1} conventional DLTS spectra of a $25 \text{ } \Omega\text{-cm}$ Cz p-Si sample before and after 6 hours hydrogen plasma treatment at room temperature.

generation. Finally, as discussed below, data from the present work and comparable data obtained by Janet Jacobs were successfully reproduced by numerical modeling under the assumption that a proportion of the total hydrogen concentration was involved in the polarizing defect.

8.4.2 Comparison of different materials

The majority of the experimental work has been carried out on hydrogenated (100) oriented $25 \text{ } \Omega\text{-cm}$ Cz p-Si. This material has been compared to a number of other materials (Table 8.1) in order to establish the dependence of the effect on surface orientation, growth method, dopant type and doping level. These are important parameters with regards to the microscopic identity of the polarizing defect.

The unusual capacitance changes were also observed in (100) oriented $22 \text{ } \Omega\text{-cm}$ FZ p-Si with no significant deviation from the results obtained in (100) oriented $25 \text{ } \Omega\text{-cm}$ Cz p-Si. Note, that the two materials have the same surface orientation and comparable resistivity. This result indicates that the effect is not sensitive to the

oxygen concentration in the material. In order to study the influence of the direction of the electric field in the space charge region, the (100) oriented 25 Ω -cm Cz p-Si was compared to (111) oriented 5-10 Ω -cm Cz p-Si. No significant differences were observed between the signals in the two materials. The effect of doping level was examined by comparison of the (100) oriented 25 Ω -cm Cz p-Si to (100) oriented 0.6 Ω -cm Cz p-Si. In general, the relative amplitude dC/C of the transients were larger in the higher doped material, typically by a factor of 2-3 under comparable experimental conditions.

Several attempts were made to form the effect in n-type silicon as well. Table 8.1 lists the various n-Si materials that have been used. Methods of hydrogenation included different types of wet chemical etching and remote plasma treatment. Some of the samples were reverse bias annealed at room temperature and at 100 °C after hydrogenation. Despite these efforts, no signs of the unusual capacitance transients have been observed in any of the hydrogenated n-Si samples under any experimental conditions. This is somewhat surprising as the effect has been reported by Janet Jacobs also in n-Si, though the signals were generally stronger in p-Si.

8.5 Sign of the capacitance changes

Let us consider the sign of the capacitance changes during a DLTS pulse train as predicted by the polarization model. When reverse bias is applied, the enhancement of the electric field in the x -direction causes an increase in the charge separation $a_x(x, t)$ (i.e. a movement $\Delta a_x(x, t)$) and a corresponding increase in the polarization $P_x(x, t)$. The overall electric field is screened and the space charge region is pushed out. This results in a transient decrease of the reverse bias capacitance $C_{RB}(t)$ towards the steady-state value $C_{RB}(\infty)$. After application of the fill pulse, the external electric field is reduced and the original situation is restored by the opposite movement of charge. Consequently, the space charge region shrinks and a transient increase of the fill pulse capacitance $C_{FP}(t)$ towards the steady-state value $C_{FP}(\infty)$ results. Thus, the capacitance changes predicted by the polarization model are in agreement with the signs observed exper-

imentally for the reverse bias phase process and the fill pulse phase process (Figure 8.2).

The capacitance decrease during the reverse bias phase is also consistent with emission of minority carriers from traps within the space charge region. This effect is frequently studied by minority carrier transient spectroscopy, where minority carriers are injected into the space charge region by application of either a light pulse or a forward bias. In the present case, however, no minority carriers are generated. Further, as shown below, the unusual capacitance changes do not behave in any way like carrier emission from deep energy levels.

Somewhat similar capacitance transients have been reported in n-type silicon by Herring et al. [Herring 2001]. The authors concluded that the effect was related to long-range ion drift of atomic hydrogen. In this experiment, monoatomic hydrogen was created by hole-stimulated dissociation of phosphorous-hydrogen complexes and was subsequently driven towards the front surface by the electric field under a reverse bias. This produced a transient decrease of the capacitance as seen in the present work. Similar ion-drift-induced capacitance transients have been reported for copper in p-type silicon [Heiser 1998]. It is, however, very unlikely that such long-scale drift of hydrogen (or another species) is responsible for the effect observed in the present work. Firstly, no minority carriers were injected to release atomic hydrogen from dopant-hydrogen complexes. Secondly, the time constants of the observed capacitance transients are orders of magnitude smaller than those expected for long-range drift of hydrogen. Third, the amplitudes of the capacitance changes do not change as the DLTS measurements progress. In the case of long-range movement, we would expect a quantitatively non-reversible process as some hydrogen would diffuse beyond the space charge region.

In summary, the sign of the capacitance changes are consistent with the proposed model of a localized polarization event. We can exclude the possibilities of emission from minority carrier traps and long-range drift of hydrogen through the space charge region.

8.6 Kinetics

The kinetics of the reverse bias phase process and the fill pulse phase process depend on the history of the given sample and the experimental conditions. Essentially, this means that the time constants of the processes can differ from sample to sample and can change upon room temperature annealing. This instability is an important characteristic of the unusual capacitance changes and will be treated in more detail later in the chapter. Obviously, the instability makes it extremely difficult to reliably characterize the kinetics of the processes. It is, however, possible to extract some generalizations regarding the influence of electric field and temperature on the time constant. It is important to emphasize that no instability is observed below 200 K, where all measurements have been carried out. Thus, at the measurement temperature, the signal is stable and the data are reproducible.

8.6.1 Electric field dependence of the reverse bias phase process

Figure 8.5(a) depicts Laplace DLTS spectra of the reverse bias phase process measured at 60 K in a hydrogenated 25 Ω -cm Cz p-Si sample. The spectra have been obtained at a fixed fill pulse of 0 V with a pulse width long enough to reach saturation. The value of the reverse bias is varied, consequently changing the width of the space charge region and the electric field distribution in the measurement phase. A typical example of the estimated field distribution for various values of the bias is given in Figure 8.1. In general, the Laplace spectra in Figure 8.5(a) show either a broad structure or multiple peaks, indicating a distribution of time constants. The spectra shift towards higher rate and the process becomes increasingly non-exponential for larger values of the reverse bias. These observations show that the reverse bias phase process speeds up significantly in the presence of an electric field.

We have carried out a quantitative analysis of the electric field dependence for field strengths below $\sim 2 \times 10^4$ V/cm. The polarization model illustrated in Figure 8.3(a) forms a system of a mobile charge q_1 attracted to an immobile centre of charge

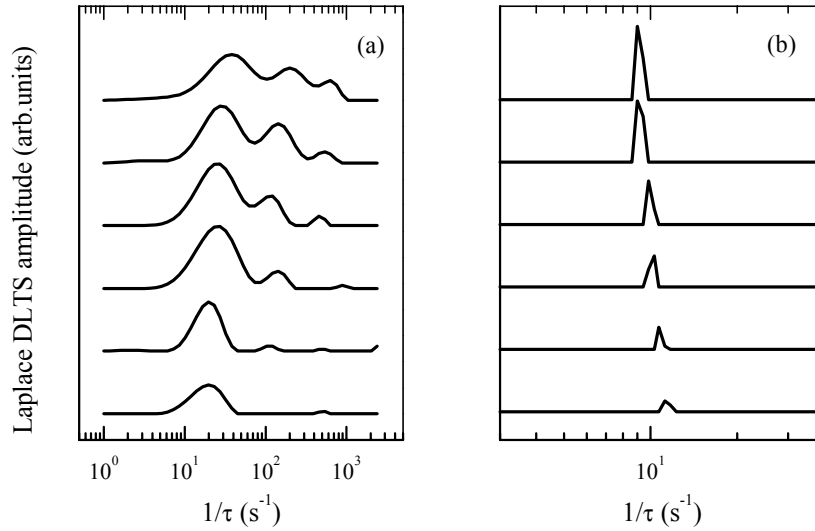


Figure 8.5: Laplace DLTS spectra of (a) the reverse bias phase process and (b) the fill pulse phase process. The spectra have been obtained at 60 K in a hydrogenated 25 Ω -cm Cz p-Si sample. The fill pulse is fixed at 0 V, while the value of the reverse bias is increased from the bottom to the top of the figures. The values of the reverse bias are in the range from 0.3 V to 5 V.

q_2 of opposite polarity. As a first approximation, it seems feasible to describe the field-lowering of the barrier associated with the polarization event in a similar way to the field-lowering of the Coulomb-barrier associated with carrier emission from a defect centre of opposite polarity, i.e. the Poole-Frenkel effect. Figure 8.6 depicts the approximate rate of the reverse bias phase process relative to the zero-field rate as a function of the field parameter $\omega = \frac{\sqrt{e^3 \mathcal{E}_{\max} / \pi \epsilon_s}}{k_B T}$, where \mathcal{E}_{\max} is the maximum electric field strength at the given reverse bias. The data are compared to the field dependence obtained from the three dimensional Poole-Frenkel effect for a system of two Coulombically attractive charges under the influence of a uniform electric field. The data are in good agreement with the applied model and give the fitting parameter $q_1 q_2 = (0.82e)^3$. It is important to emphasize the approximations in this approach. Firstly, the field strength is over-estimated as the maximum field strength is given. Secondly, the rate of the process is estimated from a highly non-exponential transient. However, the results indicate that the considered model is reasonable and that the charges involved are in the order of the elementary charge.

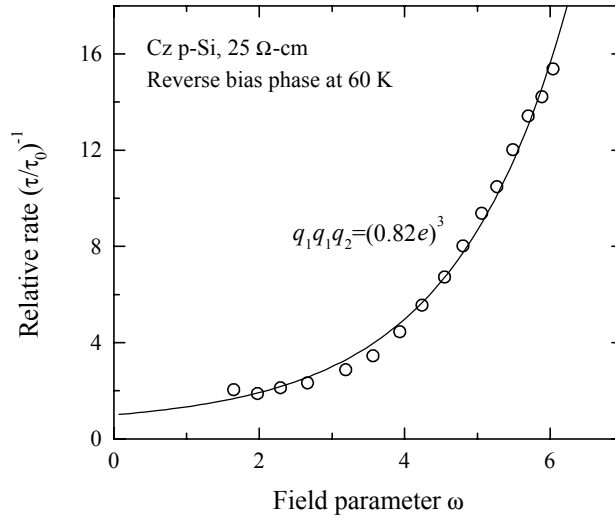


Figure 8.6: The rate of the reverse bias phase process relative to the zero-field rate versus the field parameter $\omega = \frac{\sqrt{e^3 \mathcal{E}_{\max} / \pi \epsilon_s}}{k_B T}$, where \mathcal{E}_{\max} is the maximum field strength at the given reverse bias. The solid line represents the best fit to the data obtained from the three dimensional Poole-Frenkel effect for a mobile charge q_1 attracted to an immobile centre of charge q_2 of opposite polarity. The zero-field emission rate was obtained by extrapolation of the curve to $\omega = 0$. The fitting yields $q_1 q_1 q_2 = (0.82e)^3$.

8.6.2 Electric field dependence of the fill pulse phase process

Unlike the reverse bias phase process, the fill pulse phase process is practically mono-exponential. This is illustrated in Figure 8.5(b), showing Laplace DLTS spectra of the fill pulse phase process obtained at 60 K. The spectra have been recorded with a fixed fill pulse of 0 V, while the value of the reverse bias is varied. The Laplace DLTS spectra contain sharp single lines with practically no change in time constant. The difference to the reverse bias phase process shown in Figure 8.5(a) is striking. Sharp Laplace DLTS lines were also obtained by measuring at different fill pulse values. The mono-exponential nature of the fill pulse phase process complies with the proposed polarization model. In this model, the fill pulse phase process represents an event of de-polarization, i.e. a recovery process with a time constant that is not directly influenced by the electric field strength in the reverse bias phase.

8.6.3 Relation between the two processes

Let us establish an important correlation between the kinetics of the two processes. In the usual case of studying deep energy levels by DLTS, the fill pulse phase process (carrier capture) and the reverse bias phase process (carrier emission) take place on very different time scales. This is not the case for the unusual signals studied here. At a given temperature, the time constants for the fill pulse phase process and the reverse bias phase process are comparable, with the former process always being slower than the latter. This is illustrated by the Laplace DLTS spectra in Figure 8.5, where the rate for the fill pulse phase process is $\sim 10 \text{ s}^{-1}$ and the rate for the reverse bias phase process is in the range $\sim 20\text{-}1000 \text{ s}^{-1}$ depending on the value of the reverse bias. This correlation indicates that the mechanisms involved in the two processes are essentially similar, with a lowering of the energy barrier in the presence of an electric field.

8.6.4 Temperature dependence

As a result of the instability of the signal, it is extremely difficult to quantify reliably the temperature dependence of the time constants of the processes. Figure 8.7 shows the rate of the fill pulse phase process as a function of inverse temperature for three hydrogenated 25 $\Omega\text{-cm}$ Cz p-Si samples (open symbols). It is most convenient to describe the temperature dependence of the fill pulse phase process as the transient is mono-exponential but the reverse bias phase process follows the same behavior.

We conclude from Figure 8.7 that the process is thermally activated. In general, the data cannot be described by a single Arrhenius slope but are well fitted by the sum of two Arrhenius expressions. A break in the slope typically appears at approximately 80-100 K. The slower of the two processes (dominating at low temperature) has an activation energy in the range 0.04-0.05 eV with a pre-exponential factor of $10^3\text{-}10^5 \text{ s}^{-1}$, while the faster of the two processes (dominating at high temperature) has an activation energy in the range 0.14-0.22 eV with a pre-exponential factor of $10^9\text{-}10^{12} \text{ s}^{-1}$. The break in the slope of the Arrhenius curve is indicative of a transition

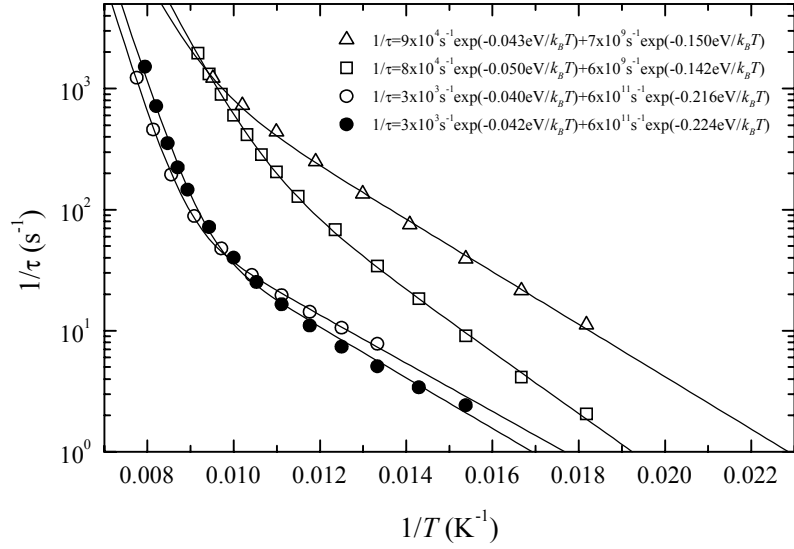


Figure 8.7: Arrhenius plots for the fill pulse phase process in hydrogenated (open symbols) and deuterated (solid symbols) 25 Ω -cm Cz p-Si. Solid lines represent best fits to the data obtained by using a sum of two Arrhenius expressions.

in the mechanism responsible for the process. A transition from thermally assisted tunneling at low temperatures to classical jumping over a barrier at high temperatures has been reported for other hydrogen-related systems in silicon, e.g. the reorientation of the hydrogen-boron complex with a crossover temperature of ~ 70 K [Cheng 1994], [Noya 1997] and the diffusion of atomic hydrogen with a crossover temperature of ~ 170 K [Langpape 1997]. Thus, it is tempting to propose a similar transition between thermally assisted tunneling and classical motion over a barrier in the present case. There are, however, major difficulties with this interpretation. The first problem is the strong variation observed between different samples. The samples have all been prepared from the same wafer and none of the samples have undergone annealing above room temperature. Thus, it seems extraordinary that the signals display such different Arrhenius behavior. Secondly, the pre-exponential factors of 10^3 - 10^5 s^{-1} and 10^9 - 10^{12} s^{-1} in the two regimes appear inconsistent with the values expected for thermally assisted tunneling and classical motion over a barrier, respectively [Cheng 1994].

Comparison of the Arrhenius plots for hydrogenated and deuterated samples is also

complicated by the strong variation observed between the samples. Figure 8.7 shows an Arrhenius plot for a deuterated 25 Ω -cm Cz p-Si sample (solid symbols). No conclusive difference to the hydrogenated samples is seen.

8.7 Signal amplitude

In this section, we consider the amplitude of the unusual capacitance changes under different experimental conditions. In general, these data showed a much more consistent behavior from sample to sample than the temperature dependence of the time constant considered above.

8.7.1 The reverse bias phase process

The reverse bias phase process was studied at 50 K in a hydrogenated 25 Ω -cm Cz p-Si sample. The measurements were carried out at a fixed fill pulse of 0 V, while the value of the reverse bias was varied. Laplace DLTS spectra for this type of measurements were presented in Figure 8.5(a). Figure 8.8 depicts the relative signal amplitude $dC_{\text{RB}}/C_{\text{RB}}$ of the capacitance transient versus the width of the space charge region at the given reverse bias (open symbols). Here, C_{RB} is the capacitance during the reverse bias phase. Also shown in Figure 8.8 is the profile of boron-hydrogen complexes (solid symbols) determined from capacitance-voltage measurements of the free carrier profile. The relative signal amplitude $dC_{\text{RB}}/C_{\text{RB}}$ initially increases strongly with the width of the space charge region but eventually saturates as the boron-hydrogen concentration vanishes.

Numerical modeling of the above data has been carried out by Prof. Bruce Hamilton. For this purpose, the hydrogen distribution in the sample was estimated by fitting the tail of the boron-hydrogen profile and extending the profile all the way to the surface (solid curve in Figure 8.8). This approach gave a surface hydrogen concentration of $\sim 3 \times 10^{16} \text{ cm}^{-3}$. As a crude approximation, it was assumed that the spatial profile of the hydrogen-related polarizing defect was equal to the estimated hydrogen profile.

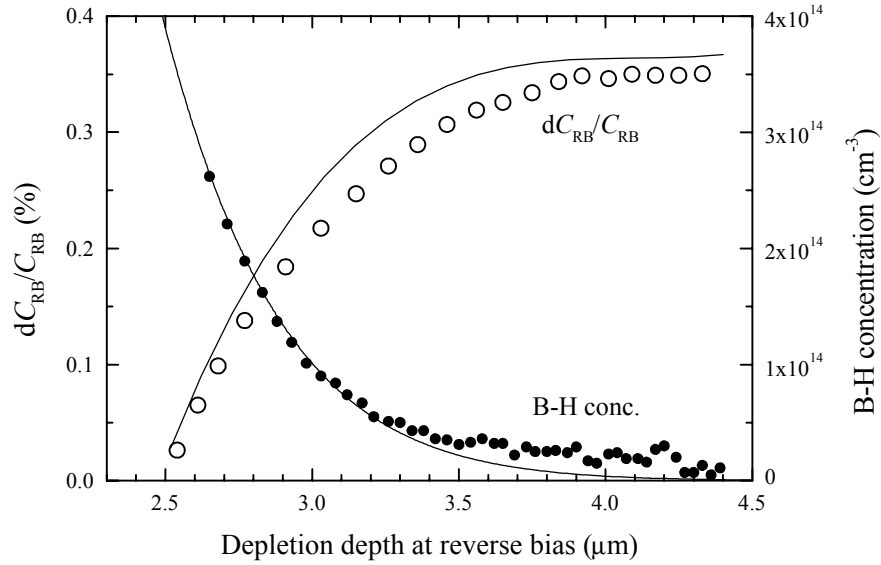


Figure 8.8: Relative amplitude dC_{RB}/C_{RB} of the reverse bias phase transient versus depletion depth obtained experimentally (open symbols) and by numerical modeling (solid curve). The measurements were carried out at 50 K at a fixed fill pulse of 0 V. Also shown is the profile of boron-hydrogen complexes obtained from capacitance-voltage measurements (solid symbols) and the best fit to the profile (solid curve).

The electric field distribution in the samples under various bias conditions was obtained as described above (Figure 8.1). The modeling assumed that the electric field causes a net increase in the separation between two charges of opposite polarity, both having the magnitude of the elementary charge. By applying these assumptions and approximations, the only unknown parameter in the polarizing system is the magnitude of the charge movement versus electric field strength. The modeling was carried out by assuming a specific form of charge movement versus field strength and subsequently calculating the resulting lowering of the effective electric field through the space charge region and the corresponding capacitance decrease by applying Poisson's equation. This procedure was carried out for several bias conditions, hence data for dC_{RB}/C_{RB} versus the width of the space charge region were obtained. It was concluded that the DLTS data were reproduced successfully by choosing a charge movement that initially increases linearly with field strength and then saturates. Figure 8.9(a) depicts

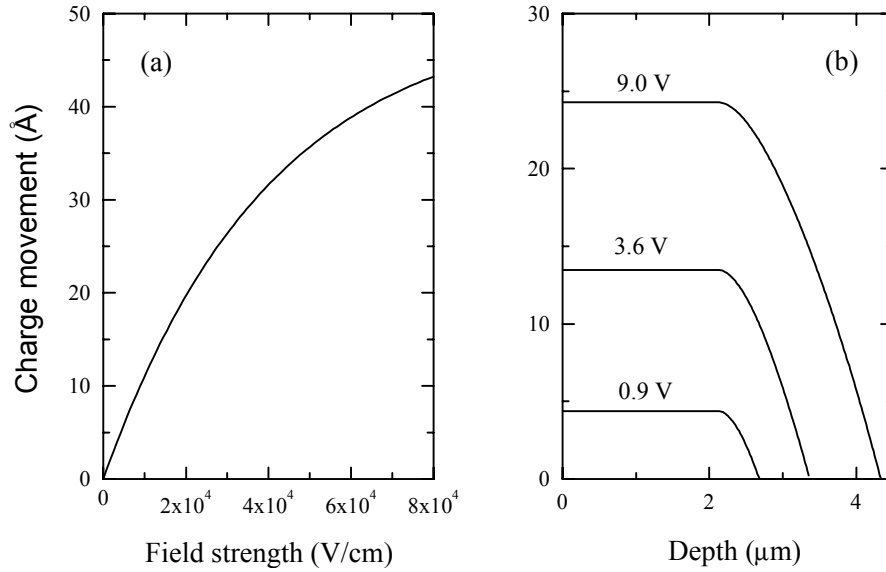


Figure 8.9: (a) Charge movement versus electric field strength used in the numerical modeling. (b) Charge movement versus depth for three different bias conditions.

the specific form of the charge movement used in the modeling. The corresponding charge movements as a function of depth is shown in Figure 8.9(b) for three different bias conditions.

We now consider the results of the numerical modeling. Figure 8.8 shows the relative amplitude $dC_{\text{RB}}/C_{\text{RB}}$ versus the width of the space charge region obtained by the modeling (solid curve). The shape of the curve is in excellent agreement with the experimental data measured by Laplace DLTS. This correlation provides strong support for the polarization model. In order to obtain agreement with the experimental data, it was necessary to assume charge movements on the order of ~ 10 Å for typical field strengths of $\sim 1 \times 10^4$ V/cm (Figure 8.9). This value is by approximately one order of magnitude larger than the charge movements expected for a localized polarization event. This discrepancy may be related to the rather crude estimation of the spatial profile of the polarizing defect, which strongly affects the estimated magnitude of the charge movement. Below, we discuss this in more detail.

Numerical modeling has also been carried out on similar DLTS data obtained by Dr. Janet Jacobs [Hamilton]. The samples used in this work were prepared from

(100) oriented Cz p-Si with a boron concentration of $\sim 6 \times 10^{15} \text{ cm}^{-3}$. The surface hydrogen concentration was estimated as $\sim 1 \times 10^{19} \text{ cm}^{-3}$, i.e. almost three orders of magnitude larger than for the data obtained in the present work. Also in this case, there was an excellent agreement between the experimental and the modeled data for $dC_{\text{RB}}/C_{\text{RB}}$ versus the width of the space charge region. The magnitude of the charge movement used in the modeling was below 1 \AA for field strengths below $1 \times 10^5 \text{ V/cm}$, i.e. approximately one order of magnitude smaller than the movements used for the data obtained in the present work. This difference occurs because of the strong variations in the estimated surface concentration of hydrogen in the two sets of samples.

We conclude that the experimental DLTS data are successfully reproduced by a model of a localized polarization event. At present, however, the estimation of the hydrogen profile used in the modeling is rather crude and probably not representative of the true hydrogen distribution. This strongly affects the estimations of the charge movements involved in the polarization events. We are currently trying to obtain a more realistic measure of the hydrogen profile for direct use in the modeling.

8.7.2 The fill pulse phase process

Laplace DLTS spectra of the fill pulse phase process recorded at 60 K in a hydrogenated 25 Ω -cm Cz p-Si sample were presented in Figure 8.5(b). The spectra were obtained at a fixed fill pulse of 0 V, while the value of the reverse bias was varied. With this set-up, the space charge region and the electric field distribution in the measurement phase (i.e. the fill pulse phase) is fixed through the measurement series. Only the electric field in the reverse bias phase is varied. Figure 8.10 depicts the relative amplitude $dC_{\text{FP}}/C_{\text{FP}}$ of the fill pulse phase transient as a function of the maximum electric field strength during the reverse bias phase. Applying the model of localized polarization, the data in Figure 8.10 represent the amplitude of the de-polarization process as a function of the polarization field. We interpret that the amplitude initially increases linearly with field strength and then goes towards saturation. The effect of saturation has been observed consistently in a number of hydrogenated samples and was more pronounced in higher

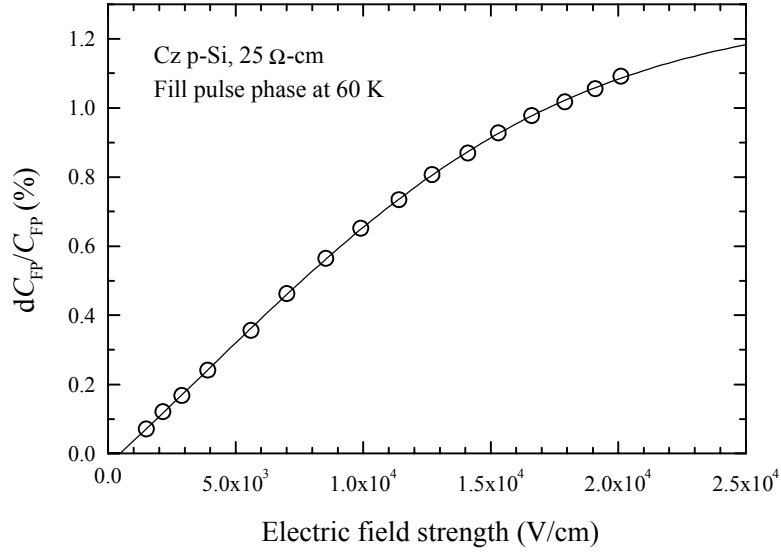


Figure 8.10: Signal amplitude dC_{FP}/C_{FP} of the fill pulse phase transient as a function of the maximum electric field strength during the reverse bias phase. The measurements were carried out at 60 K at a fixed fill pulse of 0 V. The solid line is a guidance to the eye.

doped 0.6 Ω -cm Cz p-Si material, where field strengths up to $\sim 1 \times 10^5$ V/cm were applied. This observation provides further support for the proposed model. In order to reproduce the experimental data in Figure 8.8 by numerical modeling, it was essential to assume a charge movement that initially increases linearly with field strength and then saturates (Figure 8.9(a)). We interpret that the experimentally observed saturation of the amplitude of the de-polarization process as a function of polarization field strength is caused by the corresponding saturation of the atomic charge movement.

8.8 Annealing experiments

As mentioned previously, the unusual DLTS signals show major instability upon annealing. In this section, we explore this instability in more detail.

8.8.1 Room temperature annealing

A 25 Ω -cm Cz p-Si sample was hydrogenated and kept in the dark at room temperature. An Arrhenius analysis was carried out with intervals of approximately one week.

The results clearly demonstrated that the kinetics of the fill pulse phase process are significantly altered by room temperature annealing. At certain measurement temperatures, the change in time constant was larger than a factor of 5 after a few weeks. The instability is in line with the difference in the Arrhenius behavior observed between various samples prepared from the same material (Figure 8.7). It is, however, extremely difficult to extract any systematics in the observed changes. There is a trend that the process speeds up upon room temperature annealing but in general the Arrhenius curves behave in a rather irregular way. No significant change of the signal amplitude was observed after room temperature annealing.

8.8.2 Isochronal annealing

Isochronal annealing of a 22 Ω -cm FZ p-Si sample has been carried out. The sample was annealed for periods of 30 minutes in a nitrogen ambient between temperatures 50 $^{\circ}\text{C}$ and 300 $^{\circ}\text{C}$ in steps of 25 $^{\circ}\text{C}$. Similar to the isothermal annealing at room temperature, the kinetics of the process were altered as a result of the annealing. Further, the amplitude of the signal changed significantly after annealing above 100 $^{\circ}\text{C}$. Figure 8.11 depicts the relative signal amplitude $dC_{\text{RB}}/C_{\text{RB}}$ of the reverse bias phase process as a function of annealing temperature for four different values of the reverse bias. It is extremely difficult to interpret the annealing data as the space charge region and the electric field distribution change upon annealing above 100 $^{\circ}\text{C}$, where the boron-hydrogen complexes become unstable. As established above, the electric field strength has a significant effect on the signal amplitude. The important conclusion from the annealing data is that the effect still exists after annealing at 300 $^{\circ}\text{C}$. Further, it appears that the signal becomes relatively stronger closer to the sample surface than deeper in the sample as a function of annealing temperature.

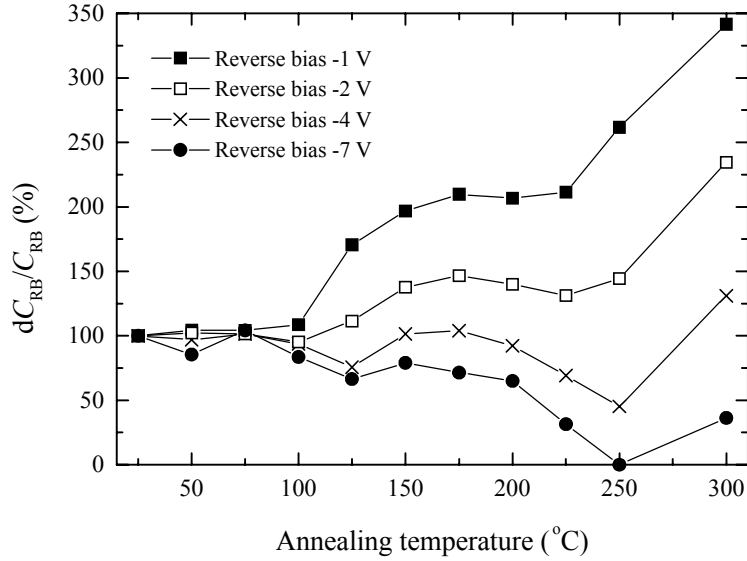


Figure 8.11: Isochronal (30 minutes) annealing data obtained in a 22 Ω -cm FZ p-Si sample. The relative signal amplitude dC_{RB}/C_{RB} of the reverse bias phase process is given for four different values of the reverse bias as a function of annealing temperature. The amplitudes are normalized to the values obtained before annealing.

8.9 Microscopic identity of the polarizing defect

The experimental results presented in this chapter form some foundation for our interpretation of the unusual capacitance changes as a localized polarization of a hydrogen-related complex under the influence of an electric field. However, from the results present above, we cannot reach any definite conclusion in relation to the microscopic identity of the polarizing complex. The data indicate that the defect is not related to chemical impurities other than hydrogen. Firstly, comparable signals were observed in 25 Ω -cm Cz p-Si and 22 Ω -cm FZ p-Si, indicating no relation to oxygen. Secondly, a successful numerical modeling of the DLTS data required a rather large defect concentration, e.g. much larger than the background doping concentration of the material. Below, we discuss two preliminary ideas regarding the identity of the polarizing complex.

8.9.1 The interstitial hydrogen molecule

The interstitial hydrogen molecule is known to exist in silicon hydrogenated by indiffusion from a hydrogen gas at high temperature and by exposure to a remote plasma (see Chapter 4). It seems probable that the complex can also be formed in large concentrations in chemically etched silicon. The molecule is located close to a T-site in the silicon lattice. Recent calculations [Estreicher 2001] show that, at temperatures $T > 0$ K, the center of mass of the molecule moves around at a very fast pace and the average position of the center of mass changes with temperature. Each of the atoms in the molecule carries a small positive charge. It seems probable that an external electric field can also change the average position of the center of mass and hereby induce a charge movement. The effect studied in the present work may be related to a movement of the center of mass of the hydrogen molecule along the axis of the externally applied electric field. The saturation of the charge movement with field strength can be explained by the center of mass approaching the walls of the tetrahedral cage. The presence of the effect after annealing at 300 °C is consistent with interstitial hydrogen molecules, which can exist in the bulk up to temperatures of ~ 300 -350 °C [Markevich 2000a]. The main problem with the above suggestion is the size of the dipole moment associated with the molecule, which is significantly smaller than required to produce the observed effect. Further, the unusual capacitance transients were not seen in hydrogenated n-type silicon, where most observations of interstitial hydrogen molecules have been carried out. Finally, the instability of the kinetics upon room temperature annealing is not addressed by this interpretation.

8.9.2 The H_2^* defect

The H_2^* defect is a metastable structure that consists of a positively charged hydrogen atom close to a bond-center site and a negatively charged hydrogen atom close to an anti-bonding site. The existence of H_2^* has been predicted by theory [Chang 1989] and subsequently confirmed experimentally [Holbeck 1993], [Bech 1994]. It is possible that

the polarization studied in the present work is related to field-induced jumps of H^+ between bond-center sites surrounding its H^- counterpart located at a fixed anti-bonding site. The charge movement associated with such jumps are on the order of Ångströms. However, it seems unlikely that the H_2^* defect is formed in large concentrations as a result of room temperature chemical etching. Further, the defect is unstable above ~ 200 °C [Bech 1994], which is inconsistent with the isochronal annealing data.

8.10 Summary

We have observed capacitance changes in p-type silicon of opposite sign to those usually observed by majority carrier DLTS. That is, the capacitance decreases during the reverse bias phase of the DLTS pulse train. The effect is related to hydrogen and cannot be explained by carrier emission from electronic energy levels in the band gap. A detailed analysis of formation conditions, kinetics, signal amplitude and annealing behavior of the effect has been carried out. The experimental data are reasonably well explained by a model of localized polarization of a hydrogen-related defect centre under the influence of an electric field. A significant instability in the kinetics of the effect has not been addressed. Further, the exact microscopic identity of the hydrogen-related defect remains unclear. It is unlikely that chemical impurities other than hydrogen are involved in the complex.

Chapter 9

Conclusions

The experimental results obtained in this work were presented and discussed in Chapters 4, 5, 6, 7 and 8. These chapters focused on somewhat separate topics and conclusions were given for each individual case. In this chapter, an overview of the thesis is given.

Our results demonstrate the ability of hydrogen to interact with existing defects in crystalline silicon. In the case of the iso-valent defect of substitutional carbon, the interactions with hydrogen form a stable electron trap with a level at $E_c - 0.155$ eV. Contrary to previous work, the trap level has been assigned to a single acceptor. The complex was identified either as a structure with hydrogen bond-centered next to a substitutional carbon atom or a structure with hydrogen anti-bonded to the carbon atom. It was concluded that the interactions of isolated atomic hydrogen with substitutional carbon and resulting formation of the hydrogen-carbon pair convert the defect from a negative-U system to a positive-U system. In the case of radiation induced defects, the interactions with hydrogen result in the formation of electrically active as well as electrically inert hydrogen-related complexes. This illustrates the general trend that hydrogen can be trapped at dangling bonds or break Si-Si bonds to form Si-H bonds, hence shifting the electronic energy levels within the band gap or completely removing the electrical activity of the original structure. These transformations were examined in detail for the vacancy-oxygen complex VO and the divacancy V_2 . It was established

that the VOH defect introduces an acceptor level at $E_c - 0.312$ eV and a donor level at $E_v + 0.263$ eV, while the VOH₂ defect is electrically inert. The V₂H defect has an acceptor level at $E_c - 0.415$ eV, close to the acceptor level of the divacancy itself. Further, higher order V₂H_{*n*} complexes can be formed by stronger hydrogenation. It was proposed that some of these complexes are electrically active, possibly with levels located in the mid-gap region in which several hydrogen-related levels are observed. It is a task for future Laplace transform DLTS studies to resolve, characterize and identify these mid-gap levels, which generally are rather poorly understood.

The thesis also deals with other forms of hydrogen in plasma treated and chemically etched silicon. After room temperature remote plasma treatment of n-type silicon, the hydrogen mainly exists in the form of hydrogen-dopant complexes beyond ~ 0.3 μm , passivating more than 50% of the background carriers into a depth of at least 1 μm . The hydrogen incorporation into the bulk of lowly doped FZ n-type silicon is strongly increased with treatment temperature up to ~ 200 °C. It was proposed that the bulk hydrogen mainly exists in the form of interstitial molecules. Treatments carried out around ~ 100 °C introduce two hydrogen-related acceptor levels into the band gap located at $E_c - 0.114$ eV and $E_c - 0.522$ eV. The identities of these levels have not been established. Chemical etching and plasma treatment of p-type silicon form a hydrogen-related defect that gives rise to capacitance changes of opposite sign to those usually observed by majority carrier DLTS. The effect cannot be explained by carrier emission from electronic energy levels in the band gap. A detailed analysis of formation conditions, kinetics, signal amplitude and annealing behavior of the effect has been carried out. The experimental data are reasonably well explained by a model of a localized polarization of a hydrogen-related defect under the influence of an electric field. The microscopic identity of the hydrogen-related defect remains unclear. Further work is currently in progress in order to establish the exact origin of this intriguing effect.

The technique of uniaxial stress combined with Laplace transform DLTS has formed an important part of the thesis. This work is part of the first detailed piezospectro-

scopic analysis of defects in semiconductors carried out by means of DLTS. We have gained considerable experience in using this technique and have developed an experimental approach that allows examination of several properties of a given defect centre, including its symmetry, piezospectroscopic tensor and reorientation kinetics.

Perhaps the most promising aspect of uniaxial stress measurements is the possibility to correlate data from various experimental and theoretical techniques. It is a classical problem in defect characterization to link observations from different experimental techniques as a given sample rarely is appropriate for more than one of these. Uniaxial stress measurements allow such a correlation to be made, hence forming an efficient tool for defect identification. A prime example is the stable configuration of the VO complex for which the piezospectroscopic tensors obtained in the present work by Laplace transform DLTS were in excellent agreement with EPR data. In the case of the hydrogen-carbon pair, the agreement between experimental and theoretical piezospectroscopic parameters has allowed us to identify the complex as a structure with either hydrogen bond-centered next to a substitutional carbon atom or a structure with hydrogen anti-bonded to the carbon atom. Unfortunately, it was not possible to distinguish reliably between the two configurations. Similar comparisons were essential in order to explain the effective symmetries observed for the two charge states of the VOH complex with static monoclinic-I symmetry. The acceptor level displays an effective orthorhombic-I symmetry due to fast thermally activated jumps of the hydrogen atom in the mirror plane of the defect, as determined by EPR. Similar, the donor level displays an effective cubic symmetry due to fast thermally activated jumps of both hydrogen and oxygen at the measurement temperature, in agreement with theoretical calculations. Thus, all the above examples illustrate that uniaxial stress combined with Laplace transform DLTS forms an efficient tool for defect identification by comparison to data obtained by other experimental techniques and theoretical modeling.

Additional information can be obtained from the defect reorientation kinetics. This work has established that, in many cases, the reorientation barrier depends strongly on the charge state of the defect. For the hydrogen-carbon pair, the energy barrier for

the reorientation is significantly larger in the neutral charge state than in the negative charge. For the VO and VOH complexes, the reorientation barrier systematically increases as more electrons are bound to the defect. Further, in the case of the VO complex, the stress dependence of the barrier allowed us to conclude that the saddle point on the reorientation trajectory has a trigonal symmetry with the oxygen atom attached to three nearest neighbor silicon atoms. These characteristics are important for the understanding of the defect dynamics and diffusion properties.

The stress measurements of the VO complex showed that the capture process for the low frequency branch in the $\langle 100 \rangle$ stress direction depends strongly on the magnitude of the applied stress. This remarkable conclusion was reached very recently and its implications has not been covered in details in the thesis. Further, the possibility of stress-dependent capture has, to some extent, been overlooked in the other stress studies. The preliminary observation for the VO complex has shown the importance of directly studying the capture process during uniaxial stress DLTS measurements. Future detailed analysis of the stress dependence of the capture process has the potential to provide insight into the capture mechanism, which generally is rather poorly understood.

The use of uniaxial stress combined with Laplace transform DLTS is still young and we see a lot of potential in the technique. A number of future studies are planned as a collaboration between UMIST and the semiconductor groups at the universities in Aarhus, Warsaw and Exeter. In relation to this thesis, future work includes analysis of the alignment data for the VOH acceptor level and detailed capture measurements for the VO complex for all directions of stress. Further, studies of the platinum-dihydrogen complex in silicon and several complexes in Ge and SiGe are subject for piezospectroscopic investigations.

Appendix A

Piezospectroscopic formulas for a trigonal defect centre

The aim of this appendix is to exemplify some of the procedures and formulas described in the piezospectroscopic theory in Chapter 2. Our chosen example is a trigonal defect centre in a silicon crystal stressed along the three major crystallographic directions, $\langle 100 \rangle$, $\langle 110 \rangle$ and $\langle 111 \rangle$. A similar approach to the one described here can be used for defects belonging to other symmetry systems.

For a trigonal defect centre, the form of the strain-energy piezospectroscopic tensor in (x, y, z) coordinates is given by:

$$\bar{\mathbf{B}}^{(x,y,z)} = \begin{bmatrix} B_1 & B_2 & B_2 \\ B_2 & B_1 & B_2 \\ B_2 & B_2 & B_1 \end{bmatrix}. \quad (\text{A.1})$$

The eigenvalues are obtained as $B_1 - B_2$, $B_1 - B_2$ and $2B_2 + B_1$ with corresponding eigenvectors $[\bar{1}10]$, $[11\bar{2}]$ and $[111]$, respectively. Thus, the piezospectroscopic tensor in the coordinate system defined by the principal axes $[\bar{1}10]$, $[11\bar{2}]$ and $[111]$ is given by:

$$\bar{\mathbf{B}}^{princ} = \begin{bmatrix} B_1 - B_2 & 0 & 0 \\ 0 & B_1 - B_2 & 0 \\ 0 & 0 & 2B_2 + B_1 \end{bmatrix}. \quad (\text{A.2})$$

The trigonal defect has four equivalent orientations in the unstrained silicon lattice corresponding to the four possible trigonal axes. This degeneracy is partly lifted by the application of a uniaxial stress $P > 0$ to the silicon crystal. Below, we consider the number of non-equivalent orientations and calculate the corresponding shifts of the total energy for stresses applied along the three major crystallographic directions, $\langle 100 \rangle$, $\langle 110 \rangle$ and $\langle 111 \rangle$. In calculating the energy shifts, we use the (x, y, z) coordinate system but identical results are obtained by using the coordinate system defined by the principal axes.

(a) **The $\langle 100 \rangle$ stress direction**

All four orientations are still equivalent. The angle between the trigonal axis and the stress direction is 54.7° . We denote by $\Delta E_4^{\langle 100 \rangle}$ the shift of the total energy. We assume that the trigonal axis is along the $[111]$ direction and that the stress is applied along the $[100]$ direction. The stress vector is obtained from equation (2.17) as:

$$\boldsymbol{\sigma}^{[100]} = -P(1, 0, 0, 0, 0, 0), \quad (\text{A.3})$$

which, by use of equation (2.22), yields the strain vector:

$$\boldsymbol{\varepsilon}^{[100]} = -P(s_{11}, s_{12}, s_{12}, 0, 0, 0). \quad (\text{A.4})$$

We calculate the shift of the total energy per unit stress from equation (2.23):

$$\Delta E_4^{\langle 100 \rangle} / P = \sum_{i,j} B_{ij}^{(x,y,z)} \varepsilon_{ij}^{[100]} / P = -B_1(s_{11} + 2s_{12}). \quad (\text{A.5})$$

(b) **The $\langle 111 \rangle$ stress direction**

There are two non-equivalent orientations of the centre relative to the stress. For one of the four orientations, the stress is along the trigonal axis, while for the remaining three orientations, the stress is at an angle of 70.5° to the trigonal axis. Thus, the two non-equivalent orientations have degeneracy 1 and 3, respectively. We denote by $\Delta E_1^{\langle 111 \rangle}$ and $\Delta E_3^{\langle 111 \rangle}$ the corresponding shifts of the total energy. We assume that the trigonal axis is along the $[111]$ direction and that the stress is applied along the

[111] direction for calculation of $\Delta E_1^{<111>}$ and along the $[\bar{1}11]$ direction for calculation of $\Delta E_3^{<111>}$. The stress vectors are obtained as:

$$\boldsymbol{\sigma}^{[111]} = -\frac{1}{3}P(1, 1, 1, 1, 1, 1), \quad (\text{A.6})$$

$$\boldsymbol{\sigma}^{[\bar{1}11]} = -\frac{1}{3}P(1, 1, 1, 1, -1, -1), \quad (\text{A.7})$$

which yield the strain vectors:

$$\boldsymbol{\varepsilon}^{[111]} = -\frac{1}{3}P(s_{11} + 2s_{12}, s_{11} + 2s_{12}, s_{11} + 2s_{12}, s_{44}, s_{44}, s_{44}), \quad (\text{A.8})$$

$$\boldsymbol{\varepsilon}^{[\bar{1}11]} = -\frac{1}{3}P(s_{11} + 2s_{12}, s_{11} + 2s_{12}, s_{11} + 2s_{12}, s_{44}, -s_{44}, -s_{44}). \quad (\text{A.9})$$

We calculate the shifts of the total energy per unit stress from equation (2.23):

$$\Delta E_1^{<111>}/P = \sum_{i,j} B_{ij}^{(x,y,z)} \varepsilon_{ij}^{[111]}/P = -B_1(s_{11} + 2s_{12}) - B_2s_{44}, \quad (\text{A.10})$$

$$\Delta E_3^{<111>}/P = \sum_{i,j} B_{ij}^{(x,y,z)} \varepsilon_{ij}^{[\bar{1}11]}/P = -B_1(s_{11} + 2s_{12}) + \frac{1}{3}B_2s_{44}. \quad (\text{A.11})$$

The energy splitting per unit stress is given by:

$$(\Delta E_1^{<111>} - \Delta E_3^{<111>})/P = -\frac{4}{3}B_2s_{44}. \quad (\text{A.12})$$

(c) The $<110>$ stress direction

There are two non-equivalent orientations of the centre relative to the stress. For two of the four orientations, the stress is at an angle of 35.3° to the trigonal axis, while for the remaining two orientations, the angle is 90° . Thus, the two non-equivalent orientations both have degeneracy 2. We denote by $\Delta E_{2A}^{<110>}$ and $\Delta E_{2B}^{<110>}$ the corresponding shifts of the total energy. We assume that the trigonal axis is along the [111] direction and that the stress is applied along the [110] direction for calculation of $\Delta E_{2A}^{<110>}$ and along the $[\bar{1}10]$ direction for calculation of $\Delta E_{2B}^{<110>}$. The stress vectors are obtained as:

$$\boldsymbol{\sigma}^{[110]} = -\frac{1}{2}P(1, 1, 0, 0, 0, 1), \quad (\text{A.13})$$

$$\boldsymbol{\sigma}^{[\bar{1}10]} = -\frac{1}{2}P(1, 1, 0, 0, 0, -1), \quad (\text{A.14})$$

which yield the strain vectors:

$$\boldsymbol{\epsilon}^{[110]} = -\frac{1}{2}P(s_{11} + s_{12}, s_{11} + s_{12}, 2s_{12}, 0, 0, s_{44}), \quad (\text{A.15})$$

$$\boldsymbol{\epsilon}^{\overline{[110]}} = -\frac{1}{2}P(s_{11} + s_{12}, s_{11} + s_{12}, 2s_{12}, 0, 0, -s_{44}). \quad (\text{A.16})$$

We calculate the shifts of the total energy per unit stress from equation (2.23):

$$\Delta E_{2A}^{<110>} / P = \sum_{i,j} B_{ij}^{(x,y,z)} \epsilon_{ij}^{[110]} / P = -B_1(s_{11} + 2s_{12}) - \frac{1}{2}B_2s_{44}, \quad (\text{A.17})$$

$$\Delta E_{2B}^{<110>} / P = \sum_{i,j} B_{ij}^{(x,y,z)} \epsilon_{ij}^{\overline{[110]}} / P = -B_1(s_{11} + 2s_{12}) + \frac{1}{2}B_2s_{44}. \quad (\text{A.18})$$

The energy splitting per unit stress is given by:

$$(\Delta E_{2A}^{<110>} - \Delta E_{2B}^{<110>})/P = -B_2s_{44}. \quad (\text{A.19})$$

Appendix B

List of symbols

| | |
|------------------------------|--|
| A | Diode area |
| A^* | Effective Richardson constant |
| $\bar{\mathbf{B}}$ | Piezospectroscopic tensor |
| B_i, B_{ij} | Piezospectroscopic tensor components |
| c_n, c_p | Electron and hole capture rates |
| C | Capacitance |
| e | Elementary charge |
| e_n, e_p | Electron and hole emission rates |
| E | Energy |
| E_c, E_v | Conduction and valence band energy extrema |
| E_F | Fermi energy level |
| E_{Fn}, E_{Fp} | Quasi-Fermi energy levels for n-type and p-type semiconductors |
| E_g | Band gap energy |
| E_n^a, E_p^a | Activation energies for electron and hole emission |
| E_t | Trap energy level |
| $E_{\sigma_n}, E_{\sigma_p}$ | Energy barriers for electron and hole capture |
| f_{FD} | Fermi-Dirac distribution function |
| g_0, g_1 | Degeneracy factors for empty and filled traps |

| | |
|--|---|
| G | Gibbs free energy |
| H | Enthalpy |
| I | Current |
| \mathbf{k} | Wave vector |
| $k_{A \rightarrow B}$ | Rate for jump from configuration A to configuration B |
| k_B | Boltzmann's constant |
| L_D | Debye length |
| m | Free electron mass |
| m_c^*, m_v^* | Effective electron and hole masses |
| n_c, p_v | Free electron and hole densities |
| n_t | Density of filled traps |
| N_A, N_B | Densities of defects in configurations A and B |
| N_c, P_v | Effective densities of states in conduction and valence bands |
| N_d, N_a | Donor and acceptor densities |
| N_t | Trap density |
| P | Stress |
| q | Charge of defect |
| Q | Fixed charge in space charge region |
| s_{ijkl}, s_{ij} | Crystal compliances |
| S | Entropy |
| t | Time |
| T | Temperature |
| $\langle v_n \rangle, \langle v_p \rangle$ | Average thermal velocities of electrons and holes |
| V | Voltage |
| V_{bi} | Built-in potential |
| V_F, V_R | Forward and reverse bias |
| W | Space charge width |
| x | Distance |

| | |
|------------------------------------|---|
| $\alpha_{A,B}$ | Stress coefficient for energy difference between configurations A and B |
| $\beta_{A,B}$ | Stress coefficient for energy barrier between configurations A and B |
| $\boldsymbol{\varepsilon}$ | Strain vector |
| ε_{ij} | Strain tensor/vector components |
| ε_s | Semiconductor dielectric constant |
| \mathcal{E} | Electric field |
| ϕ_{Bn}, ϕ_{Bp} | Schottky barrier heights for n-type and p-type semiconductors |
| $e\phi_m, e\phi_s$ | Metal and semiconductor work functions |
| λ | Lambda width |
| $e\chi_n, e\chi_p$ | Electron and hole affinities |
| ρ | Space charge density |
| $\boldsymbol{\sigma}$ | Stress vector |
| σ_{ij} | Stress tensor/vector components |
| σ_n, σ_p | Electron and hole capture cross sections |
| σ_n^a, σ_p^a | Apparent electron and hole capture cross sections |
| $\sigma_n^\infty, \sigma_p^\infty$ | Electron and hole capture cross sections in limit $T \rightarrow \infty$ |
| τ | Time constant |
| ω | Electric field parameter |

Appendix C

List of publications

K. Bonde Nielsen, L. Dobaczewski, K. Gościński, R. Bendesen, **O. Andersen** and B. Bech Nielsen. Deep levels of vacancy-hydrogen centers in silicon studied by Laplace DLTS. *Physica B* **273-274** 167-170, 1999.

L. Dobaczewski, K. Bonde Nielsen, K. Gościński and **O. Andersen**. Hydrogen and its complexes in silicon. *Institute of Physics Polish Academy of Sciences, Acta Physica Polonica A* **98** (3) 231-239, 2000.

A. R. Peaker, L. Dobaczewski, **O. Andersen**, L. Rubaldo, I. D. Hawkins, K. Bonde Nielsen and J. H. Evans-Freeman. Silicon defect characterization by high resolution Laplace deep level transient spectroscopy. In *Electrochemical Society Proceedings Vol. 2000-17* p. 549, 2000.

A. R. Peaker, L. Dobaczewski, I. D. Hawkins, J. H. Evans-Freeman, **O. Andersen**, L. Rubaldo and K. Bonde Nielsen. Hydrogen complexes and implant damage in silicon, the role of high resolution Laplace deep level transient spectroscopy, a new tool to understand defects in silicon. In *Proceedings of 3rd International Symposium on Advanced Science and Technology of Silicon Materials* p. 437, 2000.

L. Dobaczewski, K. Bonde Nielsen, **O. Andersen**, L. Rubaldo, K. Gościński and A. R.

Peaker. Defect reconfiguration as a precursor for diffusion. In *Proceedings of the 25th International Conference on the Physics of Semiconductors* p. 1427, 2001.

O. Andersen, A. R. Peaker, L. Dobaczewski and J. H. Evans-Freeman. Laplace DLTS studies of hydrogen interaction with the vacancy-oxygen centre in silicon. Submitted for *Third Conference on Postgraduate Research in Electronics, Photonics, Communications and Software*, 2001.

A. R. Peaker, J. H. Evans-Freeman, L. Dobaczewski, V. P. Markevich, **O. Andersen**, L. Rubaldo, P. Y. Y. Kan, I. D. Hawkins, K. Gościński and K. Bonde Nielsen. High resolution Laplace deep level transient spectroscopy - a new tool to study implant damage in silicon. In *Electrochemical Society Proceedings Vol. 2001-29* p. 166, 2001.

O. Andersen, L. Dobaczewski, A. R. Peaker, K. Bonde Nielsen, B. Hourahine, R. Jones, P. R. Briddon and S. Öberg. Piezospectroscopic analysis of the hydrogen-carbon complexes in silicon. *Physica B* **308-310** 139-142, 2001.

V. P. Markevich, **O. Andersen**, I. F. Medvedeva, J. H. Evans-Freeman, I. D. Hawkins, L. I. Murin, L. Dobaczewski and A. R. Peaker. Defect reactions associated with the dissociation of the phosphorous-vacancy pair in silicon. *Physica B* **308-310** 513-516, 2001.

L. Dobaczewski, K. Gościński, Z. R. Żytkiewicz, K. Bonde Nielsen, L. Rubaldo, **O. Andersen** and A. R. Peaker. Piezosopic deep-level transient spectroscopy studies of the silicon divacancy. *Physical Review B* **65** (11) 113203/1-4, 2002.

O. Andersen, A. R. Peaker, L. Dobaczewski, K. Bonde Nielsen, B. Hourahine, R. Jones, P. R. Briddon and S. Öberg. Electrical activity of carbon-hydrogen centers in Si. *Physical Review B* **66** 235205/1-8, 2002.

L. Dobaczewski, **O. Andersen**, L. Rubaldo, V. P. Markevich, A. R. Peaker and K.

Bonde Nielsen. Saddle point for oxygen reorientation in the vicinity of a silicon vacancy.
Submitted for *Physical Review B*, 2002.

Bibliography

- [Andersen 2000] O. Andersen. *Identifikation og Karakterisering af det Elektrisk Aktive VOH Center i Si med Anvendelse af Laplace DLTS*. Master's thesis, Institute of Physics and Astronomy, University of Aarhus, 2000.
- [Andersen 2001] O. Andersen, L. Dobaczewski, A. R. Peaker, K. Bonde Nielsen, B. Hourahine, R. Jones, P. R. Briddon and S. Öberg. Piezospectroscopic analysis of the hydrogen-carbon complexes in silicon. *Physica B* **308-310** 139-142, 2001.
- [Andersen 2002] O. Andersen, A. R. Peaker, L. Dobaczewski, K. Bonde Nielsen, B. Hourahine, R. Jones, P. R. Briddon and S. Öberg. Electrical activity of carbon-hydrogen centers in Si. *Physical Review B* **66** 235205/1-8, 2002.
- [Ashcroft 1976] N. W. Ashcroft and N. D. Mermin. *Solid State Physics*, international edition. Saunders College Publishing, Fort Worth, 1976.
- [Bech 1994] B. Bech Nielsen, J. D. Holbech, R. Jones, P. Sitch and S. Öberg. Observation and theory of the H_2^* defect in silicon. *Materials Science Forum Vols. 143-147* 845-852, 1994.
- [Bech 1997] B. Bech Nielsen, P. Johannesen, P. Stallinga, K. Bonde Nielsen and J. R. Byberg. Identification of the silicon vacancy containing a single hydrogen atom by EPR. *Physical Review Letters* **79** (8) 1507-1510, 1997.

- [Blood 1992] P. Blood and J. W. Orton. *The Electrical Characterization of Semiconductors: Majority Carriers and Electron States*. Academic Press, London, 1992.
- [Bonde 1999a] K. Bonde Nielsen, L. Dobaczewski, K. Gościński, R. Bendesen, O. Andersen and B. Bech Nielsen. Deep levels of vacancy-hydrogen centers in silicon studied by Laplace DLTS. *Physica B* **273-274** 167-170, 1999.
- [Bonde 1999b] K. Bonde Nielsen, B. Bech Nielsen, J. Hansen, E. Andersen and J. U. Andersen. Bond-centered hydrogen in silicon studied by *in situ* deep-level transient spectroscopy. *Physical Review B* **60** (3) 1716-1728, 1999.
- [Bonde 2001] K. Bonde Nielsen, L. Dobaczewski, S. Søgård and B. Bech Nielsen. Electronic levels of isolated and oxygen-perturbed hydrogen in silicon and migration of hydrogen. *Physica B* **308-310** 134-138, 2001.
- [Brotherton 1982] S. D. Brotherton and P. Bradley. Defect production and lifetime control in electron and γ -irradiated silicon. *Journal of Applied Physics* **53** (8) 5720-5732, 1982.
- [Chadi 1996] D. J. Chadi. Core structure of thermal donors in silicon. *Physical Review Letters* **77** (5) 861-865, 1996.
- [Chang 1989] K. J. Chang and D. J. Chadi. Diatomic-hydrogen-complex diffusion and self-trapping in crystalline silicon. *Physical Review Letters* **62** (8) 937-940, 1989.
- [Cheng 1994] Y. M. Cheng and M. Stavola. Non-Arrhenius reorientation kinetics for the B-H complex in Si: Evidence for thermally assisted tunneling. *Physical Review Letters* **73** (25) 3419-3422, 1994.
- [Corbett 1961] J. W. Corbett, G. D. Watkins, M. Chrenko and R. S. McDonald. Defects in irradiated silicon. II. Infrared absorption of the Si- A center. *Physical Review* **121** (4) 1015-1022, 1961.

- [Coutinho 2000] J. Coutinho, R. Jones, P. R. Briddon and S. Öberg. Oxygen and dioxygen centers in Si and Ge: Density-functional calculations. *Physical Review B* **62** (16) 10824-10840, 2000.
- [Coutinho] J. Coutinho. Private communications, 2002.
- [Csaszar 1994] W. Csaszar and A. L. Endrös. Anomalous electronic properties of a hydrogen-related deep donor in *c*-Si. *Physical Review Letters* **73** (2) 312-315, 1994.
- [Davies 1994] G. Davies and R. C. Newman. Carbon in monocrystalline silicon. In *Handbook on Semiconductors*, completely revised edition, edited by T. S. Moss, chapter 21 pp. 1557-1635, Elsevier Science, 1994.
- [Deixler 1998] P. Deixler, J. Terry, I. D. Hawkins, J. H. Evans-Freeman, A. R. Peaker, L. Rubaldo, D. K. Maude, J. C. Portal, L. Dobaczewski, K. Bonde Nielsen, A. Nylandsted Larsen and A. Mesli. Laplace-transform deep-level transient spectroscopy studies of the G4 gold-hydrogen complex in silicon. *Applied Physics Letters* **73** (21) 3126-3128, 1998.
- [DeLeo 1984] G. G. DeLeo, W. Beall Fowler and G. D. Watkins. Theory of off-center impurities in silicon: Substitutional nitrogen and oxygen. *Physical Review B* **29** (6) 3193-3207, 1984.
- [Dobaczewski 1994] L. Dobaczewski, P. Kaczor, I. D. Hawkins and A. R. Peaker. Laplace transform deep-level transient spectroscopic studies of defects in semiconductors. *Journal of Applied Physics* **76** (1) 194-198, 1994.
- [Dobaczewski 1999] L. Dobaczewski, K. Bonde Nielsen, K. Gościński, A. R. Peaker and A. Nylandsted Larsen. Site preference next to germanium atom of gold, platinum impurities in SiGe alloy. *Physica B* **273-274** 620-623, 1999.
- [Endrös 1989] A. Endrös. Charge-state-dependent hydrogen-carbon-related deep donor in crystalline silicon. *Physical Review Letters* **63** (1) 70-73, 1989.

- [Endrös 1992] A. L. Endrös, W. Krühler and F. Koch. Electronic properties of the hydrogen-carbon complex in crystalline silicon. *Journal of Applied Physics* **72** (6) 2264-2271, 1992.
- [Estreicher 1994] S. K. Estreicher, M. A. Roberson and D. M. Maric. Hydrogen and hydrogen dimers in c-C, Si, Ge, and α -Sn. *Physical Review B* **50** (23) 17018-17027, 1994.
- [Estreicher 1995] S. K. Estreicher. Hydrogen-related defects in crystalline semiconductors: A theorist's perspective. *Materials Science and Engineering* **R 14** 319-412, 1995.
- [Estreicher 2001] S. K. Estreicher, K. Wells, P. A. Fedders and P. Ordejón. Dynamics of interstitial hydrogen molecules in crystalline silicon. *Journal of Physics: Condensed Matter* **13** 6271-6283, 2001.
- [Evwaraye 1976] A. O. Evwaraye and E. Sun. Electron-irradiated-induced divacancy in lightly doped silicon. *Journal of Applied Physics* **47** (9) 3776-3780, 1976.
- [Fatima 1999] S. Fatima, C. Jagadish, J. Lalita, B. G. Svensson and A. Hallén. Hydrogen interaction with implantation induced point defects in p-type silicon. *Journal of Applied Physics* **85** (5) 2562-2567, 1999.
- [Feklisova 1997] O. W. Feklisova and N. A. Yarykin. Transformation of deep-level spectrum of irradiated silicon due to hydrogenation under wet chemical etching. *Semiconductor Science and Technology* **12** 742-749, 1997.
- [Feklisova 1999] O. Feklisova, N. Yarykin, E. Yakimov and J. Weber. Hydrogen interaction with defects in electron-irradiated silicon. *Physica B* **273-274** 235-238, 1999.

- [Feklisova 2001] O. Feklisova, N. Yarykin, E. B. Yakimov and J. Weber. On the nature of hydrogen-related centers in p-type irradiated silicon. *Physica B* **308-310** 210-212, 2001.
- [Fukuda 1999] K. Fukuda, Y. Kamiura and Y. Yamashita. Effects of charge state on stress-induced alignment and relaxation of a hydrogen-carbon complex in silicon. *Physica B* **273-274** 184-187, 1999.
- [Fukuda 2001] K. Fukuda, Y. Kamiura, Y. Yamashita and T. Ishiyama. Effect of uniaxial stress on the electronic state of the hydrogen-carbon complex in silicon. *Physica B* **302-303** 227-232, 2001.
- [Fukata 1997] N. Fukata, S. Sasaki, K. Murakami, K. Ishioka, K. G. Nakamura, M. Kitajima, S. Fujimura, J. Kikuchi and H. Haneda. Hydrogen molecules and hydrogen-related defects in crystalline silicon. *Physical Review B* **56** (11) 6642-6647, 1997.
- [Ganichev 2000] S. D. Ganichev, E. Ziemann, W. Prettl, I. N. Yassievich, A. A. Istratov and E. R. Weber. Distinction between the Poole-Frenkel and tunneling models of electric-field-stimulated carrier emission from deep levels in semiconductors. *Physical Review B* **61** (15) 10361-10365, 2000.
- [Gorelkinskii 1996] Y. V. Gorelkinskii and N. N. Nevinnyi. EPR of interstitial hydrogen in silicon: Uniaxial stress experiments. *Materials Science and Engineering* **B36** 133-137, 1996.
- [Green 1990] M. A. Green. Intrinsic concentration, effective densities of states, and effective mass in silicon. *Journal of Applied Physics* **67** 2944-2954, 1990.
- [Hallén 1996] A. Hallén, N. Keskitalo, F. Masszi and V. Nágl. Lifetime in proton irradiated silicon. *Journal of Applied Physics* **79** (8) 3906-3914, 1996.
- [Hamilton] B. Hamilton. Private communications, 2002.

- [Hartke 1968] J. L. Hartke. The three-dimensional Poole-Frenkel effect. *Journal of Applied Physics* **39** 4871-4873, 1968.
- [Heiser 1998] T. Heiser and E. R. Weber. Transient ion-drift-induced capacitance signals in semiconductors. *Physical Review B* **58** (7) 3893-3903, 1998.
- [Henry 1977] C. H. Henry and D. V. Lang. Nonradiative capture and recombination by multiphonon emission in GaAs and GaP. *Physical Review B* **15** (2) 989-1016, 1977.
- [Herring 2001] C. Herring, N. M. Johnson and C. G. Van de Walle. Energy levels of isolated interstitial hydrogen in silicon. *Physical Review B* **64** 125209/1-27, 2001.
- [Hoffmann 2000] L. Hoffmann, E. V. Lavrov, B. Bech Nielsen, B. Hourahine, R. Jones, S. Öberg and P. R. Briddon. Weakly bound carbon-hydrogen complex in silicon. *Physical Review B* **61** (24) 16659-16666, 2000.
- [Holbech 1993] J. D. Holbech, B. Bech Nielsen, R. Jones, P. Sitch and S. Öberg. H_2^* defect in crystalline silicon. *Physical Review Letters* **71** (6) 875-878, 1993.
- [Hourahine 1998] B. Hourahine, R. Jones, S. Öberg, R. C. Newman, P. R. Briddon and E. Roduner. Hydrogen molecules in silicon located at interstitial sites and trapped in voids. *Physical Review B* **57** (20) 12666-12669, 1998.
- [Hüppi 1990] M. W. Hüppi. Proton irradiation of silicon: Complete electrical characterization of the induced recombination centers. *Journal of Applied Physics* **68** (6) 2702-2707, 1990.
- [Irmscher 1984] K. Irmscher, H. Klose and K. Maass. Hydrogen-related deep levels in proton-bombarded silicon. *Journal of Physics C* **17** 6317-6329, 1984.
- [Istratov 1999] A. A. Istratov and O. F. Vyvenko. Exponential analysis in physical phenomena. *Review of Scientific Instruments* **70** (2) 1233-1257, 1999.

- [Johannesen 2000] P. Johannesen, B. B. Nielsen and J. R. Byberg. Identification of the vacancy-oxygen defect containing a single hydrogen atom in crystalline silicon. *Physical Review B* **61** (7) 4659-4666, 2000.
- [Johnson 1985a] N. M. Johnson. Mechanism for hydrogen compensation of shallow-acceptor impurities in single-crystal silicon. *Physical Review B* **31** (8) 5525-5528, 1985.
- [Johnson 1985b] N. M. Johnson and M. D. Moyer. Absence of oxygen diffusion during hydrogen passivation of shallow-acceptor impurities in single-crystal silicon. *Applied Physics Letters* **46** (8) 787-789, 1985.
- [Johnson 1986] N. M. Johnson, C. Herring and D. J. Chadi. Interstitial hydrogen and neutralization of shallow-donor impurities in single-crystal silicon. *Physical Review Letters* **56** (7) 769-772, 1986.
- [Johnson 1987] N. M. Johnson, F. A. Ponce, R. A. Street and R. J. Nemanich. Defects in single-crystal silicon induced by hydrogenation. *Physical Review B* **35** (8) 4166-4169, 1987.
- [Johnson 1991] N. M. Johnson, C. Doland, F. Ponce, J. Walker and G. Anderson. Hydrogen in crystalline semiconductors. A review of experimental results. *Physica B* **170** 3-20, 1991.
- [Jones 1996] *Early Stages of Oxygen Precipitation in Silicon*, edited by R. Jones. Kluwer Academic Publishers, Dordrecht, 1996.
- [Jones 2000] R. Jones, B. J. Coomer, J. P. Goss, B. Hourahine and A. Resende. The interaction of hydrogen with deep level defects in silicon. *Solid State Phenomena* **71** 173-248, 2000.
- [Kamiura 1992] Y. Kamiura, M. Yoneta, Y. Nishiyama and F. Hashimoto. Evidence for the recombination-enhanced dissociation of a hydrogen-carbon complex in silicon. *Journal of Applied Physics* **72** (8) 3394-3397, 1992.

- [Kamiura 1995] Y. Kamiura, M. Tsutsue, Y. Yamashita, F. Hashimoto and K. Okuno. Deep center related to hydrogen and carbon in p-type silicon. *Journal of Applied Physics* **78** (7) 4478-4486, 1995.
- [Kamiura 1997] Y. Kamiura, N. Ishiga, S. Ohyama and Y. Yamashita. Structure and charge-state-dependent instability of a hydrogen-carbon complex in silicon. *Materials Science Forum Vols. 258-263* 258-263, 1997.
- [Kamiura 2000] Y. Kamiura, K. Fukuda and Y. Yamashita. Motion of hydrogen in silicon revealed by deep-level transient spectroscopy under uniaxial stress. *Journal of Crystal Growth* **210** 122-127, 2000.
- [Kamiura 2002] Y. Kamiura, K. Fukuda, Y. Yamashita and T. Ishiyama. Electronically controlled motion of hydrogen in silicon. *Physical Review B* **65** 113205/1-4, 2002.
- [Kaneta 1995] C. Kaneta and H. Katayama-Yoshida. Atomic configurations and electronic states of carbon-hydrogen complex in silicon. In *22nd International Conference on the Physics of Semiconductors*, edited by D. J. Lockwood, pp. 2215-2218. World Scientific, Singapore, 1995.
- [Kaplyanskii 1961] A. A. Kaplyanskii. Band-splitting in the spectra of cubic crystals subjected to oriented deformation. *Optics and Spectroscopy* **10** 83-87, 1961.
- [Kaplyanskii 1964] A. A. Kaplyanskii. Noncubic centers in cubic crystals and their piezospectroscopic investigation. *Optics and Spectroscopy* **16** 329-337, 1964.
- [Kimerling 1981] L. C. Kimerling and J. L. Benton. Oxygen-related donor states in silicon. *Applied Physics Letters* **39** (5) 410-412, 1981.

- [Kitajima 1999] M. Kitajima, K. Ishioka, K. Murakami, K. Nakanoya and T. Mori. Temperature dependence of the formation of hydrogen molecules in n- and p-type silicon. *Physica B* **273-274** 192-195, 1999.
- [Lang 1974] D. V. Lang. Deep-level transient spectroscopy: A new method to characterize traps in semiconductors. *Journal of Applied Physics* **45** (7) 3023-3032, 1974.
- [Langpape 1997] C. Langpape, S. Fabian, C. Klatt and S. Kalbitzer. Observation of ^1H tunneling diffusion in crystalline Si. *Applied Physics A* **64** 207-210, 1997.
- [Lavrov 2001] E. V. Lavrov and J. Weber. Structural properties of hydrogen-induced platelets in silicon: a Raman scattering study. *Physica B* **308-310** 151-154, 2001.
- [Leary 1998] P. Leary, R. Jones and S. Öberg. Interaction of hydrogen with substitutional and interstitial carbon defects in silicon. *Physical Review B* **57** (7) 3887-3899, 1998.
- [Leitch 1998a] A. W. R. Leitch, V. Alex and J. Weber. H_2 molecules in c-Si after hydrogen plasma treatment. *Solid State Communications* **105** (4) 215-219, 1998.
- [Leitch 1998b] A. W. R. Leitch, V. Alex and J. Weber. Raman spectroscopy of hydrogen molecules in crystalline silicon. *Physical Review Letters* **81** (2) 421-424, 1998.
- [Lévêque 2001] P. Lévêque, P. Pellegrino, A. Hallén, B. G. Svensson and V. Privitera. Hydrogen-related defect centers in float-zone and epitaxial n-type proton implanted silicon. *Nuclear Instruments and Methods in Physics Research B* **174** 297-303, 2001.

- [Maric 1993] D. M. Maric, P. F. Meier and S. K. Estreicher. {H-B}, {H,C}, and {H,Si} pairs in silicon and germanium. *Physical Review B* **47** (7) 3620-3625, 1993.
- [Markevich 1998] V. P. Markevich and M. Suezawa. Hydrogen-oxygen interaction in silicon at around 50 °C. *Journal of Applied Physics* **83** (6) 2988-2993, 1998.
- [Markevich 2000a] V. P. Markevich, L. I. Murin, J. L. Lindström and M. Suezawa. Early stages of oxygen precipitation in silicon: The effect of hydrogen. *Semiconductors* **34** (9) 998-1003, 2000.
- [Markevich 2000b] V. P. Markevich, L. I. Murin, M. Suezawa, J. L. Lindström, J. Coutinho, R. Jones, P. R. Briddon and S. Öberg. Observation and theory of the V-O-H₂ complex in silicon. *Physical Review B* **61** (19) 12964-12969, 2000.
- [Markevich] V. P. Markevich. Private communications, 2002.
- [Mathiot 1989] D. Mathiot. Modeling of hydrogen diffusion in n- and p-type silicon. *Physical Review B* **40** (8) 5867-5870, 1989.
- [Meese 1983] J. M. Meese, J. W. Farmer and C. D. Lamp. Defect symmetry from stress transient spectroscopy. *Physical Review Letters* **51** (14) 1286-1289, 1983.
- [Murakami 1996] K. Murakami, N. Fukata, S. Sasaki, K. Ishioka, M. Kitajima, S. Fujimura, J. Kikuchi and H. Haneda. Hydrogen molecules in crystalline silicon treated with atomic hydrogen. *Physical Review Letters* **77** (15) 3161-3164, 1996.
- [Murin 1998] L. I. Murin, T. Hallberg, V. P. Markevich and J. L. Lindström. Experimental evidence of the oxygen dimer in silicon. *Physical Review Letters* **80** (1) 93-96, 1998.

- [Nickel 2000] N. H. Nickel, G. B. Anderson, N. M. Johnson and J. Walker. Nucleation of hydrogen-induced platelets in silicon. *Physical Review B* **62** (12) 8012-8015, 2000.
- [Noya 1997] J. C. Noya, C. P. Herrero and R. Ramirez. Thermally assisted tunneling of the B-H complex in silicon. *Physical Review Letters* **79** (1) 111-114, 1997.
- [Nye 1957] J. F. Nye. *Physical Properties of Crystals*. Oxford, 1957.
- [Palmetshofer 1992] L. Palmetshofer and J. Reisinger. Defect levels in H⁺-, D⁺-, and He⁺-bombarded silicon. *Journal of Applied Physics* **72** (6) 2167-2173, 1992.
- [Peaker 1999a] A. R. Peaker and M. R. Brozel. Electrical techniques for the measurement of deep states. *III-Vs Review* **12** (1) 44-51, 1999.
- [Peaker 1999b] A. R. Peaker, J. H. Evans-Freeman, P. Y. Y. Kan, L. Rubaldo, I. D. Hawkins, K. D. Vernon-Parry and L. Dobaczewski. Hydrogen reactions with electron irradiation damage in silicon. *Physica B* **273-274** 243-246, 1999.
- [Peaker 2000] A. R. Peaker, J. H. Evans-Freeman, P. Y. Y. Kan, I. D. Hawkins, J. Terry, C. Jeynes and L. Rubaldo. Vacancy-related defects in ion implanted and electron irradiated silicon. *Materials Science and Engineering* **B71** 143-147, 2000.
- [Pearton 1992] S. J. Pearton, J. W. Corbett and M. Stavola. *Hydrogen in Crystalline Semiconductors*. Springer, Berlin, 1992.
- [Pesola 1999] M. Pesola, J. von Boehm, T. Mattila and R. M. Nieminen. Computational study of interstitial oxygen and vacancy-oxygen complexes in silicon. *Physical Review B* **60** (16) 11449-11463, 1999.

- [Pons 1984] D. Pons. Accurate determination of the free carrier capture kinetics of deep traps by space-charge methods. *Journal of Applied Physics* **55** (10) 3644-3657, 1984.
- [Pritchard 1997] R. E. Pritchard, M. J. Ashwin, J. H. Tucker, R. C. Newman, E. C. Lightowlers, M. J. Binns, S. A. McQuaid and R. Falster. Interactions of hydrogen molecules with bond-centered interstitial oxygen and another defect center in silicon. *Physical Review B* **56** (20) 13118-13125, 1997.
- [Pritchard 1998] R. E. Pritchard, M. J. Ashwin, J. H. Tucker and R. C. Newman. Isolated interstitial hydrogen molecules in hydrogenated crystalline silicon. *Physical Review B* **57** (24) 15048-15051, 1998.
- [Pritchard 1999] R. E. Pritchard, J. H. Tucker, R. C. Newman and E. C. Lightowlers. Hydrogen molecules in boron-doped crystalline silicon. *Semiconductor Science and Technology* **14** 77-80, 1999.
- [Provencher 1982] S. W. Provencher. A constrained regularization method for inverting data represented by linear algebraic or integral equations. *Computer Physics Communications* **27** 213-227, 1982.
- [Qin 1985] G. G. Qin, X. C. Yao and J. X. Mou. The preferential alignment of negatively and neutrally charged A-centers in silicon under $\langle 100 \rangle$ uniaxial stress. *Solid State Communications* **56** (2) 201-204, 1985.
- [Sachse 1997] J. U. Sachse, E. O. Sveinbjörnsson, W. Host, J. Weber and H. Lemke. Electrical properties of platinum-hydrogen complexes in silicon. *Physical Review B* **55** (24) 16176-16185, 1997.
- [Sachse 1999] J. U. Sachse, J. Weber and E. O. Sveinbjörnsson. Hydrogen-atom number in platinum-hydrogen complexes in silicon. *Physical Review B* **60** (3) 1474-1476, 1999.

- [Samara 1986] G. A. Samara and C. E. Barnes. Lattice relaxation accompanying carrier capture and emission by deep electronic levels in semiconductors. *Physical Review Letters* **57** (16) 2069-2072, 1986.
- [Schroder 1998] D. K. Schroder. *Semiconductor Material and Device Characterization*, second edition. Wiley, New York, 1998.
- [Simoen 2002] E. Simoen, C. Claeys, R. Job, A. G. Ulyashin, W. R. Fahrner, O. De Gryse and P. Clauws. Hydrogen plasma-enhanced thermal donor formation in n-type oxygen-doped high-resistivity float-zone silicon. *Applied Physics Letters* **81** (10) 1842-1844, 2002.
- [Stallinga 1998] P. Stallinga, P. Johannesen, S. Herström, K. Bonde Nielsen, B. Bech Nielsen and J. R. Byberg. Electron paramagnetic resonance study of hydrogen-vacancy defects in crystalline silicon. *Physical Review B* **58** (7) 3842-3852, 1998.
- [Stievenard 1986] D. Stievenard and D. Vuillaume. Profiling of defects using deep level transient spectroscopy. *Journal of Applied Physics* **60** (3) 973-979, 1986.
- [Svensson 1991] B. G. Svensson, B. Mohadjeri, A. Hallén, J. H. Svensson and J. W. Corbett. Divacancy acceptor levels in ion-irradiated silicon. *Physical Review B* **43** (3) 2292-2298, 1991.
- [Sze 1985] S. M. Sze. *Semiconductor Devices. Physics and Technology*. Wiley, New York, 1985.
- [Terry 1999] J. G. Terry. *Electrical Characterization of Transition Metals and Hydrogen in Silicon*. Ph.D. thesis, Department of Electrical Engineering and Electronics, University of Manchester Institute of Science and Technology, 1999.

- [Tokuda 1998] Y. Tokuda and H. Shimada. Formation of hydrogen-related traps in electron-irradiated n-type silicon by wet chemical etching. In *Hydrogen in Semiconductors and Metals*, edited by N. H. Nickel et al., pp. 363-368. Materials Research Society, Warrendale, 1998.
- [Van de Walle 1994] C. G. Van de Walle. Energies of various configurations of hydrogen in silicon. *Physical Review B* **49** (7) 4579-4585, 1994.
- [Watkins 1961] G. D. Watkins and J. W. Corbett. Defects in irradiated silicon. I. Electron spin resonance of the Si- A center. *Physical Review* **121** (4) 1001-1014, 1961.
- [Watkins 1965] G. D. Watkins and J. W. Corbett. Defects in irradiated silicon: Electron paramagnetic resonance of the divacancy. *Physical Review* **138** (2A) 543-555, 1965.
- [Watkins 1999] G. D. Watkins. Vacancies and interstitials and their interactions with other defects in silicon. In *Electrochemical Society Proceedings Volume 99-1*, edited by T. Abe et al., pp. 38-52. Electrochemical Society, Pennington, 1999.
- [Weese 1992] J. Weese. A reliable and fast method for the solution of Fredholm integral equations of the first kind based on Tikhonov regularization. *Computer Physics Communications* **69** 99-111, 1992.
- [van Wieringen 1956] A. van Wieringen and N. Warmoltz. On the permeation of hydrogen and helium in single crystal silicon and germanium at elevated temperatures. *Physica* **22** 849-865, 1956.
- [Xu 1992] H. Xu. Electronic structure of hydrogen-vacancy complexes in crystalline silicon: A theoretical study. *Physical Review B* **46** (3) 1403-1422, 1992.

- [Yao 1987] X. C. Yao, J. X. Mou and G. G. Qin. Shifts and splittings of electron energy levels of A-centers in silicon under uniaxial stress. *Physical Review B* **35** (11) 5734-5739, 1987.
- [Yoneta 1991] M. Yoneta, Y. Kamiura and F. Hashimoto. Chemical etching-induced defects in phosphorus-doped silicon. *Journal of Applied Physics* **70** (3) 1295-1308, 1991.
- [Zhou 1995] Y. Zhou, R. Luchsinger and P. F. Meier. Theoretical study of H-P and H-B complexes in silicon. *Physical Review B* **51** (7) 4166-4171, 1995.